

Search for Heavy, Long-lived, Charged Particles with Large Ionisation Energy Loss in pp  
Collisions at  $\sqrt{s} = 13$  TeV Using the ATLAS Experiment and the Full Run 2 Dataset

by

Marija Glisic

A dissertation accepted and approved in partial fulfillment of the

requirements for the degree of

Doctor of Philosophy

in Physics

Dissertation Committee:

Eric Torrence, Chair

Laura Jeanty, Advisor

Tien Tien Yu, Core Member

Luca Mazzucato, Institutional Representative

University of Oregon

Fall 2024

©2024 Marija Glisic  
This work is licensed under a Creative Commons  
Attribution-NonCommercial-NoDerivs (United States) License.



## DISSERTATION ABSTRACT

Marija Glisic

Doctor of Philosophy in Physics

Title: Search for Heavy, Long-lived, Charged Particles with Large Ionisation Energy Loss in pp Collisions at  $\sqrt{s} = 13$  TeV Using the ATLAS Experiment and the Full Run 2 Dataset

Long-lived Supersymmetric particles offer an exciting sector of BSM physics that is not fully explored, but could be produced at the Large Hadron Collider (LHC) in proton-proton collisions of  $\sqrt{s} = 13$  TeV. This thesis describes the search for long-lived sleptons using a highly-ionizing ditrack signature. It is a continuation of a previous search which used a single track and targeted long-lived R-hadrons and charginos. The ditrack selection has greater sensitivity for pair-produced staus with lifetimes of 10 ns or longer. The staus would present as high-momentum tracks with high ionization energy relative to the minimum-ionizing SM particles of similar momenta, and are detectable, using ATLAS's Pixel Detector to measure ionization energy loss. These massive particles do not have simple SM backgrounds which can be easily simulated, but rather can be mimicked by detector effects and mis-reconstructions. As such, a data-driven method is formed to estimate the background. This analysis utilized the full ATLAS Run 2 dataset with integrated luminosity of  $139 \text{ fb}^{-1}$ , and did not observe an excess of events which would indicate a discovery of long-lived staus. For meta-stable lifetimes of 3, 10, and 30 ns, long-lived staus of masses less than 420, 615, and 620 GeV were excluded at 95% confidence level, and stable staus were excluded for rest masses less than 520 GeV.

This dissertation contains yet unpublished material.

## CURRICULUM VITAE

NAME OF AUTHOR: Marija Glisic

GRADUATE AND UNDERGRADUATE SCHOOLS ATTENDED:

University of Oregon, Eugene, OR, USA  
University of Washington, Seattle, WA, USA

DEGREES AWARDED:

Doctor of Philosophy, Physics, 2024, University of Oregon  
Bachelor of Science, Physics, 2016, University of Washington

AREAS OF SPECIAL INTEREST:

Supersymmetry

PROFESSIONAL EXPERIENCE:

Research Assistant, University of Oregon, 2018 – 2024  
Graduate Teaching Assistant, University of Oregon, 2017 – 2024

GRANTS, AWARDS AND HONORS:

PUBLICATIONS:

The ATLAS Collaboration (2023). Search for long-lived, massive particles in events with displaced vertices and multiple jets in  $pp$  collisions at  $\sqrt{s} = 13$  TeV with the ATLAS detector. *arXiv:2301.13866*)

The ATLAS Collaboration (2024). Search for heavy, long-lived particles dEdx and low beta or two highly-ionizing tracks in  $pp$  collisions at  $\sqrt{s} = 13$  TeV with the ATLAS detector. *under review, JHEP*)

## ACKNOWLEDGEMENTS

This dissertation would not have been possible without the support of many people. A big thank you to my advisor, Laura, who provided mentorship, patience, and kindness. Thank you to my mum and dad, Svetlana and Zoran, and sister, Vanja, who will always listen to me complain. Thanks to my brother Pavle for the funny videos, and to Marina, my best friend. Thank you also to all my physics grad school friends, who were the best company during a brutal first year and COVID pandemic. Thank you to my committee members Eric Torrence, Tien-Tien Lu, and Luca Mazzucato. Thank you to Ismet Siral, Amanda Steinhiebel, and Johan Bonilla who were extremely helpful in my learning, and thank you to Avi Kahn, and his advisor Elliot Lipeles, whose contribution to the background estimate was invaluable.

TABLE OF CONTENTS

Chapter		Page
I	THEORY . . . . .	16
	1.1 Standard Model . . . . .	16
	1.2 Beyond Standard Model . . . . .	22
	1.3 Supersymmetry . . . . .	24
II	THE LHC AND THE ATLAS EXPERIMENT . . . . .	28
	2.1 Large Hadron Collider . . . . .	28
	2.2 ATLAS Detector . . . . .	29
	2.3 Trigger and Data Acquisition System . . . . .	36
III	RECONSTRUCTION . . . . .	38
	3.1 Event Reconstruction . . . . .	38
	3.2 Jets . . . . .	39
	3.3 Missing Transverse Momentum . . . . .	40
	3.4 Muons . . . . .	42
	3.5 Tracks . . . . .	42

Chapter	Page
IV DITRACK ANALYSIS . . . . .	47
4.1 Motivation . . . . .	47
4.2 Event-Level Selections . . . . .	49
4.3 Track-Level Selections . . . . .	53
4.4 Ditrack Mass Windows . . . . .	59
4.5 Ditrack $dE/dx$ Optimization . . . . .	62
4.6 Summary of two-track signal region . . . . .	65
4.7 Two-track analysis data and signal cutflow . . . . .	65
V BACKGROUND ESTIMATE . . . . .	72
5.1 Ditrack Background . . . . .	72
5.2 ABCD Method . . . . .	73
5.3 Toy Model . . . . .	82
5.4 Discovery SR Validation . . . . .	84
VI DITRACK UNCERTAINTIES AND RESULTS . . . . .	86
6.1 Background Uncertainties . . . . .	86
6.2 Results . . . . .	87
6.3 Outlook . . . . .	94

Chapter	Page
APPENDIX: DITRACK DE/DX OPTIMIZATION STUDY . . . . .	95
A.1 Exclusion Signal Region . . . . .	95
A.2 Discovery Signal Region . . . . .	95
REFERENCES CITED . . . . .	112

## LIST OF FIGURES

Figure	Page
1.1. Standard Model of elementary particles [1]. . . . .	2
1.2. Lifetimes of Standard Model particles [2] . . . . .	5
1.3. Summary of Standard Model analyses results as measured by the ATLAS Collaboration [3] . . . . .	6
1.4. Galaxy Rotation Curve of NGC 6503 [5] . . . . .	7
1.5. Production cross-sections of SUSY particles from p-p collisions of $\sqrt{s} =$ 13 TeV [9]. . . . .	11
1.6. Feynman diagram of long-lived staus. . . . .	12
2.1. Side-view of the ATLAS detector . . . . .	15
2.2. Cross-section view of the 4-Layer Pixel Detector for Run 2. . . . .	16
2.3. Diagram of a time-over-threshold measurement. The larger charge signal corresponds to a longer time s. [13] . . . . .	17
2.4. Schematic view of the Inner Detector, with an enlarged view of the Pixel Detector. . . . .	19
2.5. Table of Inner Detector subsystem geometries. [14] . . . . .	20
3.1. Cross-sectional view of the ATLAS detector, with various particle signatures depicted. [20]. . . . .	24
3.2. Jet reconstructions from calorimeter cells using the anti-kT algorithm [22]. . . . .	26
3.3. Energy losses in silicon for muons of various kinetic energies [8]. . . . .	29
3.4. Straggling functions for the energy loss distribution of a 500 MeV pion for various thicknesses of silicon, with each distribution normalized by modal value [8]. . . . .	30

Figure	Page
4.1. The observed mass distribution in the Inclusive-High signal-region bins observed in [26]. Several representative signal models are overlaid the expected background and the observed events in data. . . . .	33
4.2. Comparison of offline MET from a simulated 400 GeV stau with 10ns lifetime, after the single-track analysis selection is applied (shown in blue) and the ditrack selection (shown in red). For both cases, all event and track-level selections were applied, but mass windows were not. . . . .	38
4.3. Offline $E_T^{\text{miss}}$ for stau samples with 10ns lifetimes and masses of 200, 300, 400, 500 GeV. All event-level requirements including the trigger, $E_T^{\text{miss}}$ , and event/jet cleaning requirements are applied. . . . .	39
4.4. Individual Slepton Track Transverse Mass. The track transverse mass distributions of both slepton tracks, for sleptons samples with lifetimes of 10ns, and masses of 200, 300, 400, 500 GeV. All event-level requirements including the trigger, $E_T^{\text{miss}}$ , and jet cleaning requirements are applied. The track is required, for the signal samples, to be matched to a sparticle. . . . .	41
4.5. Event-Level Slepton Track Transverse Mass. Using the 400 GeV, 10 ns stau sample, the correlation of transverse mass of pair-produced stau tracks. All event-level requirements including the trigger, $E_T^{\text{miss}}$ , and jet cleaning requirements are applied. The track is required, for the signal samples, to be matched to a sparticle. . . . .	42
4.6. Plot shows product of two candidate tracks' electrical charges, where $-1$ indicates the two tracks had opposite electric charges, and $1$ indicates the two tracks had matching electric charges. All event-level requirements including the trigger, $E_T^{\text{miss}}$ , and event/jet cleaning requirements are applied. Tracks are required to pass all track-quality requirements, then the two best tracks (in terms of $p_T$ , then $dE/dx$ ) are the two candidate tracks. The signal samples are 400 GeV staus with a lifetime of 10 ns. Data is from 200k events in 2018. For the signal samples, the tracks are required to be matched to a sparticle. . . . .	43
4.7. Invariant mass for stau samples with 10ns lifetimes and masses of 200 and 400 GeV, and for data. All event-level requirements including the trigger, $E_T^{\text{miss}}$ , and event/jet cleaning requirements are applied. Tracks are required to pass all track-quality requirements, then the two best tracks (in terms of $p_T$ , then $dE/dx$ ) are chosen to calculate the invariant mass. Data is from 200k events in 2018. . . . .	44

Figure	Page
4.8. Example of a mass window applied to the preliminary signal region events of 500 GeV, 10 ns staus. The mass window is highlighted in pink. . . . .	45
4.9. The estimated background yield in each mass window is shown. The error on the prediction includes the statistical and systematic uncertainty applied to the toy model. The error on the ratio is the fractional error . . .	46
4.10. The estimated background yield in each mass window is shown. The error on the prediction includes the statistical and systematic uncertainty applied to the toy model. The error on the ratio is the fractional error. . .	48
4.11. Highest achieved signal significances of varying track-level $dE/dx$ cuts. . . . .	54
4.12. The toy background yields of the highest achieved signal significances. . .	54
4.13. The signal yields of the highest achieved signal significances. . . . .	54
4.14. Optimization study of 400 GeV, 30 ns staus for the Discovery SR. Plots show the a) highest signal significances, and the corresponding b) toy background yields, and c) signal yields for varying track-level $dE/dx$ cuts. Note: The mass window parameters vary for each bin, to optimize for lowest CLs values. . . . .	54
4.15. Optimization study of 500 GeV, 10 ns staus for the Exclusion SR. Plots show the a) lowest CLs values, and the corresponding b) toy background yields, and c) signal yields for varying track-level $dE/dx$ cuts. Note: CLs values are plotted only if they are less than 0.05, and mass window parameters vary for each bin, to optimize for lowest CLs values. . . . .	55
4.16. The track $dE/dx$ distributions of both slepton tracks, for sleptons samples with lifetimes of 10ns, and masses of 200, 300, 400, 500 GeV. Using the 400 GeV, 10 ns stau sample, the correlation of $dE/dx$ of pair-produced stau tracks. All event-level requirements including the trigger, $E_T^{\text{miss}}$ , and event/jet cleaning requirements are applied. The track is required, for the signal samples, to be matched to a sparticle. Data is from 200k events in 2018. . . . .	56
5.1. Z-mumu tracks were binned by $p_T$ , and the plots show a) the $dE/dx$ distributions, b) the mean $dE/dx$ values of several bins, and c) the $dE/dx$ tail fractions for different $dE/dx$ boundaries. The bins used are the 30, 50, 100, 300, and 500 GeV bins, and their respective $dE/dx$ distributions and mean values show good agreement within statistical uncertainty. Likewise, the tail fractions remain consistent across $p_T$ , with	

Figure	Page
some statistical fluctuation occurring in the 700-1000 GeV bin, which has the lowest population of tracks. . . . .	61
5.2. Schematic diagrams of the two-track Signal Region and the corresponding Control Regions. Events must pass all event-level requirements and have at least two candidate tracks, one which passes all track-level cuts, and the second track which has to pass all track-level cuts except for $p_T > 120$ GeV and the ionization cut. The events are sorted into the corresponding ABCD regions by the characteristics of their second track, which is noted in the diagram as 'Second Track'. . . . .	63
5.3. Schematic diagrams of the two-track high- $\eta$ Validation Regions. Events must pass all event-level requirements and have at least two candidate tracks which pass all track-level cuts but the $\eta$ , ionization, transverse mass, and momentum requirements. Both tracks are required to have $1.8 <  \eta  < 2.5$ . At least one track in the event has $p_T > 120$ GeV and $dE/dx > 1.4 \text{ MeV g}^{-1}\text{cm}^2$ , and the events are sorted into the corresponding ABCD regions by the characteristics of their second track. The given uncertainties are statistical only. . . . .	67
6.1. Ratio of data and toy mass distribution in three Vrs is fit to line, the 0.68 confidence interval band is used as a non-closure systematic uncertainty. . . . .	72
6.2. All observed data events marked by red squares, overlaid on the toy background model estimate of the $dE/dx$ -mass distributions [Kahn, A]. . . . .	74
6.3. Both tracks' $dE/dx$ -derived masses from the observed data events overlaid on the background estimate of $dE/dx$ -derived mass [Kahn, A]. . . . .	75
6.4. Both tracks' $dE/dx$ -derived masses from the observed data events overlaid on the background estimate of $dE/dx$ -derived mass. [Kahn, A]. . . . .	76
6.5. The expected and observed signal sensitivity of the ditrack analysis, for long-lived staus with 3ns lifetimes. . . . .	77
6.6. The expected and observed signal sensitivity of the ditrack analysis, for long-lived staus with 10ns lifetimes. . . . .	77
6.7. The expected and observed signal sensitivity of the ditrack analysis, for long-lived staus with 30ns lifetimes. . . . .	78

Figure	Page
6.8. The expected and observed signal sensitivity of the ditrack analysis, for long-lived staus with 3000ns lifetimes. . . . .	78

## LIST OF TABLES

Table	Page
2.1. Yearly Pixel Detector settings by layer during Run2 datataking. . . . .	18
4.1. Good run lists for the data used in this analysis. . . . .	35
4.2. List of unrescaled lowest $E_T^{\text{miss}}$ HLT trigger decisions. . . . .	37
4.3. The ionization requirements of the Discovery and Exclusion SRs. . . . .	42
4.4. The 2D mass window parameters derived using the trapezoidal method. The angle identifies the opening angle of the mass window's cone, and lower edge mass identifies the mass point (mass, mass) at the center of the trapezoidal lower edge. . . . .	46
4.5. The 2D mass window parameters derived using the trapezoidal method. The angle identifies the opening angle of the mass window's cone, and lower edge mass identifies the mass point (mass,mass) at the center of the trapezoidal lower edge. The yields of slepton MC samples in the Exclusion SR are given after the mass windows are applied. . . . .	47
4.6. Summary of two-track signal selection. . . . .	51
4.7. Cutflow of the two-track signal region for sleptons with mass 400 GeV and lifetime 10 ns (no mass window applied). . . . .	52
4.8. Cutflow of the two-track signal region for the full Run2 dataset, blinded after nohadron cut (no mass window applied). An early cut of $p_T \gtrsim 50$ GeV is applied to reduce computing needs . . . . .	53
5.1. Validation Region Descriptions . . . . .	60
5.2. Kinematic definitions of the two-track signal, control and validation regions for the Exclusion SR. Events must pass all event-level requirements and have at least two candidate tracks. Candidate tracks must pass all other selection requirements, and are ranked by $p_T$ or $p$ , and by $dE/dx$ , using the boundaries defined below. The best-ranked track is noted 'Track 1' and has high $p_T$ or $p$ , and high $dE/dx$ , as defined by the parameters below. The second best-ranked track is noted as 'Track 2'. These tracks must have opposite electric charge and calculated invariant mass above 200 GeV. . . . .	62

Table	Page
5.3. Event yields of ABCD regions in Run2 data, with Discovery and Exclusion SRs. The uncertainties are statistical . . . . .	63
5.4. Event yields of the low-momentum and W-enhanced VRs in Run2 data, for the Exclusion SR (with $dE/dx$ bounds of 1.6 and 1.3 for the first and second tracks, respectively). The given uncertainties are statistical only. Signal contamination from 200 GeV staus of 10 ns lifetimes are given, no expected VR is given for staus. . . . .	65
5.5. Event yields of the invariant mass and Z-mumu VRs in Run2 data, for the Exclusion SR (with $dE/dx$ bounds of 1.6 and 1.3 for the first and second tracks, respectively). The given uncertainties are statistical only. . . . .	66
5.6. Event yields of high- $\eta$ VR with estimated and actual background yields in high- $\eta$ VR region A. The signal contamination from 200 GeV, 10 ns staus is included, though the expected yields estimate is not included. . .	68
5.7. Comparison of event yields in Region A between data and the toy background model for various VR. The Estimated Yield is calculated from data using $A = BC/D$ and the Toy Model Yield is the number of events from the Toy Model Background in Region A. The uncertainty in the Toy Model estimate shown is only the statistical uncertainty. . . . .	69
5.8. Comparison of event yields in Region X between data and the toy background model for various validation regions. The uncertainty in the Toy Model estimate shown is only the statistical uncertainty. . . . .	69
5.9. Validation Region Definitions - Discovery (Lowered $dE/dx$ ) . . . . .	70
5.10. Event yields of single-track ABCD regions of low-momentum VR in Run2 data, with $dE/dx$ cut of $1.7 \text{ MeV g}^{-1}\text{cm}^2$ . . . . .	70
6.1. Exclusion SR data and background yields in different trapezoids defined for different mass windows, with the window's lower mass bound noted. . . . .	73

# CHAPTER I

## THEORY

This dissertation describes a search for long-lived staus, and this first chapter motivates their possible existence. This chapter provides an overview of the current phenomenology of high-energy particle physics, covering the Standard Model (Section 1.1) and its experimental success (Section 1.1.2). A further review of particle lifetimes (Section 1.1.1) is given. Then, Beyond Standard Model physics is explored (Section 1.2) covering dark matter and the hierarchy problem, motivating the theory of Supersymmetry (Section 1.3), and covering stau particles in further detail.

### 1.1 STANDARD MODEL

Our current understanding of the universe's known forces and matter is described by the theory of the Standard Model (SM). It is a quantum field theory which describes known particles and the forces with which they interact. It has been very successful, in that its theoretical predictions have matched well with particle physics experiments, see Section 1.1.2.

There are four fundamental forces: strong nuclear, weak nuclear, electromagnetic, and gravity. The SM describes the interactions of particles using the first three listed forces, but gravity is not explained by the SM. Elementary particles are either fermions or bosons, depending on their spin. Fermions have a half-integer spin, while bosons have integer spins. Gauge bosons are those which have spin 1, and they are known as force carriers, since they facilitate the interactions of the strong, weak, and electromagnetic forces between certain particles. The known gauge bosons are the gluon, the photon, and the  $W$  and  $Z$  bosons. There is also one scalar boson with

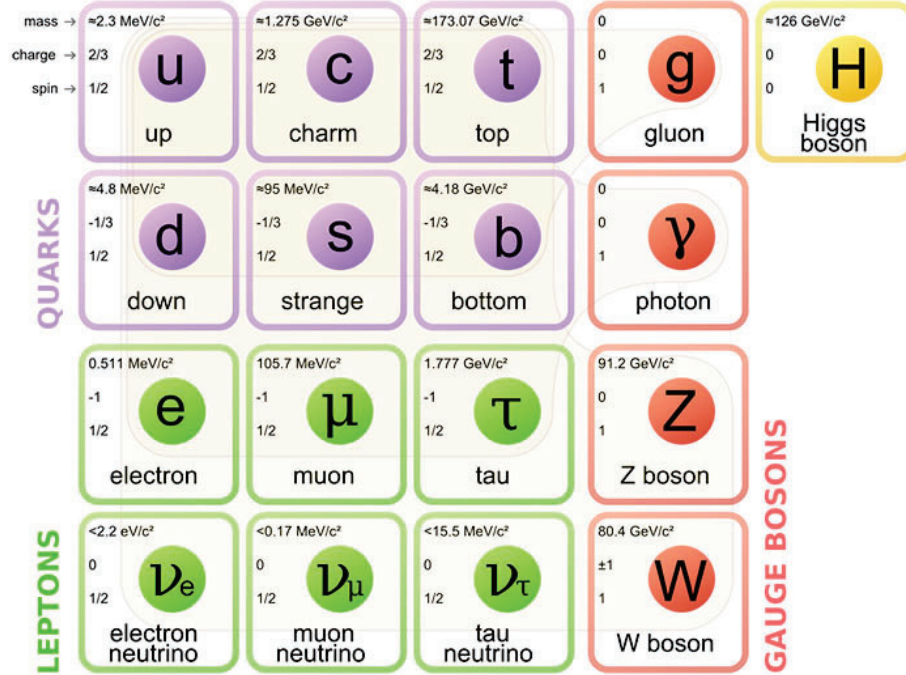


FIGURE 1.1. Standard Model of elementary particles [1].

spin 0, called the Higgs boson. The elementary particles of the Standard Model can be seen in Figure 1.1. The figure does not include anti-particles, which are particles with the same mass but opposite physical charges. The photon, gluon, Higgs, and Z bosons are their own anti-particles, while the  $W^-$  bosons are the antiparticles of the  $W^+$  bosons. In the case of fermions, their antiparticles are always separate particles.

Gluons carry the strong force. The strong force interacts through color charges, noted as red, green, blue as well as anti-red, anti-green, and anti-blue. To achieve neutral color charge, either a color is matched with its anti-color (ex.  $g\bar{g}$ ), or all three colors are grouped ( $rgb$ ). Individual gluons will have a color and an anti-color charge pair, such as (ex.  $g\bar{b}$ ).

Photons are force carriers of the electromagnetic force (EM). They interact with electromagnetic particles which hold an electric charge, but do not hold an electric

charge themselves. Because they cannot carry a charge like the gluon does with its color charge pair, EM particles cannot change electric charges of the particles they interact with.

W and Z bosons are the force carriers of the weak force. Z bosons are electrically neutral, while  $W^\pm$  bosons will have either a -1 or +1 EM charge. They operate through the weak isospin and weak hypercharge.  $W^\pm$  bosons will change the EM charge of the particle they interact with due to carrying an EM charge themselves. They can also change the flavor of a particle. The Z boson cannot change the flavor or EM charge of the particles it interacts with.

Fermions are particles with half-integer spins. The elementary fermions are divided into quarks and leptons. Both these groups have three generations, simply known as the first, second and third. The quarks and leptons have similar properties across these generations, except for their masses which increase by generation.

Leptons can be electrically charged or neutral. The charged leptons are electrons, muons, and taus. Neutral leptons are the electron neutrino, the muon neutrino, and the tau neutrino. Both charged and neutral leptons will interact through the weak force, but the charged leptons will also interact with the electromagnetic force. Leptons have a conserved quantum number called the lepton number, which assigns a +1 to any lepton, and a -1 to any anti-lepton. In all particle interactions the sum of all the leptons numbers, or L, must be conserved.

Quarks include the up, down, strange, charm, top, and bottom quarks. Up-type quarks (up, charm, and top) have electric charge of +2/3, as well as isospin and single color charges. Down-type quarks (down, strange, and bottom) also have isospin and color charges, but their electric charges are -1/3. Since quarks carry these multiple charges, they are able to interact with the EM, strong, and weak forces. Quarks

will combine with other quarks to create color-neutral particles, known as hadrons. These can be sets of two quarks, mesons, or sets of three, baryons. Protons are a widely known example of a baryon, formed of two up quarks and a down quark in a bound state. Baryons also have a conserved quantum number called the baryon number, or  $B$ , which must be conserved in all interactions. It can be calculated by the equation:

$$B = \frac{1}{3}(n_q - n_{\bar{q}}) \quad (1.1)$$

where  $n_q$  is the number of quarks and  $n_{\bar{q}}$  the number of anti-quarks.

### 1.1.1 Lifetimes of Particles

The Standard Model contains many particles, both the elementary bosons and fermions, as well as hadrons. These particles can have a variety of lifetimes, depending on how likely they are to decay. A particle's proper lifetime is inversely proportional to its decay width, and is defined by the amount of time taken for a sample of particles to reduce by  $1/e$ .

The Figure 1.2 shows a variety of Standard Model particles, with their corresponding rest mass and proper lifetimes. The leftmost shaded area is of lifetimes which are considered detector-prompt, roughly meaning the particles promptly decay and do not travel a notable distance within a particle detector, according to its position resolution. The rightmost shaded area is of detector-stable lifetimes, where a particle will travel at least 10 meters before decaying according to the proper lifetime. Note that heavier particles tend to have shorter lifetimes.

The proper lifetime of particles is given by the equation:

$$\tau^{-1} = \frac{1}{2m_X} \int d\Pi_f |M(m_X \rightarrow \{p_f\})| \quad (1.2)$$

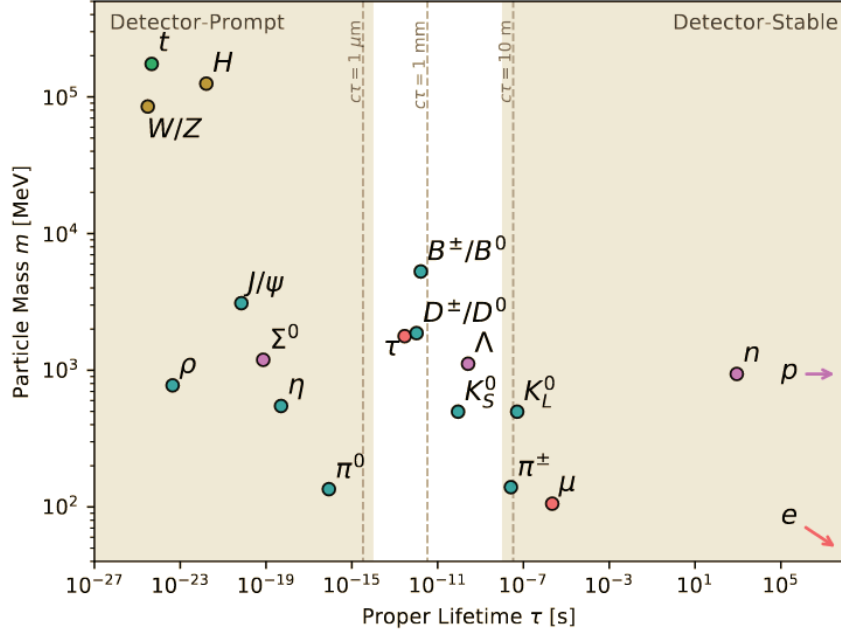


FIGURE 1.2. Lifetimes of Standard Model particles [2]

Here  $\tau$  is the proper lifetime,  $m_X$  is the mass of the particle,  $M$  is the matrix element of the particle's decay into the decay products denoted by  $p_f$ , and  $d\Pi_f$  is the Lorentz-invariant phase space of the decay, given that  $\hbar = c = 1$  [2]. The inverse factor of  $m_X$  is why heavier particles tend to shorter lifetimes, as seen in Figure 1.2. Also, the matrix element of the decay is governed by several factors which influence the lifetime of the particle. One factor is the coupling constant of the decay, which is determined by the force associated to the decay. The coupling constants of the strong, EM, and weak forces are roughly 1,  $1/137$  and  $10^{-6}$ , respectively, at low energies. This means particles which only have weak decays tend to have the longest lifetimes, then those with EM decays, and lastly strong. Another factor which can result in longer lifetimes is when the decays have nearly mass-degenerate spectra, meaning the difference in mass between the particle and its decay products is nearly zero. This is denoted by the phase-space of the decay, or  $d\Pi_f$  of Equation 1.2. For

example, this occurs in the case of the neutron, which has a mean lifetime of 878.4 s and a rest mass of 939.6 MeV. The neutron decays into a proton, an electron, and an anti-electron neutrino, which have a combined rest mass of 938.8 MeV, or only 0.8 MeV less than that of the neutron. Lastly, when the decays are facilitated by highly virtual intermediate states, the lifetimes are longer. Particles can also have multiple decay modes, so the more likely decays will dominate the proper lifetime.

### 1.1.2 Experimental Status

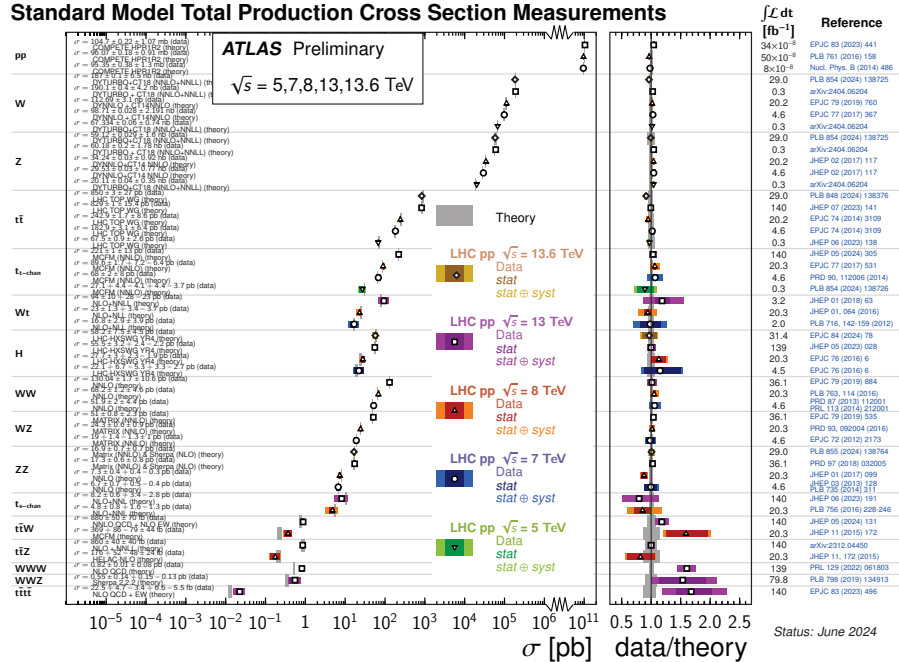


FIGURE 1.3. Summary of Standard Model analyses results as measured by the ATLAS Collaboration [3]

The Standard Model has had great experimental success. SM measurements by the ATLAS Collaboration have found great agreement between the theoretized and observed cross-sections, as seen in Figure 1.3. The last undetected particle of the

Standard Model was the theorized Higgs boson, and was discovered in 2012 with a mass of 125 GeV [4].

## 1.2 BEYOND STANDARD MODEL

For all of the Standard Model's experimental success, there are still unexplained questions in high-energy physics which SM does not answer. These include the nature of dark matter, and the hierarchy problem.

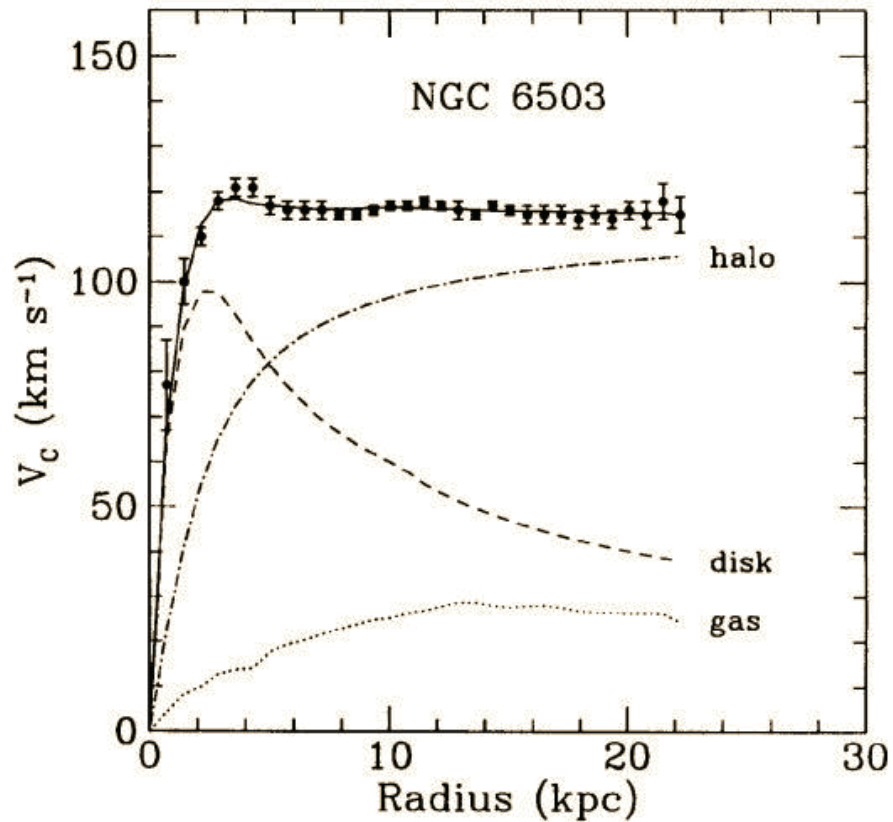


FIGURE 1.4. Galaxy Rotation Curve of NGC 6503 [5]

Dark matter (DM) is matter which does not interact with any Standard Model matter through strong or EM interactions. The only known interactions of DM are gravitational. One of the earliest sources of evidence of DM is galaxy rotation

curves, where the orbital speed is plotted relative to the radius of a galaxy, as seen in Figure 1.4. Visible, SM matter is arranged in the shape of a disk or exists as less-orderly gas, and SM alone would result in a falling rotation curve (labeled 'disk' in Figure 1.4). However, with the addition of a halo of dark matter, the rotation curve is flattened, matching the observed orbital speeds [6]. Other evidence of DM includes the mass distributions of the Bullet Cluster [7], and also the power spectrum of the Cosmic Microwave Background [8], which indicates the ratio of SM matter to DM is about 1:5.

The hierarchy problem considers why there is a large difference between the scale of the electroweak and gravitational forces. The Fermi scale, or the energy scale at which electroweak interactions typically occur, is often noted as  $M_W = 246$  GeV. The Planck scale however, where interactions with quantum gravity come into play is  $M_P = 2.4 \times 10^{18}$  GeV, or 17 orders of magnitude larger than  $M_W$ . In comparison, the energy scale of the strong force is about 1 GeV, only 3 orders of magnitude away from  $M_W$ . While this large discrepancy in scale does not invalidate the Standard Model, it does pose some problems when regarding the mass of the Higgs boson. This mass can be calculated as the sum of the bare Higgs mass and the quantum correction terms from all other fermions and bosons which interact with the Higgs boson. At first order, the mass calculation is as follows:

$$m_{H,phys}^2 = m_{H,bare}^2 + \sum_{fermion} k_f m_f^2 + \sum_{boson} k_b m_b^2 \quad (1.3)$$

$$= m_{H,bare}^2 - \frac{|\lambda_f|^2}{8\pi^2} \Lambda_{UV} + \frac{|\lambda_b|^2}{8\pi^2} \Lambda_{UV} \quad (1.4)$$

Here, the  $\lambda$  coefficients are the coupling constants of the fermion/boson to the Higgs, and  $\Lambda_{UV}$  is the ultraviolet cutoff, the high-energy cutoff. This  $\Lambda_{UV}$  can be interpreted as the energy scale where new physics enters, altering the high-energy behavior of the Standard Model. If we set this cutoff at the Plank scale, then  $\Lambda_{UV}^2$  has a magnitude of  $10^{30}$  GeV. As the largest quantum correction comes from the heaviest fermion, the top quark, for which  $\lambda_f \approx 0.94$ . Then, the quantum correction to the Higgs boson mass is order  $10^{27}$  GeV. However, the 2012 discovery of the Higgs boson found the mass to be 125 GeV. This can be potentially be fixed by including Beyond Standard Model (BSM) particles. If BSM particles exist and interact with the Higgs boson, they would introduce more quantum corrections to the theoretical Higgs boson mass calculation. This possible solution to the hierarchy problem lead theorists to explore a model called Supersymmetry.

### 1.3 SUPERSYMMETRY

Supersymmetry (SUSY) is a theory which posits that for every SM particle, there exists a supersymmetric particle with the same characteristics, except for its spin. The spins differ by a half-integer, meaning that the supersymmetric partner of a SM fermion is a boson, and the supersymmetric partner of the SM boson is a fermion. This helps resolve the hierarchy problem by including the quantum corrections from the SUSY particles. The quantum corrections from a fermion are negative contributions, while those of a boson are positive. Then, the negative quantum correction from the Standard Model's fermions are balanced by the positive quantum corrections of the supersymmetric bosons, and the same is true for the SM bosons and SUSY fermions. This balancing allows for the quantum corrections to partially cancel, leaving the bare mass of the Higgs boson to match up with the

experimental value of 125 GeV. Part of equation 1.5 is reproduced below, showing a fermion's quantum correction to the Higgs boson mass:

$$m_{H,phys}^2 = m_{H,bare}^2 - \frac{|\lambda_f|^2}{8\pi^2} \Lambda_{UV} \quad (1.5)$$

With the addition of the fermion's superpartner, and the assumption that the superpartner's coupling constant is equal to that of the SM fermion (i.e.  $\lambda_f = \lambda_s$ ), the Higgs boson mass

$$m_{H,phys}^2 = m_{H,bare}^2 - \frac{|\lambda_f|^2}{16\pi^2} \left\{ \Lambda_{UV} - 2m_s^2 \ln\left(\frac{\Lambda_{UV}}{m_s}\right) \right\} \quad (1.6)$$

Note the opposite sign between the SM fermion and its SUSY partner. This balancing allows for the quantum corrections to cancel, leaving the bare mass of the Higgs boson to match up with the experimental value of 125 GeV with less fine-tuning of model parameters needed.

The supersymmetric partners of the Standard Model fermions are scalar bosons, particles with spin-0. These supersymmetric partners are (not imaginatively) called scalar quarks and scalar leptons, or squarks and sleptons. Like their SM counterparts, squarks will be subject to strong interactions. They will also form bound states called R-hadrons, similar to the SM hadrons. Charged sleptons are mainly electroweakly interacting. The individual charged sleptons are called selectrons, smuons, and staus. In the case of the Standard Model Higgs boson, the SUSY partners are called higgsinos, can be electrically charged charginos, or electrically neutral neutralinos. As seen in Figure 1.5, the production cross-sections of the SUSY particles depend on the particle's masses, which are currently unknown. The strongly-interacting squarks and higgsinos have higher production cross-sections, while the charged sleptons are

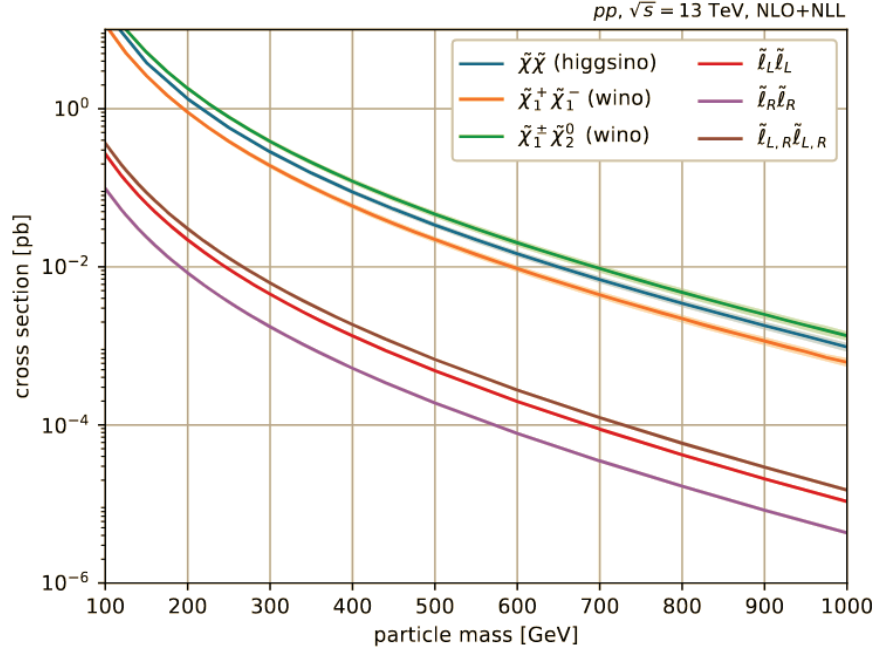


FIGURE 1.5. Production cross-sections of SUSY particles from p-p collisions of  $\sqrt{s} = 13$  TeV [9].

less produced at the same masses. For this reason, slepton searches will target lower mass ranges than R-hadron or higgsino searches.

A possible conservation law of SUSY is often called R-parity, and for each particle it can be calculated by the equation:

$$P_R = (-1)^{3(B-L)+2s} \quad (1.7)$$

where B is the baryon number, L is the lepton number, and s is the spin of the particle. If R-parity is conserved in every interaction, then supersymmetric particles would always be pair-produced in proton-proton collisions.

At first, it was thought supersymmetric particles would have the same masses as their Standard Model counterparts. For example, selectrons would have rest masses

matching those of SM electrons, or 0.511 MeV. However, selectrons of this mass have been excluded through experiment [10], meaning SUSY must be a broken symmetry. If it is a 'softly' broken symmetry, then SUSY can still exist as a BSM model. The soft supersymmetry breaking also allows for sparticles to be heavier than their SM counterparts, opening up a wide range of mass phase-space in which we hope to discover SUSY particles. Another facet of the phase space is that of particle lifetime. Since previous SUSY searches mostly focused on promptly-decaying sparticles, the phase-space of longer lifetimes is relatively unexplored. The lifetimes of SUSY particles naturally vary just the same as those of SM particles. This thesis explores a search for pair-produced, long-lived staus, as portrayed in Figure 1.6.

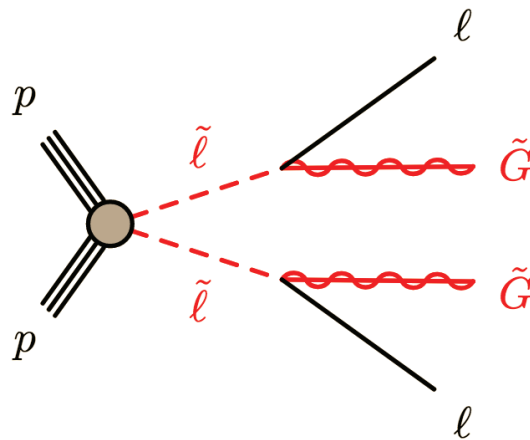


FIGURE 1.6. Feynman diagram of long-lived staus.

## CHAPTER II

### THE LHC AND THE ATLAS EXPERIMENT

This chapter will describe the experiment necessary to produce and study new, heavy, long-lived particles. It will cover the Large Hadron Collider in Section 2.1, and the ATLAS detector in Section 2.2, with particular emphasis on the Pixel Detector subsystem (Section 2.2.2).

#### 2.1 LARGE HADRON COLLIDER

The Large Hadron Collider (LHC) is the world's largest particle collider. Located at the border of Switzerland and France, it is a circular collider, stretching 27 km in circumference and is located 100 meters below the Earth's surface. The collider consists of two parallel beamlines which run in opposite directions, and four interaction points where proton-proton collisions occur. Protons are sourced from hydrogen gas which is stripped of electrons in Linac4, and then these protons are sent through increasingly larger, and more energetic, particle accelerators. These accelerators are the Proton Synchrotron Booster (PSB), the Proton Synchrotron (PS), the Super Proton Synchrotron (SPS), and lastly the LHC. During the PS step, the protons are separated into bunches of  $10^{11}$ , and two streams of proton bunches are sent so that one stream runs clockwise and the other counter-clockwise. In the LHC, the acceleration of protons is performed by radiofrequency cavities which emit electromagnetic fields. The LHC also has dipole magnets which can deflect the path of charged particles. This ensures the protons travel around the circular LHC instead of in a straight line. It also serves to focus the proton beam and keep the bunches concentrated. In the LHC, the protons are accelerated to a final energy

of 6.5 TeV. Then, as proton bunches from different directions enter the interaction points and collide, the total collision energies will have 13 TeV as their center-of-mass energy. The LHC contains four collision points which are located at four of CERN's experiments, ALICE (studying heavy-ion physics), LHCb (b-quark physics), CMS, and ATLAS, the last two of which both study SM and BSM signatures in proton-proton collisions.

## 2.2 ATLAS DETECTOR

ATLAS is a cylindrical, general purpose detector with forward-backward symmetry centered at an interaction point at the LHC. It is made up of several detector subsystems designed to provide full coverage to record the high-energy physics events. The first of the subsystems in the Inner Detector, which collects the track signatures of charged particles to a radius of 1.08 meters. Then the Calorimeter system records the energy deposits of charged particles, photons, and strongly-coupled particles in the LAr and HCAL. The Muon Spectrometer is set at the outer edges of the detector, to record muon signatures. Lastly, ATLAS detector had two magnetic systems, the Central Solenoid magnet and the Toroidal magnet system.

ATLAS uses a right-handed coordinate system with its origin at the nominal interaction point (IP) in the centre of the detector and the  $z$ -axis along the beam pipe. The  $x$ -axis points from the IP to the centre of the LHC ring, and the  $y$ -axis points upwards. Polar coordinates  $(r, \phi)$  are used in the transverse plane,  $\phi$  being the azimuthal angle around the  $z$ -axis. The pseudorapidity is defined in terms of the polar angle  $\theta$  as  $\eta = -\ln \tan(\theta/2)$  and is equal to the rapidity  $y = \frac{1}{2} \ln \left( \frac{E+p_z c}{E-p_z c} \right)$  in the relativistic limit. Angular distance is measured in units of  $\Delta R \equiv \sqrt{(\Delta y)^2 + (\Delta \phi)^2}$ .

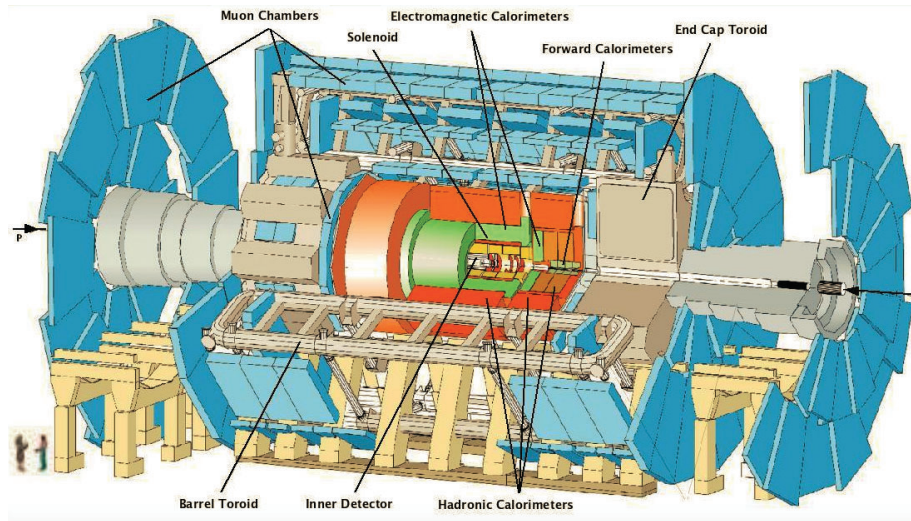


FIGURE 2.1. Side-view of the ATLAS detector

### 2.2.1 *Toroidal and Solenoid Magnet Systems*

ATLAS contains two subsystems which are responsible for maintaining a magnetic field in the detector. The magnetic field is necessary for the measurement of particle momenta, as the paths of charged particles will curve in the presence of a perpendicular magnetic field. From that curvature the particle momenta can later be calculated. The solenoid subsystem wraps around the barrel-section of the Inner Detector, and provides an axial magnetic field of 2 T in the Inner Detector. It has a single coil layer inside a thin aluminium-alloy cylinder and is only 4.5 cm thick. Keeping the solenoid thin means less material is available for particles to scatter off of, introducing unwanted particle showers. The toroidal subsystem consists of one barrel section and two end-caps. The barrel section has eight coils axially aligned between the Tile Calorimeter and the Muon Spectrometer systems, and the two end-caps both contain eight coils each. At its strongest points, the magnetic field

generated by the toroidal system is 4.1 T, though at the MS this field is 1 T strong [11].

### 2.2.2 Inner Detector

The subsystem closest to the beamline is the Inner Detector, which is further made up of three detector systems: the Pixel Detector, the Semiconductor Tracker, and the Transition Radiation Tracker. The systems of the Inner Detector serve to map the tracks of the charged particles traveling away from the interaction point. This allows for the reconstruction of particle vertices and for measurement of particle momenta. A cross-section view is seen in Figure 2.2.

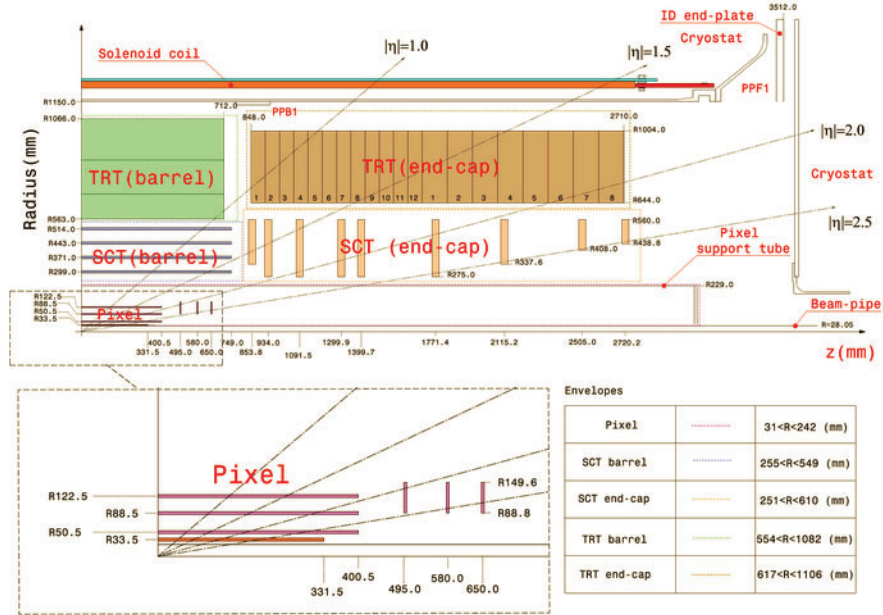


FIGURE 2.2. Cross-section view of the 4-Layer Pixel Detector for Run 2.

The Pixel Detector contains four layers of silicon pixels in the barrel-section. The first is the Insertable B-Layer (IBL), which sits 33mm from the beam line and covers the region  $|\eta| < 3.03$ . The IBL consists of 14 staves which hold 12 million pixels,

which are typically  $50 \mu\text{m}$  by  $250 \mu\text{m}$  in the  $\phi$  by  $z$  directions, respectively. Some pixels are larger, being  $50 \mu\text{m}$  by  $500 \mu\text{m}$  to fill any gaps [12]).

When a charged particle travels through a silicon pixel, it ionizes the silicon and deposits a charge. The amount of deposited charge is measured by Time-over-Threshold (ToT). ToT is a method of processing signal input by the length of time a signal pulse is greater than a preset threshold of charge, see Figure 2.3.

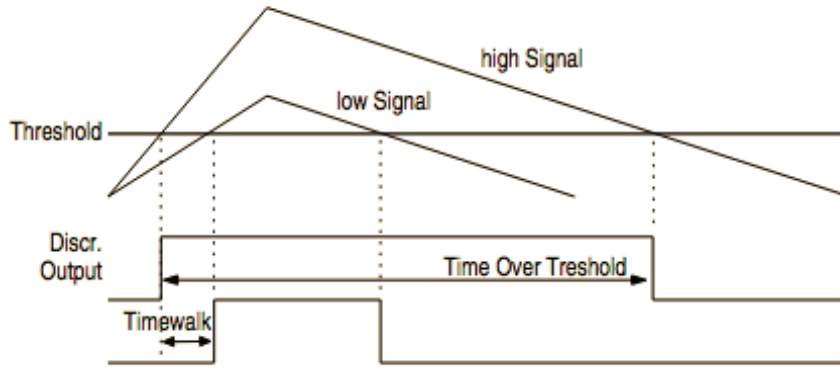


FIGURE 2.3. Diagram of a time-over-threshold measurement. The larger charge signal corresponds to a longer time s. [13]

Since the time span of the signal pulse and the amount of deposited charge are proportional to one another, the front-end chips (FE-I4) which record the pixel data are created to measure this time. The threshold value is regularly calibrated during the data-taking run, and also adjusted over time. Since the Pixel Detector is the subsystem closest to the beamline, it is exposed to the highest levels of radiation damage. Radiation damage reduces the silicon's ability to be ionized, resulting in less deposited charge after radiation damage has occurred. Over the course of Run 2, the analog threshold was lowered from 2550 e to 2000 e in the Insertable B-Layer as it incurred radiation damage to its pixels. Due to its proximity to the beamline, the IBL is exposed to the highest levels of radiation in the ATLAS detector, and so

it was designed to be replaced during long shut-downs of the detector. It also has the highest incidence rates per area from charged particles of all the Pixel layers. To reduce the bandwidth of input signal, the front-end chips of the IBL digitized the TOT values with 4 bits, instead of the 8 bits the three outer Pixel layers used. This set an upper bound of 16 bc for the IBL. The other layers have 8 bits, allowing for ToT values reaching 255. Table 2.1 shows the annual conditions of the Pixel detector layers.

TABLE 2.1. Yearly Pixel Detector settings by layer during Run2 datataking.

Sensor	IBL planar	B-Layer (L0)	L1	L2	Endcap
HV-2015	-80V	250V	150V	150V	150V
HV-2016	-80V	350V	200V	150V	150V
HV-2017	-350V	350V	200V	150V	150V
HV-2018	400V	400V	250V	250V	250V
Temperature-2015	-3c	-2c	-2c	-2c	-7c
Temperature-2016	+15c	-10c	-10c	-10c	-13c
Temperature-2017	-20c	-20c	-20c	-20c	-20c
Temperature-2018	-20c	-20c	-20c	-20c	-20c
Latency-all yrs	ToT <sub>17</sub>	ToT <sub>150</sub>	Tot <sub>256</sub>	ToT <sub>256</sub>	ToT <sub>256</sub>
Analogue threshold-2015	Q>2550e	Q>3500e	Q>3500e	Q>3500e	Q>3500e
Analogue threshold-2016	Q>2550e	Q>5000e	Q>3500e	Q>3500e	Q>3500e
Analogue threshold-2017	Q>2550e	Q>5000e	Q>3500e	Q>3500e	Q>4500e
Analogue threshold-2018	Q>42000e	Q>4300e+5000e	Q>3500e	Q>3500e	Q>3500e

The next three layers of the barrel-section of the Pixel Detector are the B-Layer, Layer 1, and Layer 2. These are positioned at 50.5mm, 88.5mm, and 122.5mm radially outward from the beamline, and cover the region  $n |\eta| < 2.0$ , as seen in Figure 2.4. The pixels of the outer three layers are slightly larger than the typical IBL pixel, measuring  $50 \mu\text{m}$  by  $300 \mu\text{m}$ . Finally, the end-cap sections of the Pixel Detector are arranged forward and backward of the barrel-section. They serve to extend the detector's tracking capabilities in the high-eta regions. At each end-cap, three circular disks are positioned perpendicular to the beamline. They extend

radially from 88.8 mm to 149.6 mm, and are set 495 mm, 580 mm, and 650 mm away from the interaction point [14].

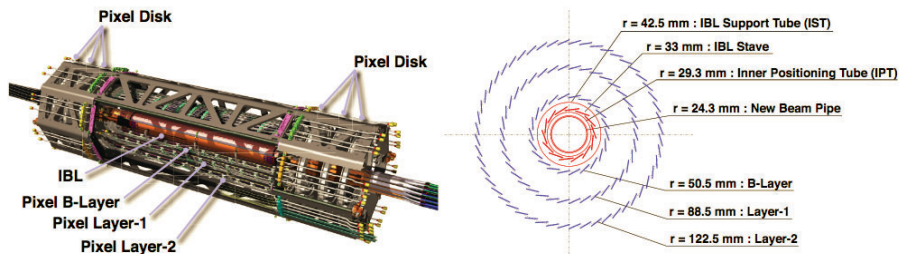


FIGURE 2.4. Schematic view of the Inner Detector, with an enlarged view of the Pixel Detector.

The next subsystem of the Inner Detector is the Semiconductor Tracker (SCT). It also uses silicon detectors to track the passage of charged particles, but uses 'strips' instead of pixels. Each strip is  $80 \mu\text{m}$  wide and 123.2 mm long. In the axial direction 768 strips are placed side by side. A second set of strips is placed with a 80 mrad rotation in alignment, creating a grid-like structure of overlapping strips. This creates one layer of the SCT's four barrel layers, which together cover  $|\eta| < 1.4$ . The SCT also has nine endcap layers which record tracks in the forward regions, extending the SCT's coverage to  $|\eta| < 2.5$  [15].

The last subsystem of the Inner Detector is the Transition Radiation Tracker (TRT). The TRT uses 370,000 drift tubes instead of silicon technology to detect charged particles. Each drift tube has a 2 mm radius and has a conductive wire in its center which is held at a voltage of -1500 V. The tubes are filled with scintillating gas, and when a charged particle ionizes the gas, the electric signal is recorded by the central wire. These signals create a trace of the particle through the drift-tubes. The barrel section has 52544 tubes which are 150 cm long arranged in the axial direction, and the endcaps have 319488 tubes which are 39 to 55 cm long, arranged radially.

Any charged particle within  $|\eta| < 2.5$  and  $p_T > 0.5$  GeV will cross 40 drift-tubes in its passage through the TRT [15].

System	Position	Area (m <sup>2</sup> )	Resolution $\sigma$ ( $\mu\text{m}$ )	Channels (10 <sup>6</sup> )	$\eta$ coverage
Pixels	1 removable barrel layer	0.2	$R\phi = 12, z = 66$	16	$\pm 2.5$
	2 barrel layers	1.4	$R\phi = 12, z = 66$	81	$\pm 1.7$
	4 end-cap disks on each side	0.7	$R\phi = 12, R = 77$	43	1.7-2.5
Silicon strips	4 barrel layers	34.4	$R\phi = 16, z = 580$	3.2	$\pm 1.4$
	9 end-cap wheels on each side	26.7	$R\phi = 16, R = 580$	3.0	1.4-2.5
TRT	Axial barrel straws		170 (per straw)	0.1	$\pm 0.7$
	Radial end-cap straws		170 (per straw)	0.32	0.7-2.5
	36 straws per track				

FIGURE 2.5. Table of Inner Detector subsystem geometries. [14]

### 2.2.3 Calorimeters

There are two calorimeter subsystems in the ATLAS detector. They serve to measure the energies of most particles. The first is the Liquid Argon Calorimeter (LAr), which was developed to mainly capture photons and charged particles, though it does interact with neutral, hadronic particles. The barrel section wraps radially around the Inner Detector, and has an inner and outer radius of 1.15m and 2.25m. It is comprised of layers of steel and liquid argon, the latter of which has a radiation length of 14.2 cm [16]. When photons, electrons, and hadrons pass through the LAr, they produce showers of lower energy photons and electrons after interacting with the steel plates. These showers produce electric currents after ionizing the liquid argon. The currents then serve to measure the energies of the incident particles in the calorimeter. A cooling system is present to keep the argon at -184 degrees Celcius, so that it remains in its liquid phase.

The second calorimeter subsystem is the Tile Calorimeter. It is comprised of 420,000 plastic scintillator tiles which are sandwiched between layers of steel [17]. When the incident hadrons interact with the steel plates they generate showers. These showers produce photons in the plastic scintillators, which are converted to an electric current. Again, this electric current produces the measurement of deposited energy in the calorimeters

#### *2.2.4 Muon Spectrometer*

The outermost subsystem of the ATLAS detector is the Muon Spectrometer (MS). As muons are lightly-interacting particles compared to electrons, they can traverse the radial length of the ATLAS detector and only lose 3 GeV of energy before reaching the MS. Thus, a separate detector system is necessary to detect muons. The MS uses drift-tube technology, like the TRT, though these cover a wider area [18].

### 2.3 TRIGGER AND DATA ACQUISITION SYSTEM

ATLAS sees 1.7 billion proton-proton events per second, the majority of which are low-energy events that are already well-studied. Only highly-energetic events, or those with interesting signatures are kept for permanent storage. The Trigger and Data Acquisition system (TDAQ) is used to sort through all the electronic data of each event. It is organizationally split into two levels, based on the subdetector processing times. The first-level is a hardware trigger which accepts on the order of 100,000 events per second, then the second-level software trigger whittles this number down to the order of 1000 events per second for permanent storage.

The Level-1 Trigger system reads in the electronic data from the MS and calorimeter subdetectors to determine if an event should be processed further. The

read-in rate is 40 MHz [19], and due to this high volume of incoming events, only 2  $\mu$ s of time is allowed for Level-1 to make a decision. As much of the time is used by signal traveling from the subdetectors to the TDAQ system, the signal analysis must be computationally simple in order to be read fast. It uses firmware technology to process this data quickly. Triggers at Level-1 are physics objects such as  $\sum E_T$ ,  $\tau$ ,  $E_T^{\text{miss}}$ , muons, and jets. The  $E_T^{\text{miss}}$  trigger is of particular interest to this thesis, as it is used in the ditrack analysis.  $E_T^{\text{miss}}$ , or missing transverse momentum, is the transverse momentum which is not recorded by the ATLAS detector. Since collisions are created from two protons each with  $\sqrt{s} = 6.5$  TeV going in opposite directions, the total momentum in the transverse direction is zero. By summing all the momentum measured by the detector during one bunch-crossing, we obtain a measurement of  $E_T^{\text{miss}}$ . This measurement only uses the information from the LAr and Tile Calorimeters and is called the Online  $E_T^{\text{miss}}$ . A more comprehensive  $E_T^{\text{miss}}$  measurement is generated during the reconstruction stage, see Chapter III. The L1 Trigger whittles down the number of events to a rate of 100 kHz or less. Next, the High-Level Trigger (HLT) is a software-based trigger which can add additional information about the selected events. The HLT has access to full granularity tracking data from the Inner Detector, as well as calorimeter and muon data. Using this, it can apply more computationally complicated decisions to reduce the rate of events from 100 kHz to 3 kHz, which are then passed to the Data Acquisition system (DAQ). The DAQ is given the triggered events, and it stores them to disk.

## CHAPTER III

### RECONSTRUCTION

Reconstruction is a process through which patterns in the electronic detector data are identified and assigned to physics objects. This chapter will cover the various types of signatures left by particles, and how they are reconstructed into physics objects, including jets (Section 3.2), missing transverse momentum (Section 3.3), muons (Section 3.4), and tracks (Section 3.5). The measurement of a track's ionization energy loss, or  $dE/dx$ , is further covered in Section 3.5.1, since it is a vital selection in the search for long-lived taus this dissertation covers.

#### 3.1 EVENT RECONSTRUCTION

After events have been accepted by the Trigger and readout by the DAQ system, the electronic data from the detector is reconstructed into physics objects. These objects include tracks, jets, muons, and  $E_T^{\text{miss}}$ , which are especially relevant to the physics analysis this thesis describes. Figure 3.1 shows different particle signatures in the ATLAS detector which are modeled by the physics objects. In the figure solid lines show interactions with the subdetectors, while dotted lines mean the subdetector did not register the particle. As seen in the diagram, hadrons, photons, and electrons will all produce showers of other particles in the calorimeters. As photons and electrons are electromagnetically-interacting particles, they both shower in the EM or LAr Calorimeter. Protons will also shower in the EM calorimeter due to their electric charge, though this was not included in the diagram. Protons and neutrons produce jets in the Hadronic or Tile calorimeter since hadrons are strongly-interacting. Both the photon and neutron leave no track in the Inner Detector as they

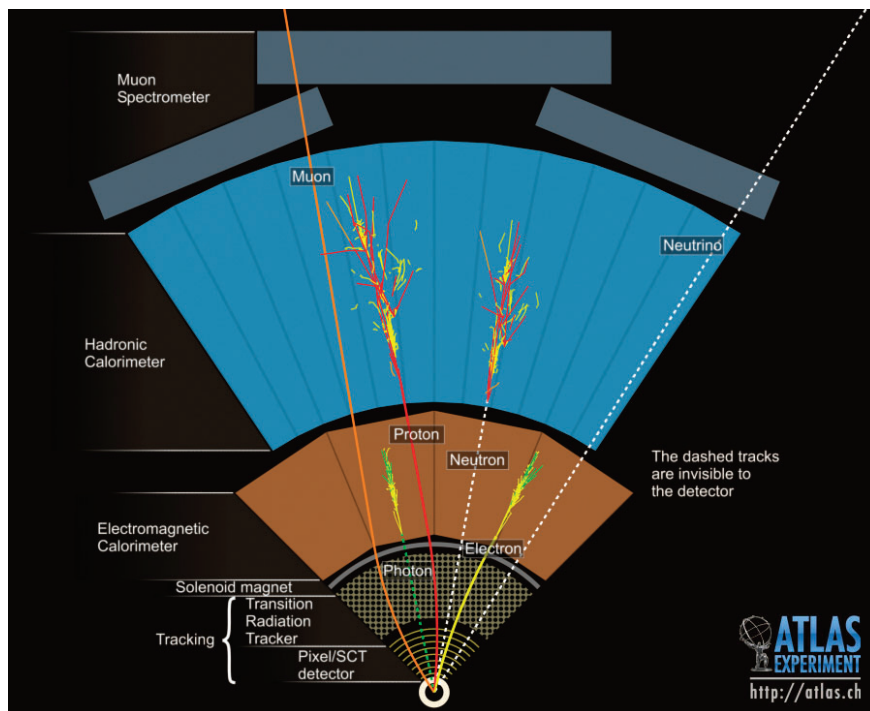


FIGURE 3.1. Cross-sectional view of the ATLAS detector, with various particle signatures depicted. [20].

are electrically neutral. Muons are 200 times heavier than electrons, and minimally interacting so they deposit very little energy in either calorimeter. Instead, their main signature is a track which is detected by the Inner Detector and the Muon Spectrometer systems. Lastly, the neutral, weakly-interacting neutrino is undetected by the ATLAS subdetectors.

### 3.2 JETS

Jet objects are reconstructed from both calorimeter and Inner Detector data. A jet has a cone-like shape, with the angle of the center line to edge is defined as  $\Delta R$ :

$$\Delta R = \sqrt{(\Delta\eta)^2 + (\Delta\phi)^2} \quad (3.1)$$

Here,  $\phi$  is the azimuthal angle and  $\eta$  is the pseudorapidity. A standard ATLAS jet has a defined  $\Delta R$  of 0.4, and this was the same value used for the long-lived stau analysis.

The smallest detector units of the LAr and Tile Calorimeters are called cells. When a jet hits a calorimeter multiple layers will detect it, and more than one cell per layer may record hits. This collection of hit cells is called a topocluster. The reconstruction algorithm which forms distinct jet objects from the topocluster is called the anti- $k_T$  algorithm. Some track objects are also included along with the topocluster input, after subtracting the track's expected energy deposits in the calorimeter. The tracks must be high-quality tracks, with at least nine hits in the SCT detector, and cannot be already matched to electrons or muons. Lastly, the tracks must have momenta above 0.5 GeV, to ensure the particle is energetic enough to deposit energy in the calorimeter, and below 40 GeV, as the highly-energetic particles are problematic for removing their expected energy deposits from topoclusters [21]. Figure 3.2 shows an example output of the algorithm, where recorded hits are portrayed by vertical columns. The jets which are reconstructed from those hits are differentiated by color. Where some overlap of the jets occurs, the leading- $p_T$  jets dominate and project a circle on the 2D plane, while the subleading jets form crescents that curve around the leading jet (i.e. the green jet is leading, the magenta is subleading). With this, the jets are distinctly defined.

### 3.3 MISSING TRANSVERSE MOMENTUM

Missing transverse momentum, or  $E_T^{\text{miss}}$ , is the amount of transverse momentum not detected by the ATLAS detector. It can result from particles which do not interact with the detector, such as neutrinos or the theorized lightest neutralino

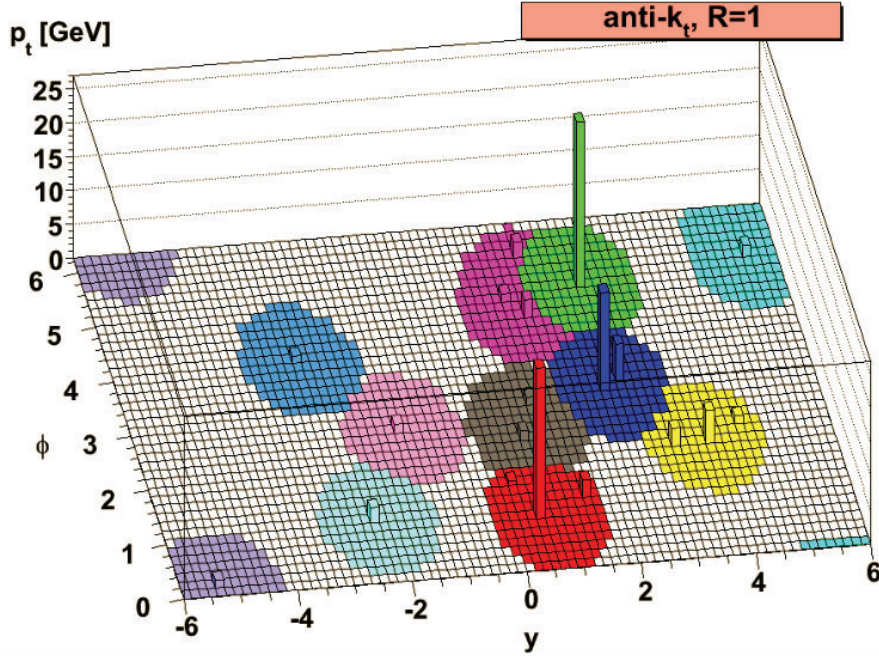


FIGURE 3.2. Jet reconstructions from calorimeter cells using the anti-kT algorithm [22].

of SUSY, or from mismeasurements by the detector. As the transverse momenta of the colliding protons are both 6.5 TeV in opposite directions, the net transverse momentum of any event is zero. Thus, if the total transverse momentum as recorded by the detector is not zero, this imbalance is called  $E_T^{\text{miss}}$ .

A rudimentary measurement of  $E_T^{\text{miss}}$  is already created at the Trigger-level, as described in Section 2.3. The more comprehensive measurement is called Offline  $E_T^{\text{miss}}$ . Offline  $E_T^{\text{miss}}$  includes all the transverse momenta terms from distinct, reconstructed electrons, photons, tau-leptons, and muons. Then, jet objects which are not accounted for by the previous terms are included. Lastly, any tracks which are not accounted for by the previous objects are added to the  $E_T^{\text{miss}}$  calculation. All physics objects are required to pass several kinematic cuts for medium reconstruction quality [23].

### 3.4 MUONS

Muons are characterized by leaving hits in the Inner Detector and the Muon Spectrometer, with very little energy deposits in the calorimeters. Muons are reconstructed by matching ID tracks to MS tracks such that the combination track passes several muon-quality requirements [24].

### 3.5 TRACKS

Tracks note the passage of charged particles in the Inner Detector (ID). As charged particles move through a magnetic field, provided by the Toroidal and Solenoid systems, the path bends along a helix due to the Lorentz force:

$$\vec{F} = q\vec{v} \times \vec{B} \tag{3.2}$$

where  $F$  is the magnetic force on the charged particle,  $q$  the electric charge,  $v$  the velocity, and  $B$  the magnetic field strength. In the ID the magnetic field is well-documented. Then, using the hits recorded by the ID subdetectors, the helical path of the track is mapped out. From this path, the azimuthal and polar angles,  $\phi$  and  $\theta$  are derived. Also, the transverse and azimuthal impact parameters  $d_0$  and  $z_0$  are found. These impact parameters are measures of the closest distance between the track and the vertex where the p-p collision occurred, and they serve as a measure of where the track originated. Lastly, from the curvature of the path the ratio of  $q/p$  is found. Since multi-charged particles are not a signature or source of background for the long-lived stau analysis, an assumption is made that the track particle has a single electric charge. Then, this  $q/p$  ratio gives us the sign of the electric charge, as well as the track's momentum.

### 3.5.1 Ionization Energy

An additional track measurement is used for this thesis which is non-standard among most ATLAS analyses. This measurement is  $dE/dx$ , the amount of energy lost to ionization per thickness as the charged particle travels through a material. Specifically, the  $dE/dx$  measurement from the Pixel Detector is used. The Bethe-Bloch equation characterizes the relation between most probable value of  $dE/dx$  and the particle's speed through a given material. When that material is very thin silicon, as is used in the Pixel Detector (  $250 \mu\text{m}$ ), the  $dE/dx$  curve flattens, as is shown in Figure 3.3. This figure plots the most probable values of  $dE/dx$  from a muon through several thin silicon widths. Despite the wide distribution of muon speeds, the  $\langle dE/dx \rangle_{MPV}$  is mostly constant for  $\beta\gamma > 4$ . The Pixel Detector was intentionally designed so that light, relativistic SM particles would be minimally ionizing particles (MIPs). However, heavier particles of similar momenta, like long-lived staus, will be slower, reaching higher  $\langle dE/dx \rangle_{MPV}$  values.

The particle's speed, coupled with a momentum measurement, allows for the calculation of the particle's mass using the  $dE/dx$ . This  $dE/dx$ -derived mass later serves as an important track quality in the search for long-lived staus.

Now, the  $dE/dx$  probability distribution functions of 500 MeV pions in thin silicon can be seen in Figure 3.4. These probabilities fall on a Landau distribution, where the most probable value is where the distribution peaks. The Landau distribution also has a long tail, meaning it is more probable that the hits will average a  $dE/dx$  measurement greater than the distribution's peak. To combat this a truncated mean is used for ionization energy loss, where typically the lowest 70% energy deposit measurements are used [25]. This is done to combat the influence of the Landau distribution's long tail, and make the distribution more like a Gaussian.

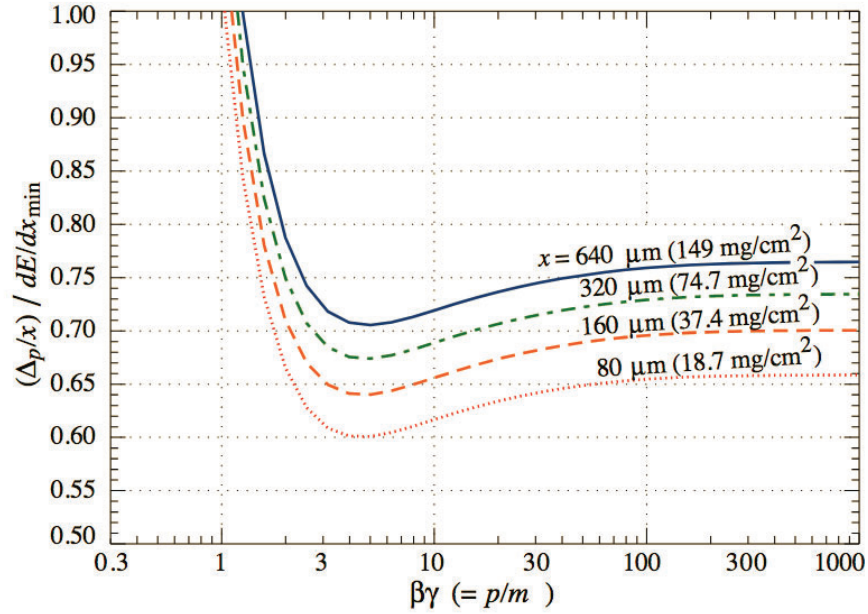


FIGURE 3.3. Energy losses in silicon for muons of various kinetic energies [8].

As the Pixel Detector has only four layers in the central barrel, and three in the Pixel's endcaps, a limited number of 'good clusters' can be used. To calculate the track- $dE/dx$ , the analysis uses a truncated mean where the greatest  $dE/dx$  cluster is discarded, or two greatest if there are more than four clusters. The remaining cluster  $dE/dx$  values are averaged to produce an approximate of the most probable value of the Landau distribution. The resolution of these  $dE/dx$  measurements is about 10% [25].

Over the course of the data-taking run, the silicon pixel chips degrade due to radiation damage, as mentioned in Chapter II. Also, tracks with higher  $\eta$  are more likely to have higher  $dE/dx$  due to second-order effects in thin silicon sensors. These effects, as well as any changing detector conditions require the  $dE/dx$  values to be calibrated before they are used as part of an analysis. This calibration is done

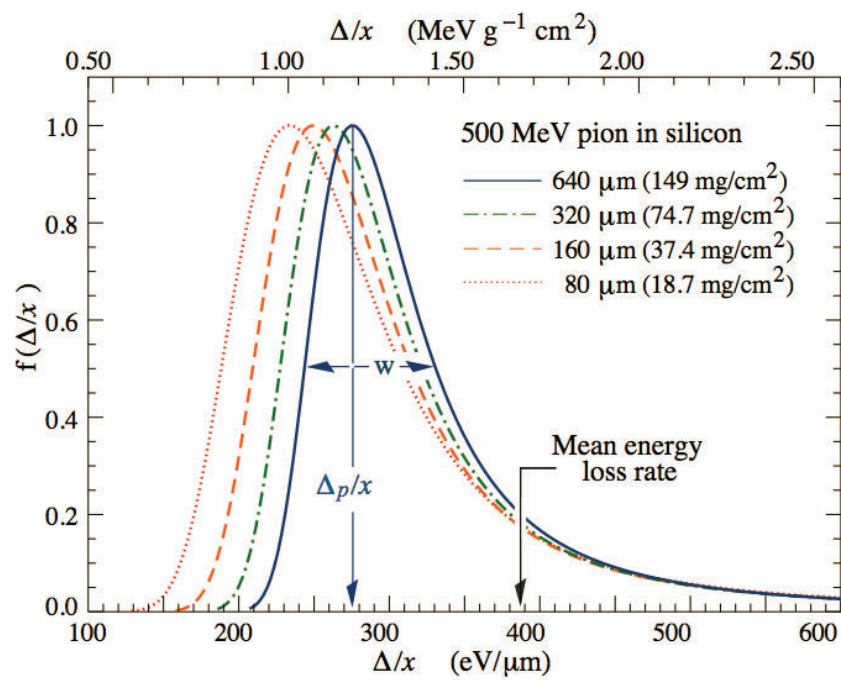


FIGURE 3.4. Straggling functions for the energy loss distribution of a 500 MeV pion for various thicknesses of silicon, with each distribution normalized by modal value [8].

by sampling MIP data events at different data-taking periods, and applying the corrections to equalize the most probable  $dE/dx$  value across eta and time.

## CHAPTER IV

### DITRACK ANALYSIS

This chapter covers the selection criteria of the search for long-lived staus, and its development. First, the analysis history and motivation is covered in Section 4.1. Then the actual selections are covered in chronological order, with the event-level selections covered in Section 4.2, then the track-level selections in Section 4.3. The last analysis selection is the application of mass windows, as explained in Section 4.4. These mass windows were chosen after a study showed the analysis was best served with two signal regions, and this study is covered in Section 4.5. Finally, the selections are summarized in Section 4.6 and expected signal yields are shown in Section 4.7.

#### 4.1 MOTIVATION

The ditrack analysis is an extension of an earlier  $dE/dx$  analysis for long-lived SUSY particles. The first iteration used  $dE/dx$  to search for R-hadrons, charginos, and staus while only focusing on finding one candidate track [26]. A 2016 subset of Run 2 data was processed first [27] and a promising excess of events was found in the signal region. After the full Run 2 data was analysed, a slight excess was still present, though was not considered statistically significant in comparison to Standard Model background. This excess can be seen in the high-mass range of Figure 4.1. In order to explore this phase space, the ditrack extension was proposed.

R-hadrons and neutralinos and charginos, like staus, are also produced two at a time, however, they are equally likely to be electrically neutral as they are electrically charged. Staus on the other hand, are always pair-produced as two charged particles, capable of producing two tracks in the Inner Detector. So, the ditrack extension of

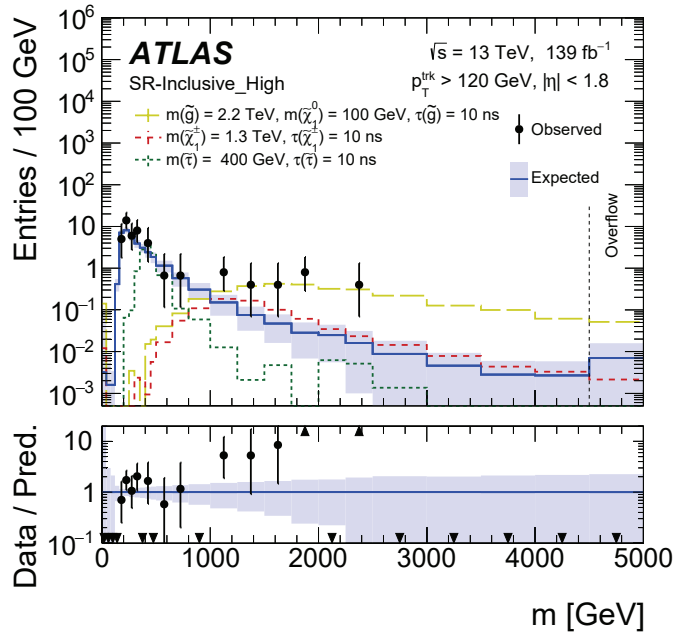


FIGURE 4.1. The observed mass distribution in the Inclusive-High signal-region bins observed in [26]. Several representative signal models are overlaid the expected background and the observed events in data.

the first  $dE/dx$  analysis has always been more sensitive to staus than R-hadrons or charginos, thus staus have been the main focus.

The requirement of a second candidate track in the ditrack analysis allows for the loosening of some cuts without sacrificing the overall background rejection. These loosened cuts include the offline  $E_T^{\text{miss}}$  and the track-level ionizations and transverse masses. The ditrack analysis has two signal regions; a Discovery SR and an Exclusion SR. These two signal regions differ only in the tracks' ionizations, which are noted in Table 4.3, and their  $dE/dx$ -mass windows, noted in Section 4.4.

## 4.2 EVENT-LEVEL SELECTIONS

All must pass the lowest, unrescaled  $E_T^{\text{miss}}$  trigger. A full list of triggers is Run 2 triggers is shown in Table 4.2 since the requirements changed over the four years of Run 2. All events must be in the Good Runs List (meaning all ATLAS subdetectors were in working order, the records of which are noted in Table 4.1) and pass standard event-cleaning. If the SCT detector, or the LAr or Tile Calorimeters flag a possible corruption in one event, that event is removed. Events must also pass a jet-cleaning procedure to reject false calorimeter hits or non-collision backgrounds. Jets can have a variety of characteristics in data, which are listed below.

TABLE 4.1. Good run lists for the data used in this analysis.

Year	Good Run List
2015	data15_13TeV.periodAllYear_DetStatus-v89-pro21-02_Unknown_PHYS_StandardGRL_All_Good_25ns.xml
2016	data16_13TeV.periodAllYear_DetStatus-v89-pro21-01_DQDefects-00-02-04_PHYS_StandardGRL_All_Good_25ns.xml
2017	data17_13TeV.periodAllYear_DetStatus-v99-pro22-01_Unknown_PHYS_StandardGRL_All_Good_25ns_TriggerNo17e33prim.xml
2018	data18_13TeV.periodAllYear_DetStatus-v102-pro22-04_Unknown_PHYS_StandardGRL_All_Good_25ns_TriggerNo17e33prim.xml

- $\langle Q \rangle$ : the energy-squared weighted average of the pulse quality of the cells in the jet;
- $f_Q^{\text{LAr}}$ : fraction of the energy in the LAr cells of the jet with poor signal shape quality;
- $E_{\text{neg}}$ : sum of all cells in the jet with negative energy;
- $f_{\text{EM}}$ : ratio of the energy in the electromagnetic calorimeter to the total energy of the jet;
- $f_{\text{HEC}}$ : ratio of the energy in the Hadronic end-cap calorimeter to the total energy of the jet;
- $f_{\text{max}}$ : maximum energy fraction in any single calorimeter layer;
- CHF: sum of the track  $p_T$  in the jet, divided by the jet calorimeter  $p_T$

However, standard jet-cleaning procedures were found to also reject signal from charged LLPs. Standard jets are emitted near the collision point, while a jet from an LLP will be produced farther from the collision point. An alternative jet-cleaning method was needed, named SuperLooseBadLLP in the Athena framework, and its requirements are listed below.

- $(f_{\text{max}} > 0.99)$  and  $(\text{jet } |\eta| < 2)$
- $(E_{\text{neg}} > 60 \text{ GeV})$  and  $(f_{\text{max}} > 0.85)$
- $(f_{\text{HEC}} > 0.5)$  and  $(\langle Q \rangle > 0.5)$  and  $(f_Q^{\text{LAr}}/65535 > 0.8)$
- $(f_{\text{EM}} > 0.95)$  and  $(f_Q^{\text{LAr}} > 0.8)$  and  $(\text{jet } |\eta| < 2.8)$  and  $(f_Q^{\text{LAr}}/65535 > 0.8)$

Lastly, all events are required to contain a primary vertex (PV), a point from which an events associated particles originate from. Since the presence of pileup means one event will have multiple associated vertices (during Run 2, pileup averaged 36), the vertex with the highest associated sum of  $p_T$  is designated as the PV.

---



---

HLT_noalg_L1J400
HLT_xe70
HLT_xe70_mht
HLT_xe90_mht_L1XE50
HLT_xe100_mht_L1XE50
HLT_xe110_mht_L1XE50
HLT_xe90_pufit_L1XE50
HLT_xe110_pufit_L1XE55
HLT_xe110_pufit_L1XE50
HLT_xe100_pufit_L1XE50
HLT_xe100_pufit_L1XE55
HLT_xe110_pufit_xe70_L1XE50
HLT_xe120_pufit_L1XE50
HLT_xe110_pufit_xe65_L1XE50

---



---

TABLE 4.2. List of unprescaled lowest  $E_T^{\text{miss}}$  HLT trigger decisions.

Events are required to have offline  $E_T^{\text{miss}} > 20$  GeV. For stable lifetimes, pair-produced staus leave very little energy in the calorimeter. Only with the addition of initial-state radiation do we expect to see events which will pass the online  $E_T^{\text{miss}}$  triggers. For metastable lifetimes, the visible decay products allow for more offline  $E_T^{\text{miss}}$  in the event, lessening the need for the event to have associated initial-state radiation. A comparison of the ditrack and single-track's final offline  $E_T^{\text{miss}}$  measurements can be seen in Figure 4.2, where the ditrack analysis is shown to be more sensitive at lower  $E_T^{\text{miss}}$ . Selections which build upon only one track require  $E_T^{\text{miss}} > 170$  GeV to reject background, which also reduced signal acceptance, see Figure 4.3. However, selecting for a second candidate track in the same event has a great effect in rejecting background, see Table 4.7. Thus, the offline  $E_T^{\text{miss}}$  threshold

is loosened to 20 GeV, to include events which were not accepted in the first  $dE/dx$  analysis due to their offline  $E_T^{\text{miss}}$ . The nominal value of 20 GeV is used, instead of having no offline  $E_T^{\text{miss}}$  cut at all, because the track's transverse mass depends on having a well-defined  $E_T^{\text{miss}}$ .

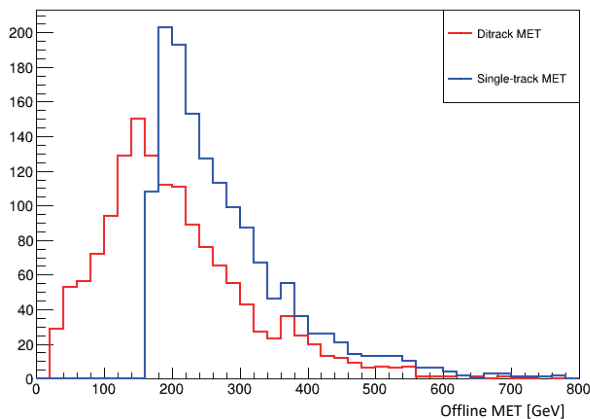


FIGURE 4.2. Comparison of offline MET from a simulated 400 GeV stau with 10ns lifetime, after the single-track analysis selection is applied (shown in blue) and the ditrack selection (shown in red). For both cases, all event and track-level selections were applied, but mass windows were not.

### 4.3 TRACK-LEVEL SELECTIONS

Events are required to have at least two candidate tracks. Each track must pass a series of selections to ensure track quality and veto non-track objects. The event is required to contain at least one track that passes the transverse mass requirement, as described in Section 4.3.2. Lastly, the tracks must all pass the ionization requirements of the Exclusion and Discovery SRs, which are described in Section 4.3.3. Once an event with two candidate tracks is found, the tracks are required to have opposite electrical charges, and pass an invariant mass threshold.

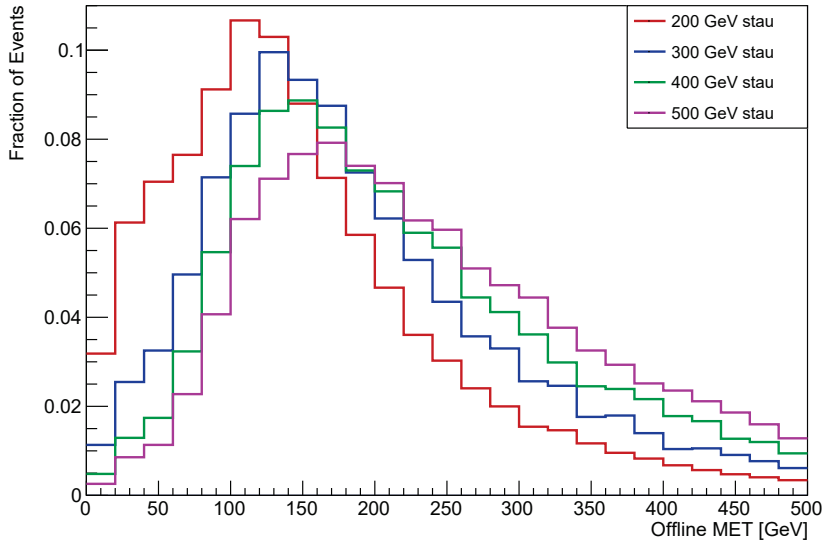


FIGURE 4.3. Offline  $E_T^{\text{miss}}$  for stau samples with 10ns lifetimes and masses of 200, 300, 400, 500 GeV. All event-level requirements including the trigger,  $E_T^{\text{miss}}$ , and event/jet cleaning requirements are applied.

### 4.3.1 Track-Quality Selections and Vetos

Firstly, all considered tracks have to be associated with the event's primary vertex. This was done using the LooseTrackVertexAssociationTool of the Athena framework. At least two hits from the Pixel Detector must have been accepted for use in the  $dE/dx$  calculation. Each track has either an IBL or B-layer cluster of hits, to avoid accepting tracks from interactions with the detector material between Pixel Detector layers. None of the track's hits in the Pixel layers are allowed to be split or shared with another track. When two tracks have some overlap at a Pixel Detector layer, the reconstruction algorithm may assign one hit to both tracks. This is called a shared hit. When the reconstruction algorithm considers the hit for being 'shared' but decides against, this hit is called a split hit, to indicate the possible overlap. Hits from overlapped tracks would read as more energetic, which would artificially

inflate the calculated Pixel- $dE/dx$  value. Next, the tracks are required to have at least five hits in the SCT layers, as a study found it rejected likely background from non-prompt particles and those from detector material-interactions.

In the Inner Detector, jets and tracks share some characteristics. However, our signal will produce only isolated tracks. To reject all jet-like activity, an isolation veto was applied. Inside a spatial cone of  $\delta R = 0.3$  centered around the candidate track, the momenta from all additional track objects was summed up. If this sum exceeded 5 GeV, the object was determined to be a jet and was discarded.

Next, to ensure the candidate tracks were reconstructed well, a momentum uncertainty cut was applied. As momentum reconstruction is more precise at lower momenta, the cut has to depend on momenta.

$$\sigma_p < \max\left(10\%, \left(-1\% + 90\% \times \frac{|p|}{\text{TeV}}\right)\right) \text{ and } \sigma_p < 200\% \quad (4.1)$$

where  $\sigma_p = \delta(q/p)/(q/p)$ .

Highly-energetic electrons will produce jets as they travel through the detector. The presence of these jets is then used to identify a track as belonging to an electron. This is done by considering the closest jet with  $p_T > 20$  GeV within a spatial cone of  $\delta R = 0.4$ . If 95% or more of the total jet energy matches the jet energy in the EM calorimeter, then the track is likely from an electron, as is vetoed. Similarly, a hadronic veto is implemented if the same closest jet has a total jet energy greater than the track momentum. This is because the signal particles are not expected to interact very much with the calorimeters, as they're minimum ionizing particles.

### 4.3.2 Transverse Mass

At least one track in the event is required to have a transverse mass greater than 130 GeV, but no such requirement is made on the second track to increase acceptance for low mass sleptons (see Figure 4.4). As the definition on transverse mass includes a vector-projection component of each track’s four-momentum to the event’s  $E_T^{\text{miss}}$ , the two candidate tracks have different transverse mass distributions, see Figure 4.5. Due to the asymmetrical nature of the tracks’ transverse masses in relation to each other, the transverse mass is only required of one track.

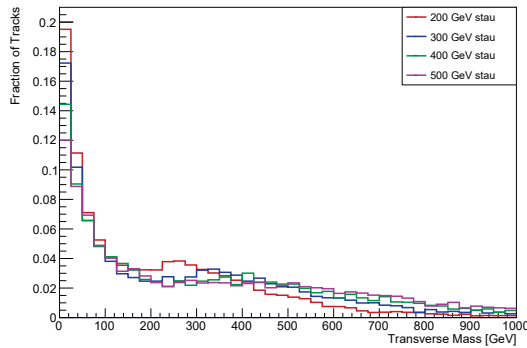


FIGURE 4.4. Individual Slepton Track Transverse Mass. The track transverse mass distributions of both slepton tracks, for sleptons samples with lifetimes of 10ns, and masses of 200, 300, 400, 500 GeV. All event-level requirements including the trigger,  $E_T^{\text{miss}}$ , and jet cleaning requirements are applied. The track is required, for the signal samples, to be matched to a sparticle.

### 4.3.3 Ionization

The ionization requirements are different for the Discovery SR and the Exclusion SR. The Discovery SR requires both candidate tracks to have  $dE/dx$  above 1.7 MeV  $g^{-1}cm^2$ . The Exclusion SR requires at least one track to have  $dE/dx$  greater than 1.6 MeV  $g^{-1}cm^2$ , while the  $dE/dx$  of the second track must be above 1.3

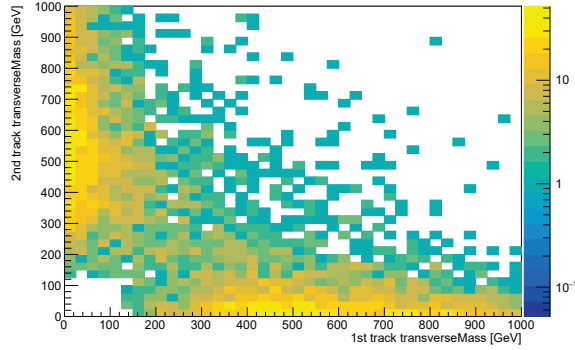


FIGURE 4.5. Event-Level Slepton Track Transverse Mass. Using the 400 GeV, 10 ns stau sample, the correlation of transverse mass of pair-produced stau tracks. All event-level requirements including the trigger,  $E_T^{\text{miss}}$ , and jet cleaning requirements are applied. The track is required, for the signal samples, to be matched to a sparticle.

$dE/dx$ . These requirements are displayed in Table 4.3. The process of optimizing and choosing these particular values is described in Section 4.5.

Signal Region	First Track $dE/dx$ [ $\text{MeV g}^{-1}\text{cm}^2$ ]	Second Track $dE/dx$ [ $\text{MeV g}^{-1}\text{cm}^2$ ]
Discovery	$dE/dx > 1.7$	$dE/dx > 1.7$
Exclusion	$dE/dx > 1.6$	$dE/dx > 1.3$

TABLE 4.3. The ionization requirements of the Discovery and Exclusion SRs.

#### 4.3.4 *Opposite Charge*

The two candidate tracks in each event are required to have opposite electrical charges. If an event contains more than two candidate tracks, only oppositely-charged pairs are used in the following invariant mass requirement. Since signal is comprised of pair-produced sleptons, the product of the two slepton's electrical charges is  $-1$ , while this is not necessarily true of background events with two tracks, see Figure 4.6.

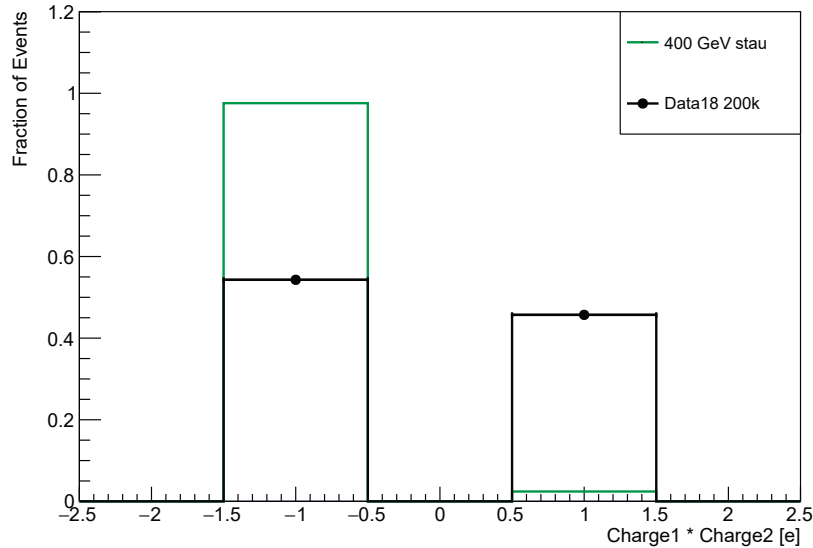


FIGURE 4.6. Plot shows product of two candidate tracks' electrical charges, where  $-1$  indicates the two tracks had opposite electric charges, and  $1$  indicates the two tracks had matching electric charges. All event-level requirements including the trigger,  $E_T^{\text{miss}}$ , and event/jet cleaning requirements are applied. Tracks are required to pass all track-quality requirements, then the two best tracks (in terms of  $p_T$ , then  $dE/dx$ ) are the two candidate tracks. The signal samples are 400 GeV staus with a lifetime of 10 ns. Data is from 200k events in 2018. For the signal samples, the tracks are required to be matched to a sparticle.

### 4.3.5 Invariant Mass

To reject the background events originating from tracks from  $Z$ -boson decays, an invariant mass cut is introduced, see Figure 4.7. Once two candidate tracks are found in the event, the mass of their supposed parent particle is calculated as the invariant mass. The pion mass is used as the assumed mass of the track. If the invariant mass is less than 200 GeV, the event is rejected. If an event contains more than two candidate tracks, then invariant mass values are calculated for each pair of oppositely-charged tracks. In order to maintain signal sensitivity for lower masses, the largest invariant mass value is used to determine if the event passes or not.

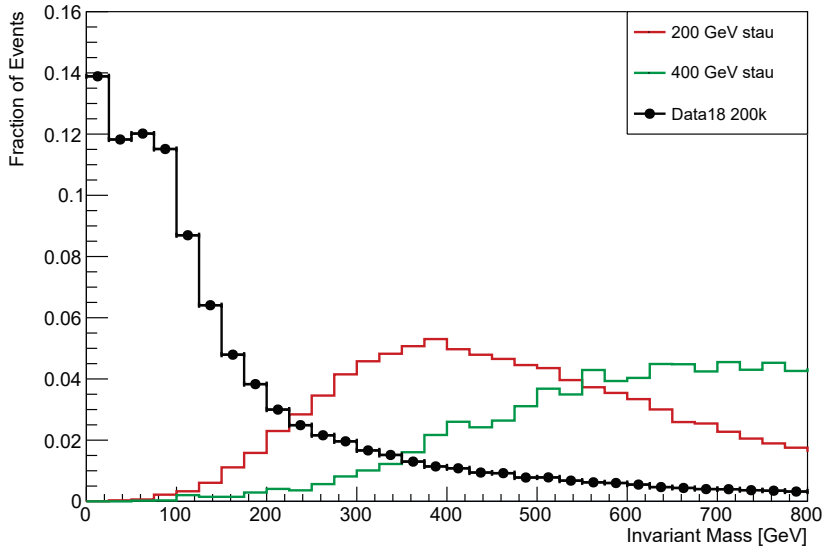


FIGURE 4.7. Invariant mass for stau samples with 10ns lifetimes and masses of 200 and 400 GeV, and for data. All event-level requirements including the trigger,  $E_T^{\text{miss}}$ , and event/jet cleaning requirements are applied. Tracks are required to pass all track-quality requirements, then the two best tracks (in terms of  $p_T$ , then  $dE/dx$ ) are chosen to calculate the invariant mass. Data is from 200k events in 2018.

#### 4.4 DITRACK MASS WINDOWS

The last requirement of the ditrack analysis is a mass window, applied to the  $dE/dx$ -derived mass distribution of the two candidate tracks. As pair-produced sleptons will have the same masses, their  $dE/dx$ -derived mass measurements should have good agreement, within resolution. This is not however true of the irreducible background. To take advantage of this difference in signal and background, a mass window is applied to any potential signal events which pass the other cuts. The mass window is modeled as trapezoidal mass windows. Every mass window has an opening angle and a lower-mass bound, controlling the spread of the acceptance region. An example can be seen in Figure 4.8. No upper-mass bound is applied, as a study found

the highest signal significances occurred with no upper-bound on the mass window.

The mass window parameters were chosen in a process described in Section 4.5.

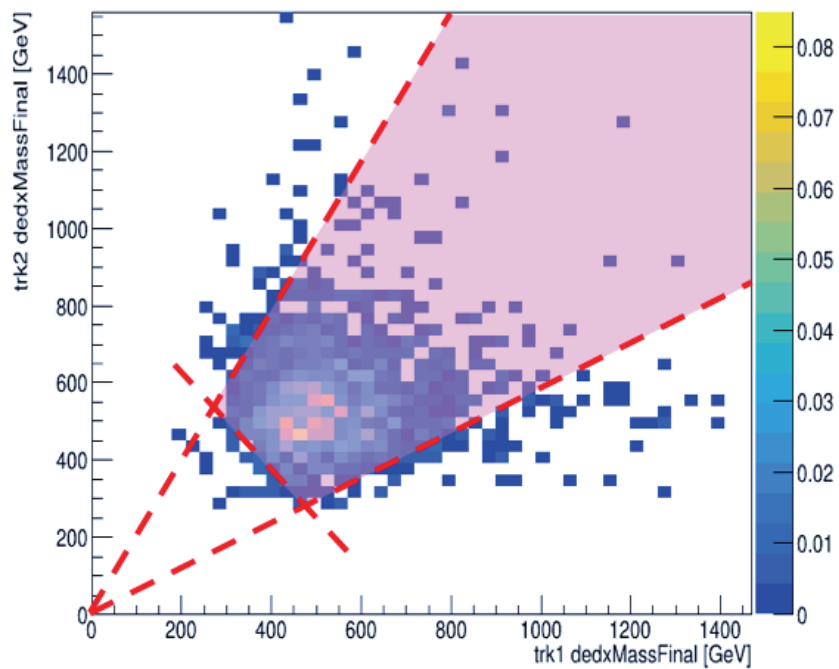


FIGURE 4.8. Example of a mass window applied to the preliminary signal region events of 500 GeV, 10 ns staus. The mass window is highlighted in pink.

For the Discovery SR, since signal yields are lower than in the Exclusion SR as a result of higher  $dE/dx$  cuts, only two mass windows are used. One targets high-mass signal and the other targets low-mass signal, with a mass of 350 GeV as the boundary

between low and high mass. This is done to keep the analysis simple and to ease reinterpretation of the results. The parameters are displayed in Table 4.4, and were chosen after optimizing for signal significance across all signal masses and lifetimes. An in-depth description of the optimization procedure is given in Section 4.5.

target mass [GeV]	cone angle [degrees]	lower edge mass [GeV]
Less than 350	45	160
Greater than 350	45	300

TABLE 4.4. The 2D mass window parameters derived using the trapezoidal method. The angle identifies the opening angle of the mass window’s cone, and lower edge mass identifies the mass point (mass, mass) at the center of the trapezoidal lower edge.

For the Exclusion SR, mass windows are created to target several different stau masses and lifetimes, the parameters of which are chosen by optimizing for the lowest CLs value. The opening angles and low-mass bounds can be found in Table 4.5.

The estimated background yield in each mass window from the toy model background generation is shown in Figures 4.9 and 4.10.

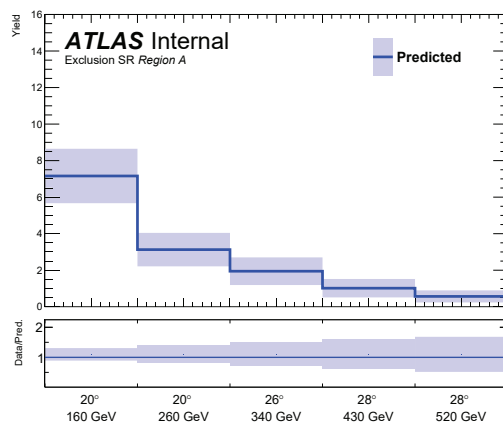


FIGURE 4.9. The estimated background yield in each mass window is shown. The error on the prediction includes the statistical and systematic uncertainty applied to the toy model. The error on the ratio is the fractional error

target mass [GeV]	target lifetime [ns]	cone angle [degrees]	lower edge mass [GeV]	expected signal yield
200	3	20	160	20.83
200	10	20	160	43.25
200	30	20	160	34.62
200	3000	20	160	9.21
300	3	20	260	9.86
300	10	20	260	23.28
300	30	20	260	22.10
300	3000	20	260	9.97
400	3	26	340	4.01
400	10	26	340	9.51
400	30	26	340	11.25
400	3000	26	340	5.72
500	3	28	430	2.21
500	10	28	430	5.44
500	30	28	430	5.67
500	3000	28	430	3.15
600	3	28	520	0.96
600	10	28	520	2.63
600	30	28	520	2.77
600	3000	28	520	1.56
700	3	28	600	0.44
700	10	28	600	1.35
700	30	28	600	1.44
700	3000	28	600	1.34

TABLE 4.5. The 2D mass window parameters derived using the trapezoidal method. The angle identifies the opening angle of the mass window’s cone, and lower edge mass identifies the mass point (mass,mass) at the center of the trapezoidal lower edge. The yields of slepton MC samples in the Exclusion SR are given after the mass windows are applied.

#### 4.5 DITRACK $dE/dx$ OPTIMIZATION

The ditrack analysis has two signal regions, the Discovery SR and Exclusion SR. They differ only in their ionization requirements and mass window parameters. The  $dE/dx$  values were chosen by studying the effect of different  $dE/dx$  requirements on the signal and background yields. The signal yields were taken from slepton Monte Carlo, while a fully data-driven, background toy model was used to form the estimated background yields. These background toy models simulate the kinematic behavior of ditrack events in the SRs, and are further describe in Section 5.3. The ionization cuts of the Discovery SR were chosen by studying how track  $dE/dx$  affected

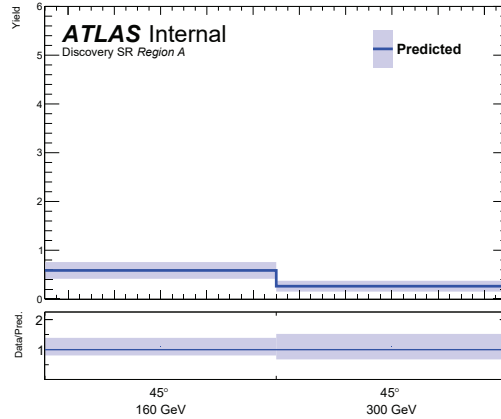


FIGURE 4.10. The estimated background yield in each mass window is shown. The error on the prediction includes the statistical and systematic uncertainty applied to the toy model. The error on the ratio is the fractional error.

signal significance.

$$Z = \sqrt{2(n \ln(\frac{n(b + \sigma^2)}{b^2 + n\sigma^2}) - \frac{b^2}{\sigma^2} \ln(1 + \frac{\sigma^2(n - b)}{b(b + \sigma^2)}))} \quad (4.2)$$

Uncertainties of 50% for background and 20% for signal were assumed during the optimization study.

For varying  $dE/dx$  values between 1.3 and 1.8  $\text{MeV g}^{-1}\text{cm}^2$ , the  $dE/dx$ -mass distributions of toy background models and simulated stau samples were generated. For each set of  $dE/dx$  cuts, and for each stau sample, a mass window was chosen for having the highest signal sensitivity, after varying the opening angles and low-edge boundaries. The signal sensitivities for all stau samples, across the different  $dE/dx$  cuts were plotted and considered to chose the most optimal ionization requirements of the Discovery SR. To illustrate, Figure 4.14 shows the signal and toy background yields across different  $dE/dx$  cuts for the 400 GeV staus with a lifetime of 30 ns. We find the signal significance is highest with higher  $dE/dx$  requirements, where

background rejection is strongest. This was found to be true for other stau samples, which differed in mass and lifetime, and can be referenced in Appendix A.

The ionization requirements for the ditrack Discovery SR are  $1.7 \text{ MeV g}^{-1}\text{cm}^2$  for both tracks.  $1.7 \text{ MeV g}^{-1}\text{cm}^2$  was chosen as a compromise between strong signal significance and acceptable statistics when validating the background estimates of the discovery region.

Finally, the Discovery SR will use two mass windows to simplify the analysis and ease reinterpretation. The low-mass window targets stau masses under 350 GeV and has a low-edge of 160 GeV. The high-mass window targets heavier staus, and has a low-edge of 300 GeV. Both mass windows have an opening angle of 45 degrees. These windows were chosen by optimizing for signal significance for all stau samples, and then choosing two windows which covered the majority of signal's phase space.

The optimization of  $dE/dx$  cuts for the Exclusion SR followed a similar method as the Discovery SR. The ionization cuts were chosen by optimizing for the lowest confidence limit. The CLs values were calculated such that the observed data matched that of the toy background model's yield, using the formula below. The mass window parameters for each stau sample were chosen by optimizing for the lowest CLs values. Smoothing was done to the angles and low-edge boundaries across each slepton signal mass, to negate the effect of statistical uncertainties. The mass window parameters are noted in Table 4.5.

$$CLs = \frac{ROOT.Math.poisson_cdf(b, s + b)}{1 - ROOT.Math.poisson_cdf_c(b - 1, b)} \quad (4.3)$$

Figure 4.15 shows the signal and toy background yields across different  $dE/dx$  cuts for the 500 GeV staus with a lifetime of 10 ns. The lowest CLs values occur when one track's  $dE/dx$  cut is 1.5-1.7  $\text{MeV g}^{-1}\text{cm}^2$  and the second track's  $dE/dx$  cut

is loosened to  $1.3 \text{ MeV g}^{-1}\text{cm}^2$ . This same range of  $dE/dx$  cuts resulted in minimal CLs values for other stau samples, which differed in mass and lifetime. These can be referenced in Appendix A.

The Exclusion SR's ionization requirements are at least one track has  $dE/dx > 1.6 \text{ MeV g}^{-1}\text{cm}^2$  and the second track has  $dE/dx > 1.3 \text{ MeV g}^{-1}\text{cm}^2$ .

Lastly, in developing the mass windows, circular mass windows were also considered and tested. The trapezoidal mass windows had better signal sensitivities for most slepton signals when compared to the toy background model. Also, a 200 GeV cut on the lower- $dE/dx$  track was tested as a possible substitute for the trapezoidal mass windows. However, the trapezoidal window had stronger signal sensitivities compared to the single-track cut. For example, the trapezoidal mass window applied to the 400 GeV slepton signal with a lifetime of 10 ns has a signal sensitivity of 3.27, while the single-track cut on the same signal had a sensitivity of 1.33.

#### 4.6 SUMMARY OF TWO-TRACK SIGNAL REGION

Table 4.6 summarizes the selection requirements for the two-track analysis, before application of the mass windows.

#### 4.7 TWO-TRACK ANALYSIS DATA AND SIGNAL CUTFLOW

The cutflow for the proposed two-track selection is illustrated in Table 4.7 for a representative stau signal. The cutflow table shows the numbers after the SUSY6 reconstruction is applied to data (the SUSY6 reconstruction setup is used as it includes the physics objects relevant to a  $dE/dx$  analysis). For the signal samples,

TABLE 4.6. Summary of two-track signal selection.

Data quality	GRL event cleaning jet cleaning	see Table 4.1. rejecting <code>EventInfo::Error</code> for LAr, Tile, SCT; <code>EventInfo::Core=18</code> vetoed rejecting pileup jets and <code>SuperLooseBadLLP</code> jets
Event topology	trigger $E_T^{\text{miss}}$ primary vertex	un-prescaled lowest $E_T^{\text{miss}}$ trigger; see Table 4.2. $E_T^{\text{miss}} > 20$ GeV the hard-scatter vertex to have at least two tracks
The event contains at least two tracks which pass <i>all</i> the track-level cuts below, except for the transverse mass requirement. Of the event's candidate tracks, at least <i>one</i> must satisfy the transverse mass requirement; tracks sorted in pT descending order.		
Track kinematics	momentum pseudorapidity transverse mass (1 track)	$p_T > 120$ GeV $ \eta  < 1.8$ $m_T(\text{track}, E_T^{\text{miss}}) > 130$ GeV
Track quality	impact parameters rel.momentum resolution hit requirement (1) hit requirement (2) hit requirement (3) hit requirement (4)	associated to PV $\delta(q/p)/(q/p) < \max\left(10\%, -1\% + 90\% \times \frac{ p }{\text{TeV}}\right)$ and $\delta(q/p)/(q/p) < 200\%$ $(n_{\text{used}} \geq 2)$ , or $\left[n_{\text{used}} = 1\right]$ and $(n_{\text{OF}}^{\text{IBL}} > 0)$ and $(n_{\text{hits}}^{\text{pix}} \geq 2 + n_{\text{used}})$ expect IBL hit and having at least an IBL hit, or expect B-Layer hit, not expect IBL hit and having at least a B-Layer hit no shared pixel hits and no split pixel hits $n_{\text{SCTHits}} > 5$
Veto	isolation (cone $\Delta R < 0.3$ ) electron veto hadron/tau veto	$\left(\sum_{\text{trk}} p_T\right) < 5$ GeV EM fraction $< 0.95$ $E_{\text{jet}}/p_{\text{track}} < 1$
pixel $dE/dx$		Exclusion SR: One track $\langle dE/dx \rangle_{\text{corr}} > 1.6$ MeV g <sup>-1</sup> cm <sup>2</sup> , second track $\langle dE/dx \rangle_{\text{corr}} > 1.3$ MeV g <sup>-1</sup> cm <sup>2</sup> Discovery SR: Both tracks $\langle dE/dx \rangle_{\text{corr}} > 1.7$ MeV g <sup>-1</sup> cm <sup>2</sup>
opposite charge		candidate track pairs have opposite electric charge
invariant mass		candidate track pair invariant mass $> 200$ GeV

the event yields have been normalized using the expected cross-sections and assuming the full Run-2 luminosity of  $140.1 \text{ fb}^{-1}$ .

<b>Selection</b>	<b>N(Events)</b>	<b>Eff.</b>	<b>Rel. Eff.</b>
Total	258.365	1.000	1.000
GRL	258.365	1.000	1.000
Event Cleaning	258.365	1.000	1.000
Jet Cleaning	255.914	0.991	0.991
Trigger	128.823	0.499	0.503
Primary Vertex	128.823	0.499	1.000
Offline $E_T^{\text{miss}}$	128.261	0.496	0.996
<b>Events are required to have at least two tracks which pass the following track-level requirements, except for <math>m_T</math> cut, where only a single track needs to pass.</b>			
Track in PV	105.326	0.408	0.821
$p_T > 50 \text{ GeV}$	92.471	0.358	0.878
$dE/dx$ Used Hits	84.044	0.325	0.909
IBL/B-Layer Hits	83.166	0.322	0.990
Shared/Split Hits	80.640	0.312	0.970
SCT Hits	72.858	0.282	0.903
Track Isolation	66.859	0.259	0.918
Track p uncertainty	64.274	0.249	0.961
Central track	53.108	0.206	0.826
$m_T > 130 \text{ GeV}$ (Event requires at least one track to have a large $m_T$ )	52.896	0.205	0.996
Electron veto	52.168	0.202	0.986
Hadron veto	51.044	0.198	0.978
$p_T > 120 \text{ GeV}$	50.812	0.197	0.995
Exclusion $dE/dx$ (1.6, 1.3)	12.662	0.049	0.249
Discovery $dE/dx$ (1.7, 1.7)	5.158	0.020	0.102
<b>At least a pair of candidate tracks should satisfy the following requirements</b>			
Exclusion Opposite Charge	12.637	0.049	0.998
Exclusion Invariant Mass $> 200 \text{ GeV}$	12.637	0.049	1.00
Discovery Opposite Charge	5.158	0.020	1.000
Discovery Invariant Mass $> 200 \text{ GeV}$	5.158	0.020	1.000
<b>Exclusion Signal Region</b>		<b>N(Events)</b>	<b>Fraction</b>
Exclusion SR Yield		12.637	0.049
<b>Discovery Signal Region</b>		<b>N(Events)</b>	<b>Fraction</b>
Discovery SR Yield		5.158	0.020
			1.000

TABLE 4.7. Cutflow of the two-track signal region for sleptons with mass 400 GeV and lifetime 10 ns (no mass window applied).

The same proposed two-track selection is applied to the full Run2 dataset, with the ionization and momentum requirements blinded, as seen in Table 4.8. The cutflow table shows the numbers after the SUSY6 selection is applied.

Selection	N(Events)	Eff.	Rel. Eff.
mini-xAOD	50310121	1.000	1.000
GRL	50310121	1.000	1.000
Event Cleaning	50265190	0.999	0.999
Jet Cleaning	49666647	0.987	0.988
Trigger	49666647	0.987	1.000
Primary Vertex	49666647	0.987	1.000
Offline $E_T^{\text{miss}}$	45683060	0.908	0.920
<b>Events are required to have at least two tracks which pass the following track-level requirements, except for <math>m_T</math> cut, where only a single track needs to pass.</b>			
Track in PV	38447575	0.764	0.842
$p_T > 50$ GeV	8582680	0.171	0.223
dE/dx Used Hits	6954302	0.138	0.810
IBL/B-Layer Hits	6682091	0.133	0.961
Shared/Split Hits	5128902	0.102	0.768
SCT Hits	4584036	0.091	0.894
Track Isolation	567083	0.011	0.124
Track p uncertainty	563801	0.011	0.994
Central track	410512	0.008	0.728
$m_T > 130$ GeV (Event requires at least one track to have a large $m_T$ )	156878	0.003	0.382
Electron veto	97119	0.002	0.619
Hadron veto	73304	0.001	0.755
$p_T > 120$ GeV	—	—	—
Exclusion dE/dx (1.6, 1.3)	—	—	—
Discovery dE/dx (1.7, 1.7)	—	—	—
<b>At least a pair of candidate tracks should satisfy the following requirements</b>			
Exclusion Opposite Charge	—	—	—
Exclusion Invariant Mass > 200 GeV	—	—	—
Discovery Opposite Charge	—	—	—
Discovery Invariant Mass > 200 GeV	—	—	—
<b>Exclusion Signal Region</b>	<b>N(Events)</b>	<b>Fraction</b>	
<b>Discovery Signal Region</b>	<b>N(Events)</b>	<b>Fraction</b>	
SR-two-track	0.xxx	0.yyy	

TABLE 4.8. Cutflow of the two-track signal region for the full Run2 dataset, blinded after nohadron cut (no mass window applied). An early cut of  $p_T \geq 50$  GeV is applied to reduce computing needs

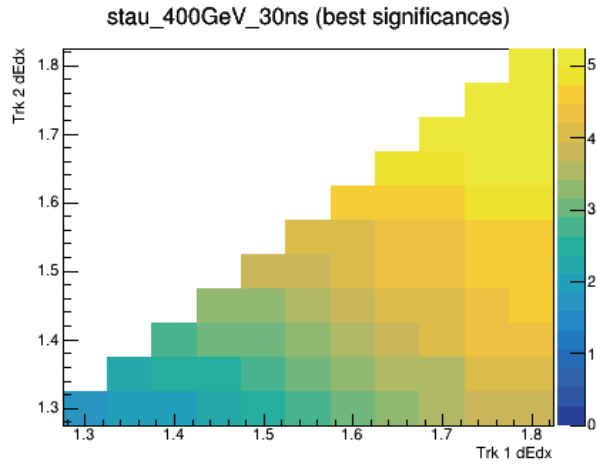


FIGURE 4.11. Highest achieved signal significances of varying track-level  $dE/dx$  cuts.

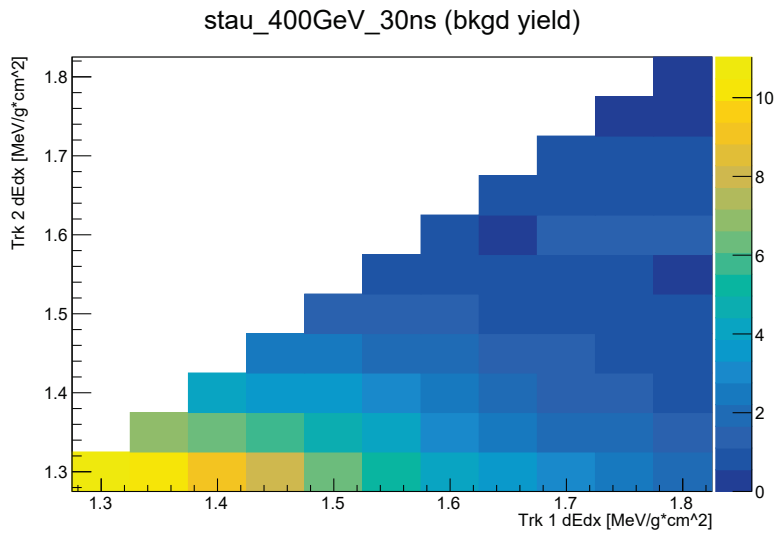


FIGURE 4.12. The toy background yields of the highest achieved signal significances.

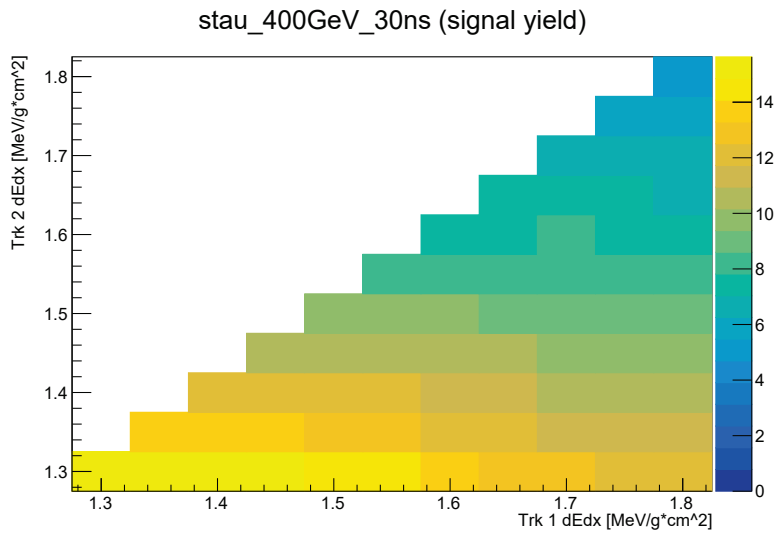


FIGURE 4.13. The signal yields of the highest achieved signal significances.

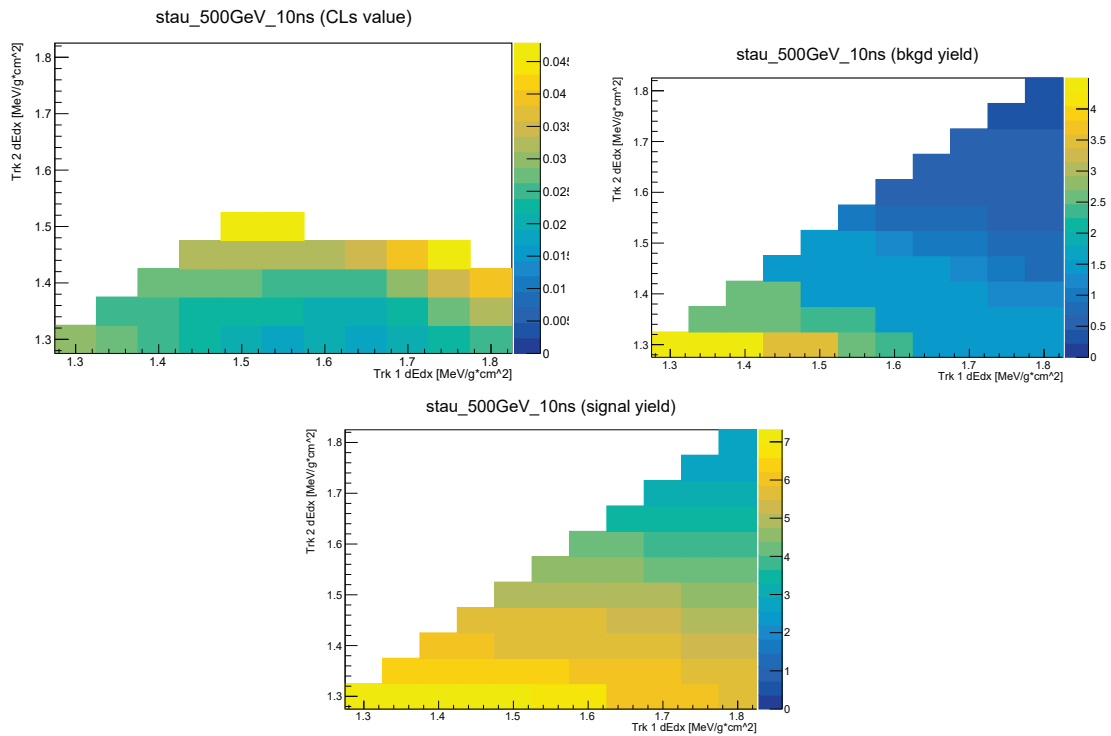


FIGURE 4.15. Optimization study of 500 GeV, 10 ns staus for the Exclusion SR. Plots show the a) lowest CLs values, and the corresponding b) toy background yields, and c) signal yields for varying track-level  $dE/dx$  cuts. Note: CLs values are plotted only if they are less than 0.05, and mass window parameters vary for each bin, to optimize for lowest CLs values.

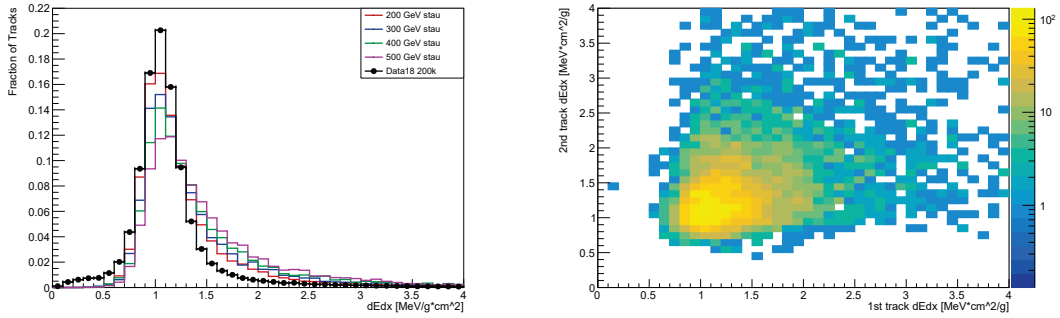


FIGURE 4.16. The track  $dE/dx$  distributions of both slepton tracks, for sleptons samples with lifetimes of 10ns, and masses of 200, 300, 400, 500 GeV. Using the 400 GeV, 10 ns stau sample, the correlation of  $dE/dx$  of pair-produced stau tracks. All event-level requirements including the trigger,  $E_T^{\text{miss}}$ , and event/jet cleaning requirements are applied. The track is required, for the signal samples, to be matched to a sparticle. Data is from 200k events in 2018.

## CHAPTER V

### BACKGROUND ESTIMATE

An overview of sources of Standard Model background in the search for long-lived staus is covered in Section 5.1. This chapter mainly describes the development and validation of the ditrack background estimate. Two different data-driven methods are used in this, an ABCD method (Section 5.2) and a toy model (Section 5.3) which was developed by Abraham Kahn of the University of Pennsylvania. The background toy model is used to give the estimated background yields in the analysis's signal regions, while the ABCD methods validated the toy's estimates. Multiple validation regions were used to test the background toy model and are described in Sections 5.2.1, 5.2.2, 5.2.3. Additional checks were done for validating the background estimates of the discovery signal regions, and these are described in Section 5.4.

#### 5.1 DITRACK BACKGROUND

The background of the two-track signal is mainly due to instrumental effects, including overlapping particles, the Landau tail of Standard Model MIPs, and effects from both in and out-of-time pileup. Since these background events are not easily simulated in Monte Carlo, we use two different methods to estimate the expected background in the signal region. One is a toy background model, a fully data-driven simulation of the background's expected  $dE/dx$ -mass distributions in the SRs. The other is a data-driven ABCD method, which estimates the total expected background in the SRs and is used to validate the toy background model. The ABCD method is also used to test assumptions in the background methods in several VR.

The ditrack background estimate is based upon the assumption that  $p_T$  and  $dE/dx$  are not correlated quantities for particles with momentum above 1 GeV. To study this assumption, datasets of Z-mumu events are used, as Z-mumu events are found to be a large source of background events in a high- $p_T$ , inverted-invariant mass VR (discussed in Section 5.2.2). Tracks which match to a muon are required to pass the baseline track-level requirements outlined in Section 4.3.1, and have  $p_T > 20$  GeV. These tracks are binned by  $p_T$  so that the  $dE/dx$  distributions and mean  $dE/dx$  values can be compared across different track-level  $p_T$  populations. The different distributions of  $dE/dx$  matched within statistical uncertainty across a  $p_T$  range of 20-500 GeV in which the ditrack VRs and SRs fall. Similarly, the mean values of  $dE/dx$  across the  $p_T$  bins showed good agreement, as seen in Figure 5.1. Lastly, the  $dE/dx$  tail fractions are studied for correlation with track  $p_T$ . Tail fractions refer to the percentage of the track population with  $dE/dx$  greater than a particular  $dE/dx$  boundary. The tail fractions are calculated using the  $dE/dx$  boundaries of 1.3, 1.4, 1.5, 1.8 MeV g<sup>-1</sup>cm<sup>2</sup>. For a given  $dE/dx$  boundary, the tail fractions remain constant for varying  $p_T$ , with some statistical fluctuation occurring in the highest  $p_T$  bin which contains the lowest population of tracks, also as seen in Figure 5.1. Thus, the background estimation and validation methods can rely upon the non-correlation of  $p_T$  and  $dE/dx$  in background.

## 5.2 ABCD METHOD

For the two-track background estimate, ABCD regions are defined by different  $p_T$  and  $dE/dx$  bins, as these properties are uncorrelated in our SM background for  $p_T$  above 1 GeV. The signal region is denoted as Region A. Regions B and C respectively are the high- $p_T$  and high- $dE/dx$  control regions. The ABCD background

estimate is formed from the full Run2 dataset. All events are required to pass the early event-level requirements including the trigger,  $E_T^{\text{miss}}$ , and event/jet cleaning. Then each event must have at least two candidate tracks, at least one of which has high  $p_T$  and  $dE/dx$ . A candidate track is defined as one which has passed all the track-level requirements, excluding  $m_T > 130$  GeV,  $p_T > 120$  GeV, and the ionization cut. For the Exclusion VR, the ionization cuts of the first track and second tracks are 1.6 and 1.3  $\text{MeV g}^{-1}\text{cm}^2$ , respectively. For the Discovery VR, the ionization cuts are 1.7  $\text{MeV g}^{-1}\text{cm}^2$  for both candidate tracks. To select the first track, noted as 'Track 1', candidate tracks which pass the  $p_T$  and  $dE/dx$  requirements are sorted by  $dE/dx$ , and the highest  $dE/dx$  track is chosen as Track 1, and is removed from the list of remaining candidate tracks. If Track 1 does not satisfy the transverse mass requirement, then Track 2 is chosen from only candidate tracks which do have a transverse mass larger than 130 GeV. To select the best second track from the remaining candidates, the candidate tracks are sorted into a track-level ABCD region. Region A has high- $p_T$ , high- $dE/dx$  tracks, region B has high- $p_T$ , low- $dE/dx$  tracks, region C has low- $p_T$ , high- $dE/dx$  tracks, and region D has low- $p_T$ , low- $dE/dx$  tracks. Within each individual region, the tracks are sorted by  $p_T$ , and overall the candidate tracks are sorted by their region, prioritizing in order of region A tracks, then B, then C, and lastly D. The first candidate track from this ranked list is selected to be the event's Track 2. Track 1 and Track 2 should have opposite electric charges and a calculated invariant mass larger than 200 GeV to be counted in the background estimate, or else the event is not used. The selected event is sorted into the appropriate region by the  $p_T$  and  $dE/dx$  properties of its Track 2, as shown in Figure 5.2. A simple overview of the multiple Validation Regions is given in Table 5.1, while full region definitions are available in Table 5.2. Lastly, the

Exclusion and Discovery control region and expected signal region yields are noted in Table 5.3.

TABLE 5.1. Validation Region Descriptions

<b>VR Name</b>	<b>How VR differs from SR</b>
Low- $p_T$ VR	70 < track $p_T$ < 100 GeV No invariant mass requirement
W-enhanced low- $p_T$ VR	70 < track $p_T$ < 100 GeV No transverse mass requirement Invariant Mass < 200 GeV
High- $\eta$ VR	track $p > 400$ GeV 1.8 < track $\eta$ < 2.5 No invariant mass requirement
Inverted Invariant Mass VR	Invariant Mass < 200 GeV
Z-mumu VR	No Offline MET cut No Transverse Mass cut Tracks must be matched to a muon 80 GeV < Invariant Mass < 100 GeV

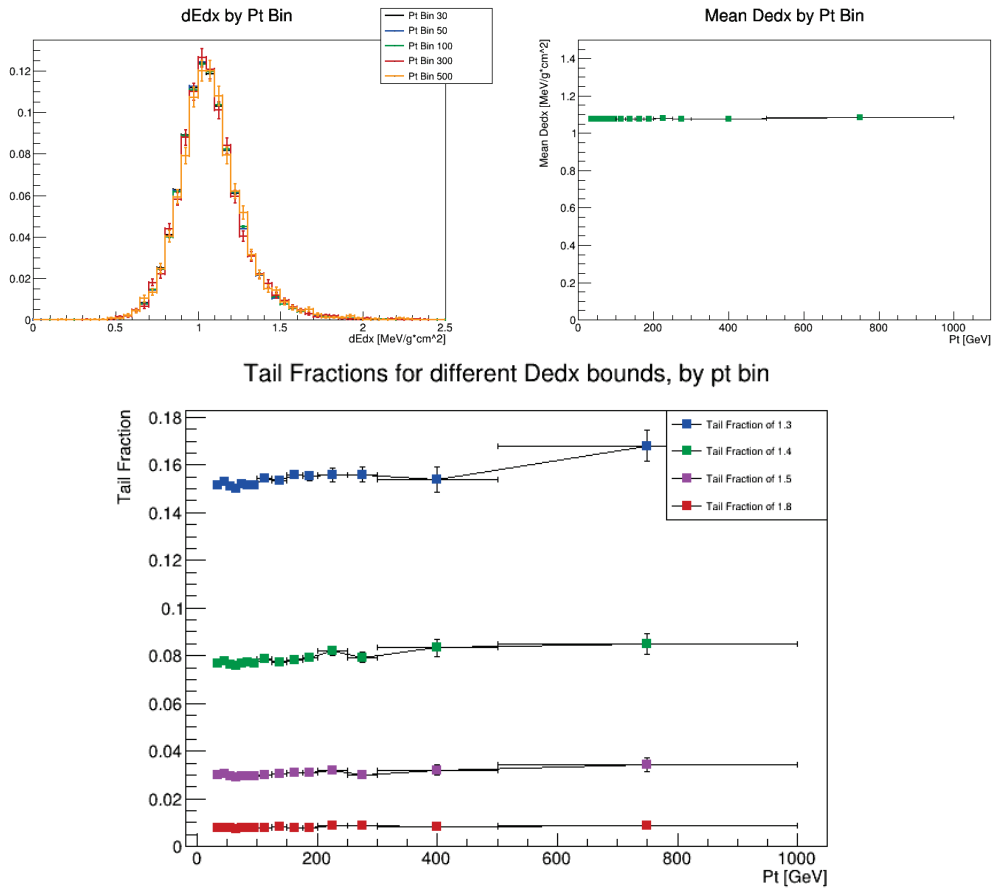


FIGURE 5.1. Z-mumu tracks were binned by  $p_T$ , and the plots show a) the  $dE/dx$  distributions, b) the mean  $dE/dx$  values of several bins, and c) the  $dE/dx$  tail fractions for different  $dE/dx$  boundaries. The bins used are the 30, 50, 100, 300, and 500 GeV bins, and their respective  $dE/dx$  distributions and mean values show good agreement within statistical uncertainty. Likewise, the tail fractions remain consistent across  $p_T$ , with some statistical fluctuation occurring in the 700-1000 GeV bin, which has the lowest population of tracks.

TABLE 5.2. Kinematic definitions of the two-track signal, control and validation regions for the Exclusion SR. Events must pass all event-level requirements and have at least two candidate tracks. Candidate tracks must pass all other selection requirements, and are ranked by  $p_T$  or  $p$ , and by  $dE/dx$ , using the boundaries defined below. The best-ranked track is noted 'Track 1' and has high  $p_T$  or  $p$ , and high  $dE/dx$ , as defined by the parameters below. The second best-ranked track is noted as 'Track 2'. These tracks must have opposite electric charge and calculated invariant mass above 200 GeV.

<b>Region</b>	Track 1		Track 2		Both Tracks
<b>SR and CRs</b>	$p_T$ [GeV]	$dE/dx$ [MeV g <sup>-1</sup> cm <sup>2</sup> ]	$p_T$ [GeV]	$dE/dx$ [MeV g <sup>-1</sup> cm <sup>2</sup> ]	$ \eta $
SR			> 120	> 1.3	
CR-B	> 120	> 1.6	> 120	< 1.3	< 1.8
CR-C			[50, 120]	> 1.3	
CR-D			[50, 120]	< 1.3	
<b>VR-low<math>p_T</math></b> <b>VR-W-enhanced low <math>p_T</math></b>	$p_T$ [GeV]	$dE/dx$ [MeV g <sup>-1</sup> cm <sup>2</sup> ]	$p_T$ [GeV]	$dE/dx$ [MeV g <sup>-1</sup> cm <sup>2</sup> ]	
VR-low $p_T$ -A			[70 – 100]	> 1.3	< 1.8
VR-low $p_T$ -B	[70 – 100]	> 1.6	[70 – 100]	< 1.3	
VR-low $p_T$ -C			[10 – 70]	> 1.3	
VR-low $p_T$ -D			[10 – 70]	< 1.3	
<b>VR-high<math>\eta</math></b>	$p$ [GeV]	$dE/dx$ [MeV g <sup>-1</sup> cm <sup>2</sup> ]	$p$ [GeV]	$dE/dx$ [MeV g <sup>-1</sup> cm <sup>2</sup> ]	$ \eta $
VR-high $\eta$ -A			> 400	> 1.3	[1.8 – 2.5]
VR-high $\eta$ -B	> 400	> 1.6	> 400	< 1.3	
VR-high $\eta$ -C			[50, 400]	> 1.3	
VR-high $\eta$ -D			[50, 400]	< 1.3	
<b>VR-invert <math>M_{invariant}</math></b> <b>VR-Z-mumu</b>	$p_T$ [GeV]	$dE/dx$ [MeV g <sup>-1</sup> cm <sup>2</sup> ]	$p_T$ [GeV]	$dE/dx$ [MeV g <sup>-1</sup> cm <sup>2</sup> ]	$ \eta $
VR-invert-A			> 120	> 1.3	< 1.8
VR-invert-B	> 120	> 1.6	> 120	< 1.3	
VR-invert-C			[50, 120]	> 1.3	
VR-invert-D			[50, 120]	< 1.3	

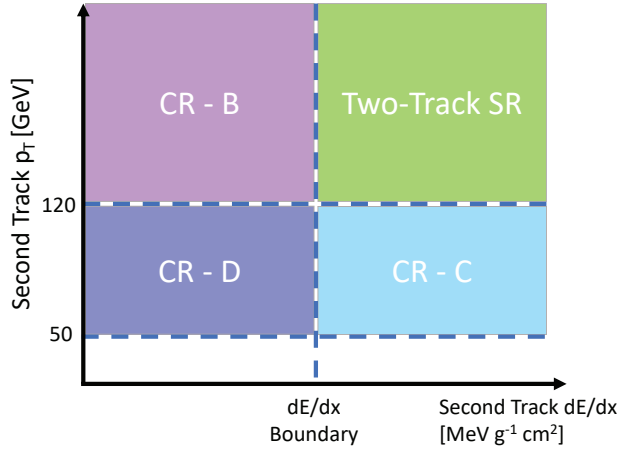


FIGURE 5.2. Schematic diagrams of the two-track Signal Region and the corresponding Control Regions. Events must pass all event-level requirements and have at least two candidate tracks, one which passes all track-level cuts, and the second track which has to pass all track-level cuts except for  $p_T > 120$  GeV and the ionization cut. The events are sorted into the corresponding ABCD regions by the characteristics of their second track, which is noted in the diagram as 'Second Track'.

TABLE 5.3. Event yields of ABCD regions in Run2 data, with Discovery and Exclusion SRs. The uncertainties are statistical

Region	Exclusion Background Yield	Discovery Background Yield
CR-B	157	113
CR-C	12	0
CR-D	168	111
Expected SR	$11.2 \pm 3.5$	$0 \pm 0$
SR	15	0

### 5.2.1 Low-Momentum VR

The low-momentum validation region was built to test the background estimation process in data. To ensure the validation region was orthogonal to the signal regions, meaning there's no overlap between signal and validation events, track  $p_T$  was limited to 10-100 GeV. Events in this validation region must pass all pre-track event-level

requirements (Trigger, offline MET, event/jet clean, GRL, PV) and must contain at least two candidate VR tracks. Candidate VR tracks have passed all the track-level requirements, except for the ionization and momentum cuts. The two candidate tracks of the event must also have opposite electric charges. Each event is required to have at least one ‘good’ track, with high  $dE/dx$  ( $> 1.6 \text{ MeV g}^{-1}\text{cm}^2$  for the Exclusion SR, and  $> 1.7 \text{ MeV g}^{-1}\text{cm}^2$  for the Discovery SR), and  $p_T > 70 \text{ GeV}$ . Then the secondary candidate tracks are filtered into ABCD regions, with momentum bins of 10-70 GeV and 70-100 GeV, and ionization energy bins of low and high  $dE/dx$  (for the Exclusion SR this  $dE/dx$  boundary is  $1.3 \text{ MeV g}^{-1}\text{cm}^2$ , and for the Discovery SR the boundary is  $1.7 dE/dx$  unit). If an event has more than two candidate tracks, the tracks are prioritized by being in the high  $p_T$  bin, then by being in the high  $dE/dx$  bin. Within the same bins, tracks are prioritized by  $p_T$ . The two best candidate tracks are used to sort the event into the ABCD regions of the low- $p_T$  VR, and any other tracks are not used. The number of events in regions B,C,D are used to validate the event yield in region A. An additional requirement is placed such that the two candidate tracks have opposite electrical charge and an invariant mass greater than 200 GeV. The definitions of these validation regions are shown in Table 5.2. The signal contamination from staus is negligible, and can be seen in Table 5.4.

Since the low-momentum VR has low statistics, a second, W-enhanced, low-momentum VR is added. This second VR is a looser version of the low-momentum VR, as it does not require any tracks to pass the transverse mass cuts, and invariant mass of the two-tracks must be lower than 200 GeV, inverting the SR requirement. The yields of the low-pt and the W-enhanced VRs can be found in Table 5.4, and between the expected and observed yields in the VR regions good agreement was found.

TABLE 5.4. Event yields of the low-momentum and W-enhanced VRs in Run2 data, for the Exclusion SR (with  $dE/dx$  bounds of 1.6 and 1.3 for the first and second tracks, respectively). The given uncertainties are statistical only. Signal contamination from 200 GeV staus of 10 ns lifetimes are given, no expected VR is given for staus.

<b>Region</b>	<b>Low-Pt VR</b>	<b>W-Enhanced VR</b>	<b>W-En. VR Staus</b>	<b>Low-Pt VR Staus</b>
CR-B	109	994	0.15	0.25
CR-C	50	539	0.6	0.6
CR-D	355	4384	0.3	0.3
Expected VR	$15.4 \pm 2.7$	$122.2 \pm 6.8$	—	—
VR	14	138	0.9	1.9

### 5.2.2 *Inverted Invariant-Mass VR*

An invariant mass VR is used to study the high-momentum background in the central eta region. The Inverted Invariant Mass VR is identical to the Exclusion SR, except that the invariant mass of the two candidate tracks must be less than 200 GeV, inverting the SR cut. The signal contamination from staus is negligible due to the high signal acceptance rate of the invariant mass requirement. To increase statistics, a second inverted-invariant mass VR is used. It specifically targets background from Z-mumu events by restricting the invariant mass to 80-100 GeV, and by removing the Offline  $E_T^{\text{miss}}$  and track-level transverse mass requirements. Additionally, the candidate tracks must be matched to a muon. Note that the Inverted Invariant Mass and Z-mumu VR are not mutually exclusive. In Table 5.5, the ABCD estimates of background in the validation regions agree well with data, within statistical uncertainty, for both the Inverted Invariant Mass VR and the expanded Z-mumu VR.

TABLE 5.5. Event yields of the invariant mass and Z-mumu VRs in Run2 data, for the Exclusion SR (with  $dE/dx$  bounds of 1.6 and 1.3 for the first and second tracks, respectively). The given uncertainties are statistical only.

<b>Region</b>	<b>Inverted Invariant Mass VR</b>	<b>Z-mumu VR</b>
CR-B	242	525
CR-C	97	937
CR-D	666	7338
Expected VR	$35.2 \pm 4.5$	$67.0 \pm 3.7$
VR	35	66

### 5.2.3 High-Eta Validation Region

The high- $\eta$  validation region tests the efficacy of the two-track ABCD method for high-mass background. This VR uses momentum instead of transverse momentum to define the boundaries of its regions, as transverse momentum by nature is depleted in the high- $\eta$  regions ( $1.8 < |\eta| < 2.5$ ). Events in this validation region must pass all pre-track event-level requirements (Trigger, offline MET, event/jet clean, GRL, PV) and must contain at least two candidate tracks in the high- $\eta$  region. Unlike for the background estimate and the low- $p_T$  validation region, none of the high- $\eta$  candidate tracks are required to pass the transverse mass cut. All candidate tracks must have  $p_T > 50$  GeV. The event's Track 1 and Track 2 are selected in a similar process to the one outlined in Section 5.2, using the  $dE/dx$  bound of  $1.4 \text{ MeV g}^{-1}\text{cm}^2$  and a momentum of 400 GeV. The two candidate tracks must have opposite electric charge and have a calculated invariant mass larger than 200 GeV. The event is sorted into the appropriate validation region by the  $dE/dx$  and momentum of the second selected track. The development of a high- $\eta$  VR is possible since the signal is depleted in the high- $\eta$  region. The definitions of these validation regions are shown in Table 5.2 and Figure 5.3. The signal contamination from staus is negligible, and can be seen in Table 5.6, along with the Run 2 dataset yield using the full VR selection.

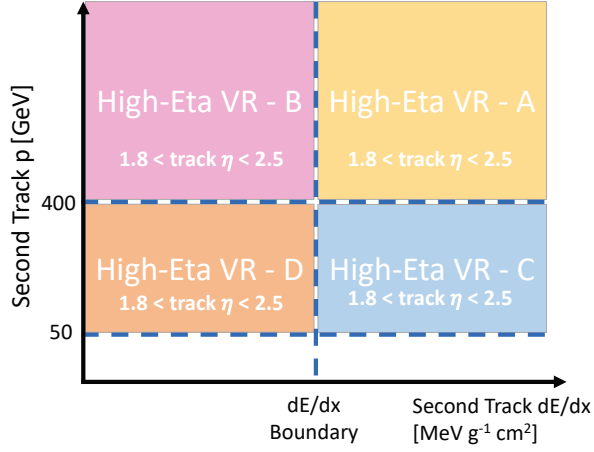


FIGURE 5.3. Schematic diagrams of the two-track high- $\eta$  Validation Regions. Events must pass all event-level requirements and have at least two candidate tracks which pass all track-level cuts but the  $\eta$ , ionization, transverse mass, and momentum requirements. Both tracks are required to have  $1.8 < |\eta| < 2.5$ . At least one track in the event has  $p_T > 120$  GeV and  $dE/dx > 1.4$  MeV g $^{-1}$ cm $^2$ , and the events are sorted into the corresponding ABCD regions by the characteristics of their second track. The given uncertainties are statistical only.

### 5.3 TOY MODEL

A data-driven toy model was developed to model the mass distribution of background in the Discovery and Exlcusion Signal Regions. It uses Run 2 data event which have passed the event-level selections and all the baseline track selections as mentioned in Section 4.3.1. From these preliminary ditrack events, two templates are built. The first is a  $dE/dx$  template, created from events with at least one low- $p_T$  track. Since  $p_T$  and  $dE/dx$  are uncorrelated in background, the  $dE/dx$  distribution from these events will be similar to the  $dE/dx$  distribution of the signal region events. The low- $p_T$  track requirement ensures no signal contamination occurs when studying the  $dE/dx$  distribution. Since a slight correlation exists between  $dE/dx$  and  $\eta$ , the  $dE/dx$  distributions are categorized by  $\eta$  bins of 0.2. The second template is

TABLE 5.6. Event yields of high- $\eta$  VR with estimated and actual background yields in high- $\eta$  VR region A. The signal contamination from 200 GeV, 10 ns staus is included, though the expected yields estimate is not included.

Region	Run2 Yield after NotHadron	High-eta VR 200 GeV Staus
VR-high $\eta$ -B	19	0
VR-high $\eta$ -C	2	0
VR-high $\eta$ -D	15	0
Expected VR-high $\eta$ A	$1.5 \pm 1.1$	–
VR-high $\eta$ -A	3	0

kinematic, created from events with events with two low- $dE/dx$  tracks. From these events, the track  $p_T$  and  $\eta$  information is used. Once the two templates are generated, a toy event is created by taking a pair of  $p_T$  and  $\eta$  values from the kinematic template and assigning a  $dE/dx$  value from the corresponding  $\eta$  bin of the other template. Then, the tracks  $dE/dx$ -derived masses are calculated. Each toy event is normalized to the Run 2 data by

$$N = \frac{\text{Number of events in the kinematic template}}{\text{Number of toy events}} \times \frac{1}{(1 - f_1)(1 - f_2)} \quad (5.1)$$

Where  $f_1$  and  $f_2$  are the fraction of tracks in the  $dE/dx$  template with low  $dE/dx$  in the  $\eta$ -bin corresponding to track 1 and track 2 respectively. Five million toy events were generated and used to form a  $dE/dx$ -mass distribution for the background estimate.

The ABCD validation regions were used to validate the background toy model, as shown in Table 5.7, and good closure was observed.

Lastly, an additional region was used with the ABCD validation regions, called Region X. This region requires both tracks to have high- $dE/dx$  and low- $p_T$ , which offers more statistics than the region A. The yields in data and the toy model matched well, as shown in Table 5.8.

TABLE 5.7. Comparison of event yields in Region A between data and the toy background model for various VR. The Estimated Yield is calculated from data using  $A = BC/D$  and the Toy Model Yield is the number of events from the Toy Model Background in Region A. The uncertainty in the Toy Model estimate shown is only the statistical uncertainty.

VR Name with 1.6, 1.3 dE/dx	Estimated Yield	Toy Model Yield	Actual Yield in Data
Low- $p_T$ VR	$15.4 \pm 2.7$	$13.0 \pm 2.6$	14
W-enhanced low- $p_T$ VR	$122.2 \pm 6.8$	$126 \pm 4.0$	138
High- $\eta$ VR	$1.5 \pm 1.1$	—	3
Inverted Invariant Mass VR	$35.2 \pm 4.5$	$36 \pm 1.9$	35
Z-mumu VR	$67.4 \pm 3.7$	$71 \pm 4.7$	66

TABLE 5.8. Comparison of event yields in Region X between data and the toy background model for various validation regions. The uncertainty in the Toy Model estimate shown is only the statistical uncertainty.

VR Name with 1.6, 1.3 dE/dx	Toy Model Yield	Actual Yield in Data
Region X Low- $p_T$ VR	$11.4 \pm 1.1$	14
Region X W-enhanced low- $p_T$ VR	$81 \pm 3.6$	81
Region X Inverted Invariant Mass VR	$80 \pm 3.5$	94
Region X Z-mumu VR	$822 \pm 18$	811

#### 5.4 DISCOVERY SR VALIDATION

Due to the high background rejection of the Discovery SR, additional studies were performed to validate the background estimates with dE/dx cuts of  $1.7 \text{ MeV g}^{-1}\text{cm}^2$ .

First, the Inverted Invariant Mass VR and the Z-mumu VR were tested on data using the ABCD method, with lowered, symmetric dE/dx cuts of 1.6, 1.5, 1.4, and 1.3  $\text{MeV g}^{-1}\text{cm}^2$ . These results, in Table 5.9, show with the increased statistics resulting from the increasingly lowered dE/dx cuts, the agreement between the expected and actual yield in data improved.

Secondly, a modified low-momentum VR was applied, where only one candidate track was required instead of two candidate tracks. The inclusion of single-track events greatly increased statistics, which served to test the closure of single-track

TABLE 5.9. Validation Region Definitions - Discovery (Lowered  $dE/dx$ )

VR Name	1.6 $dE/dx$ Yield (and Estimate)	1.5 $dE/dx$ Yield (and Estimate)	1.4 $dE/dx$ Yield (and Estimate)	1.3 $dE/dx$ Yield (and Estimate)
Inverted Invariant Mass VR	3 ( $4.0 \pm 1.2$ )	13 ( $10.4 \pm 2.1$ )	42 ( $30.9 \pm 3.6$ )	119 ( $111.2 \pm 7.4$ )
Z-mumu VR	7 ( $7.1 \pm 0.8$ )	24 ( $18.7 \pm 1.3$ )	59 ( $59.2 \pm 2.5$ )	199 ( $210.8 \pm 5.5$ )

events at the high  $dE/dx$  cut of  $1.7 \text{ MeV g}^{-1}\text{cm}^2$ . Table 5.10 shows the agreement between the expected and observed yields of region A. This test of the highest  $dE/dx$  cut, coupled with the ditrack test at various, lower  $dE/dx$  cuts, suggests that the ditrack Discovery VRs would also have good closure, if they possessed more statistics.

TABLE 5.10. Event yields of single-track ABCD regions of low-momentum VR in Run2 data, with  $dE/dx$  cut of  $1.7 \text{ MeV g}^{-1}\text{cm}^2$ .

Region	Discovery Background Yield
CR-B	95061
CR-C	1045
CR-D	82507
expected CR-A	$1204 \pm 38$
observed CR-A	1246

## CHAPTER VI

### DITRACK UNCERTAINTIES AND RESULTS

This chapter covers the statistical and systematic uncertainties of the final expected background and signal yields of the ditrack analysis. The final yields are given and discussed in Section 6.2, and no excess of signal was observed to indicate the existence of long-lived staus with lifetimes and masses sensitive to discovery at the ATLAS detector. Instead new exclusion limits for staus are presented. The impact of this analysis and future of long-lived Supersymmetry is discussed in Section 6.3.

#### 6.1 BACKGROUND UNCERTAINTIES

Both statistical and systematic uncertainties were calculated for the background estimate. The background estimate formed by the toy model has three sources of statistical uncertainty. The first is from forming the  $dE/dx$  template, and is assessed by applying a Gaussian fluctuation to each bin. The second is from sampling from the kinematic template. Applying a Poissonian weight to the selected track determines how often that track is selected for the toy model. Lastly, the procedure of building toy tracks is run one hundred times, creating a hundred different mass distributions. From these different versions, the RMS from each bin of the background mass distributions gives a statistical uncertainty.

A systematic uncertainty is needed to account for the non-closure between the mass distributions of the toy model and of data. The mass distributions of toy models and data are compared in the Inverted Invariant Mass VR, the W-enhanced low- $p_T$  VR, and the Z-mumu VR. The ratio of data to toy is fit to a line, and a 0.68 confidence interval band is applied to that fit. The systematic uncertainty is

taken from the width of the band, and can be seen in Figure 6.1. The systematic uncertainty is larger at higher masses, which is expected, as the mass resolution is lower at high mass, and the higher mass phase space had lower statistics across all validation regions. The statistical and systematic uncertainties of the mass windows are available in Table 6.1.

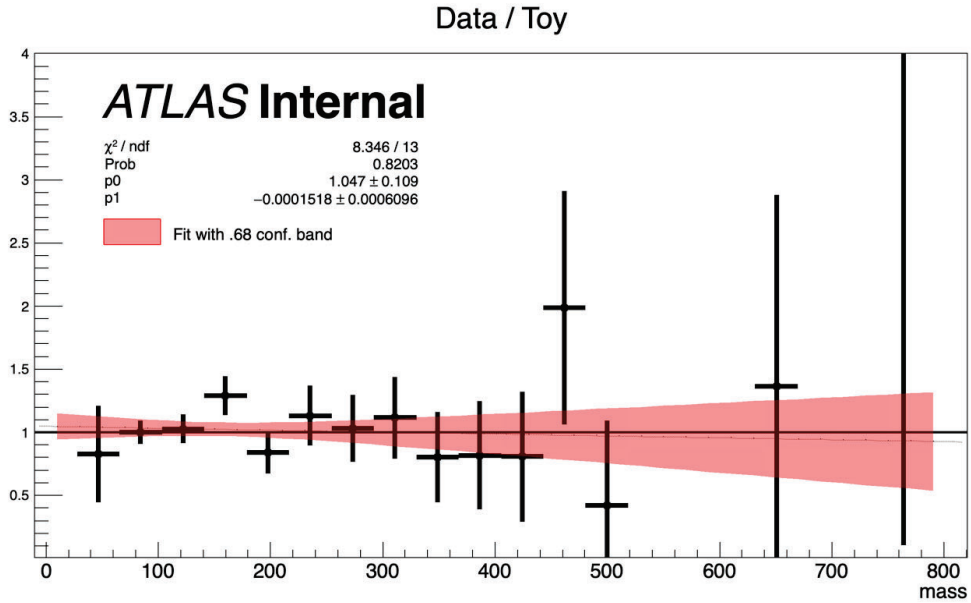


FIGURE 6.1. Ratio of data and toy mass distribution in three Vrs is fit to line, the 0.68 confidence interval band is used as a non-closure systematic uncertainty.

## 6.2 RESULTS

The expected background and observed data yields of the Exclusion Signal Region are noted in Table 6.1. The background estimate was formed from applying the mass window selection, as described in Section 4.4, to the data-driven toy background model, described in Section 5.3. In total, fifteen events were observed which passed the event and track-level selections of the Exclusion SR, but of those fifteen only four were accepted by the mass windows. The Discovery SR had a

zero background estimate, and no data events were observed which passed its strict  $dE/dx$  requirements. We find that the observed events do not exceed the expected background estimates.

TABLE 6.1. Exclusion SR data and background yields in different trapezoids defined for different mass windows, with the window’s lower mass bound noted.

Target Sig. Mass	Data Events	Expected BG	Lower Bound
Inclusive	15	19.33	0
Slepton Mass Windows			
200	4	$7.21 \pm 0.45$ (stat.) $\pm 1.39$ (syst.)	160
300	1	$3.15 \pm 0.21$ (stat.) $\pm 0.87$ (syst.)	260
400	1	$1.94 \pm 0.15$ (stat.) $\pm 0.72$ (syst.)	340
500	0	$1.01 \pm 0.09$ (stat.) $\pm 0.48$ (syst.)	430
600	0	$0.57 \pm 0.07$ (stat.) $\pm 0.31$ (syst.)	520
700	0	$0.57 \pm 0.07$ (stat.) $\pm 0.31$ (syst.)	520

The Exclusion SR  $dE/dx$ -mass distributions of all 15 observed events are shown in Figure 6.2, and are noted in red. They are compared to the estimated background distribution, before any mass windows are applied. As was predicted by the toy background model, the majority of the observed events (9 out of 15) are clustered around a symmetric lower-/dedx-mass range (about 100-300 GeV). Of these 9 events, only two passed the mass window selections targeting the 200 GeV staus, i.e, the lowest-mass signal model. Another four out of the fifteen events show poor agreement between their two tracks’  $dE/dx$ -masses, like the right-most observed event. There the first track has a measured  $dE/dx$ -mass of 900 GeV, while the second track’s  $dE/dx$ -mass was measured to be much lower, 300 GeV. This can arise from a low-mass track recording a  $dE/dx$  value that is higher than its mass would indicate. Such mis-reconstructions can occur due to the Landau distribution of  $\langle dE/dx \rangle$ , as explained in Section 3.5.1.

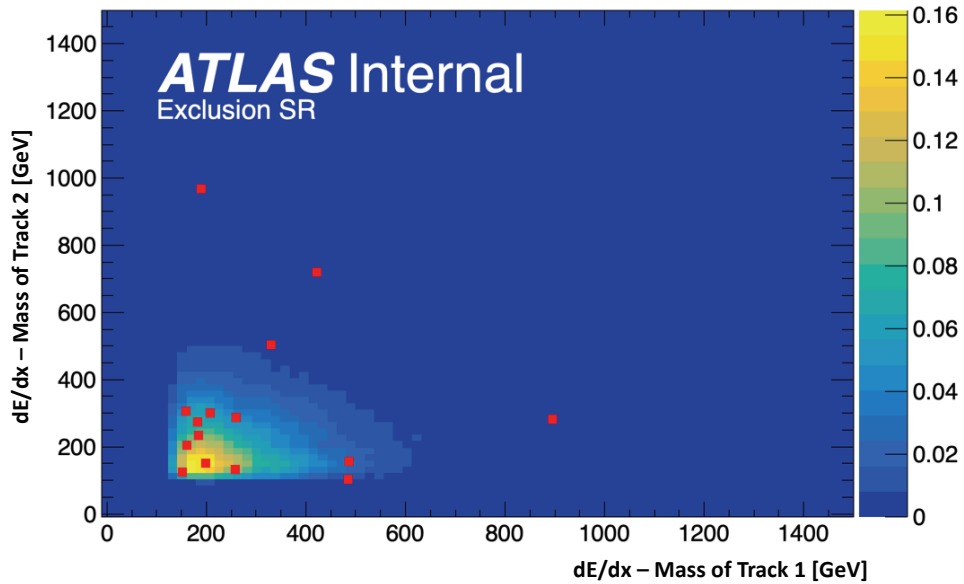
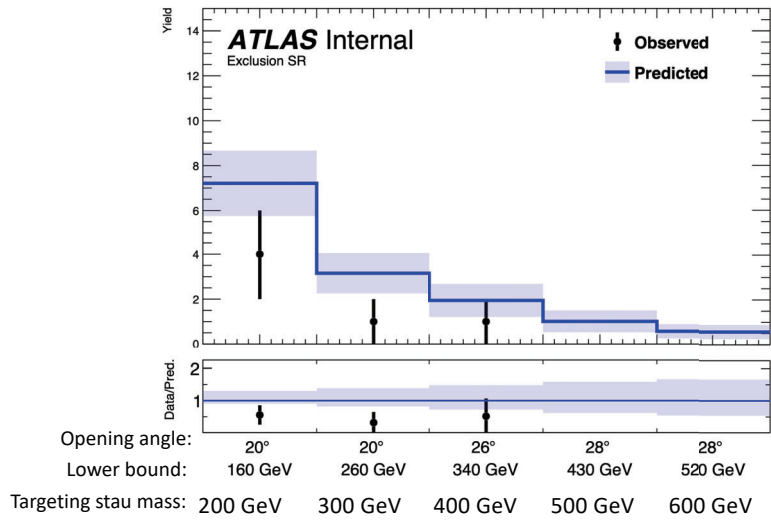


FIGURE 6.2. All observed data events marked by red squares, overlaid on the toy background model estimate of the  $dE/dx$ -mass distributions [Kahn, A].

The mass window selections were described in Section 4.4, and they serve to reject events with poor agreement between their two  $dE/dx$ -mass measurements, or lower  $dE/dx$ -masses than the targeted signal mass. The yields of each mass window are portrayed in Figure 6.3, where it is important to note that the mass windows are not orthogonal to one another, meaning there is one observed event which is accepted by three different windows.



1

FIGURE 6.3. Both tracks'  $dE/dx$ -derived masses from the observed data events overlaid on the background estimate of  $dE/dx$ -derived mass [Kahn, A.]

As an additional validation of the toy background model, the  $dE/dx$ -mass values of each track are compared to those of the fifteen observed events, see Figure 6.4. The uncertainties displayed are statistical, and since only fifteen events were observed, the data's uncertainties are large compared to those of the background estimate. A statistical Kolmogorov-Smirnov test was performed, and the ks value was 0.834. A ks value of 1 would indicate the data and estimated background were sampled from identical distributions. Since the observed yield suffers statistically due to the low event count, a ks value of 0.834 indicates good agreement between the background predication and data.

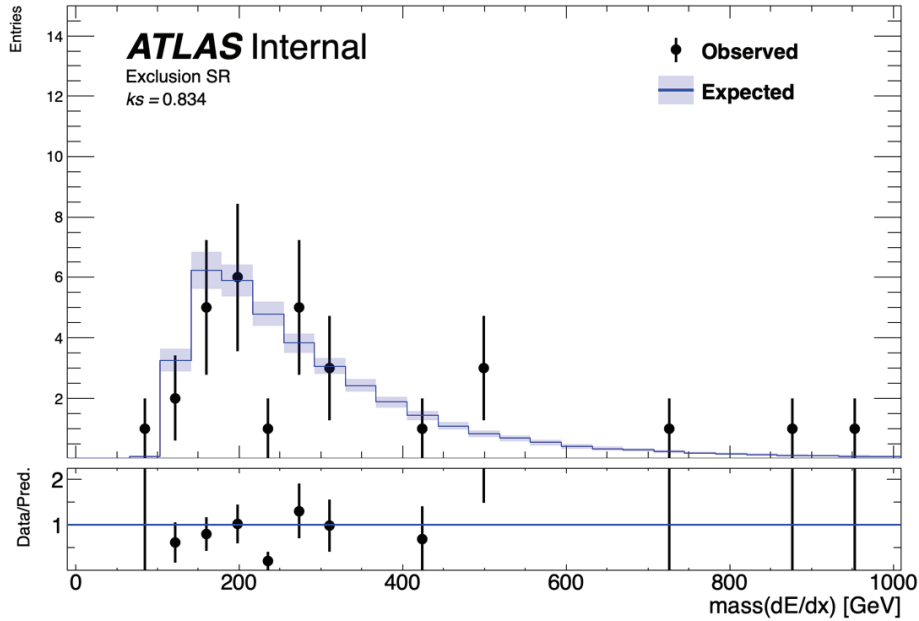


FIGURE 6.4. Both tracks'  $dE/dx$ -derived masses from the observed data events overlaid on the background estimate of  $dE/dx$ -derived mass. [Kahn, A.]

Since we do not observe an excess of events when compared to the background estimate, this ditrack search does not support the discovery of long-lived, heavy, charged particles in the ATLAS Run2 dataset. Instead, we can set new exclusion limits for the lifetimes and masses of pair-produced staus produced by a minimal supersymmetric model. The upper limits of 95% CL on the production cross-sections for staus with lifetimes of 3 ns, 10 ns, 30 ns, and stable staus as a function of mass are portrayed in Figures 6.5, 6.6, 6.7, and 6.8, respectively. These plots show the observed limit this analysis created in black, against the theoretical production cross-section bounds in grey. From these, we conclude that long-lived staus with lifetimes of 3 ns are excluded below masses of 420 GeV, those with 10 ns lifetimes are excluded below 615 GeV, and those with 30 ns lifetimes are excluded below 620 GeV. In the case of stable staus, masses below 523 GeV are excluded.

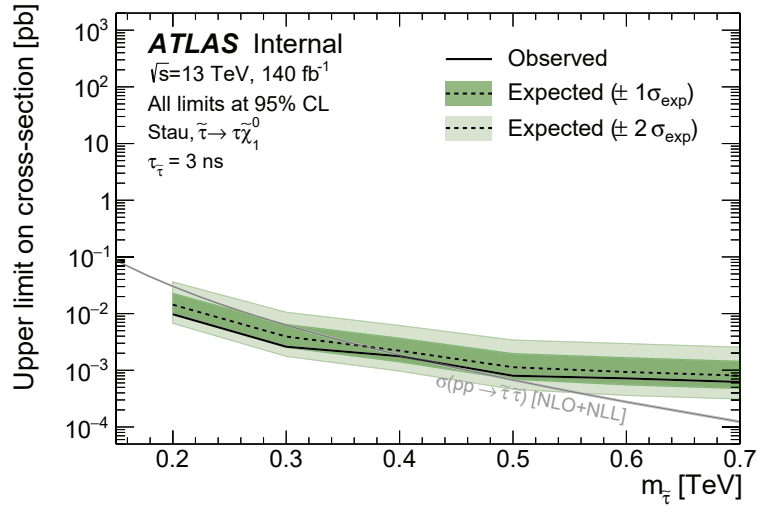


FIGURE 6.5. The expected and observed signal sensitivity of the ditrack analysis, for long-lived staus with 3ns lifetimes.

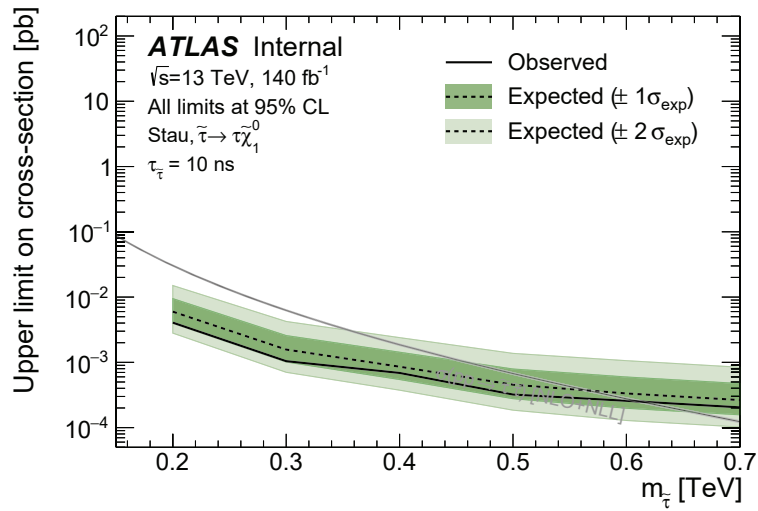


FIGURE 6.6. The expected and observed signal sensitivity of the ditrack analysis, for long-lived staus with 10ns lifetimes.

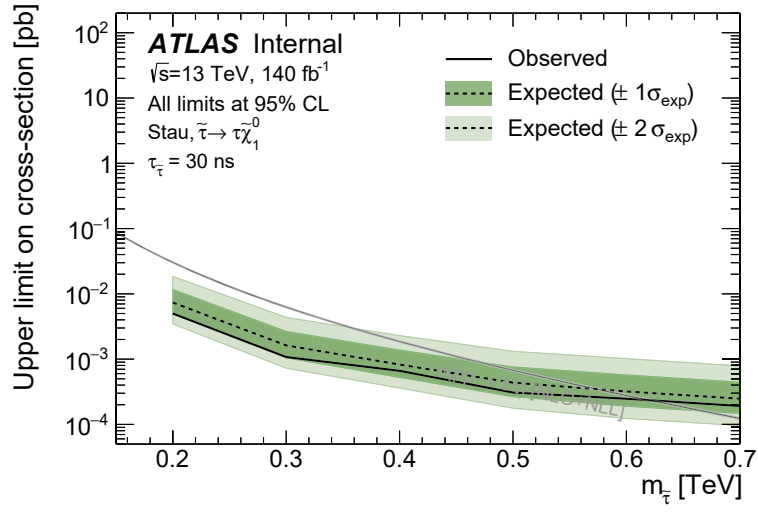


FIGURE 6.7. The expected and observed signal sensitivity of the ditrack analysis, for long-lived staus with 30ns lifetimes.

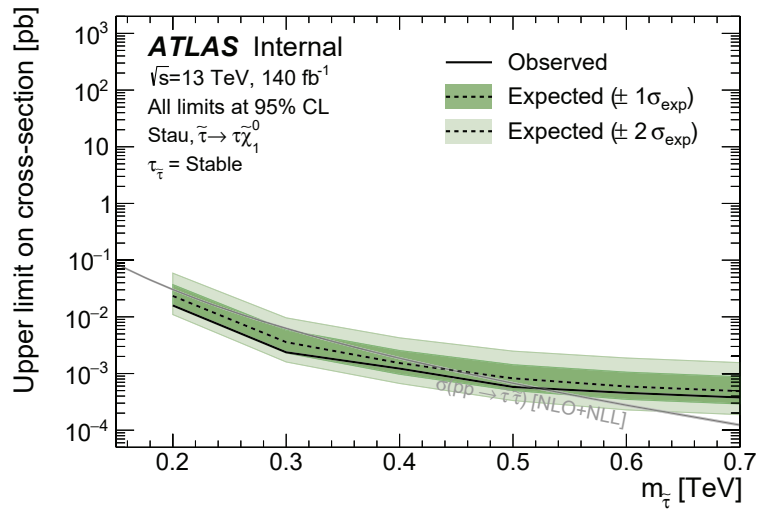


FIGURE 6.8. The expected and observed signal sensitivity of the ditrack analysis, for long-lived staus with 3000ns lifetimes.

### 6.3 OUTLOOK

The observed yields of the Exclusion SR noted in Section 6.2 are model-independent. Reinterpretation of the results can be performed for any physics model with sensitivity to the ditrack selections. The ditrack analysis was optimized for minimal supersymmetric stau models of pair-produced staus. The previous iteration of the analysis which searched for heavy, charged, long-lived particles with high ionization energy was sensitive to gluinos and charginos, which have higher production cross-sections than staus of similar lifetimes, but it did not have good sensitivity to staus. By developing a ditrack analysis, we were able to target long-lived staus and expand their current experimental limits.

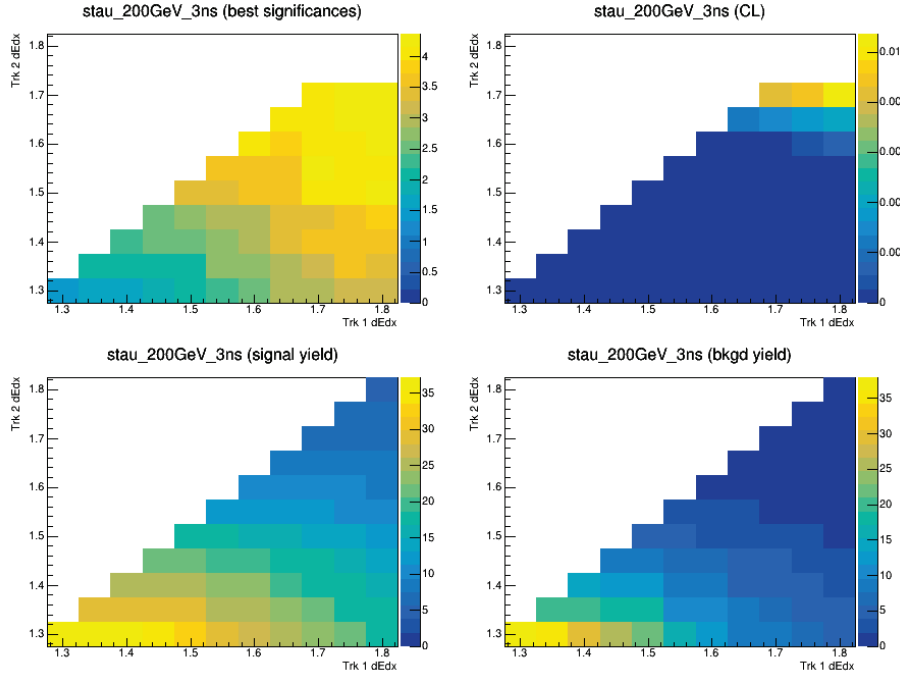
Supersymmetric particles were not discovered by this analysis, but future searches will probe further. One current search looks for disappearing tracks using the same pixel- $dE/dx$  measurement as a critical selection. It looks for staus and charginos with 0.1-10 ns lifetimes and is partially built on the work done by this ditrack analysis. Other SUSY searches are ongoing, and future detector and accelerator upgrades such as the High-Lumi LHC and its related ATLAS sensitivity upgrades will open the door to rarer, higher-mass SUSY searches.

## APPENDIX

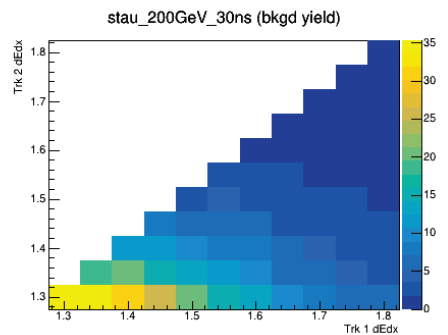
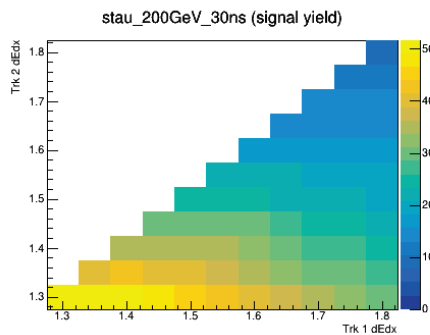
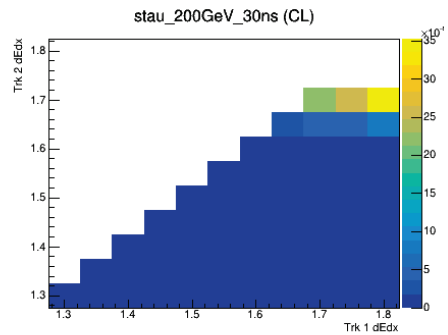
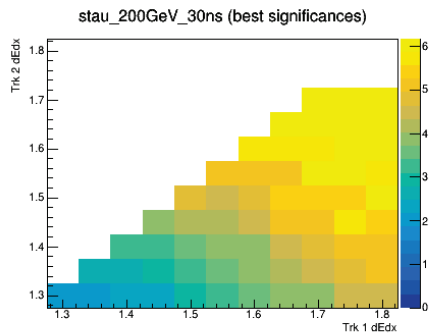
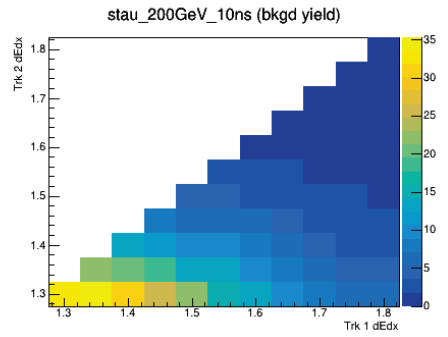
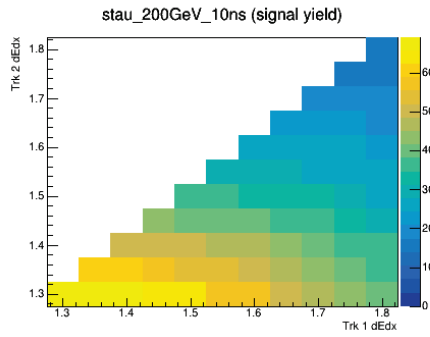
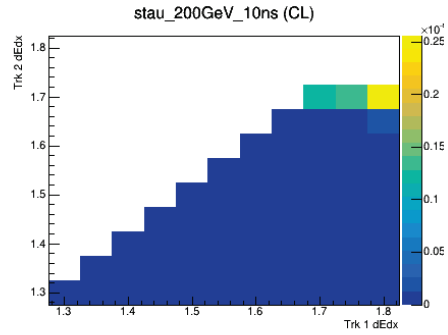
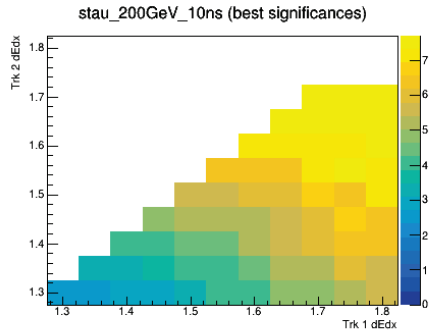
### DITRACK DE/DX OPTIMIZATION STUDY

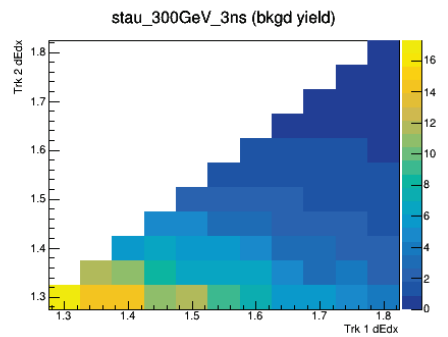
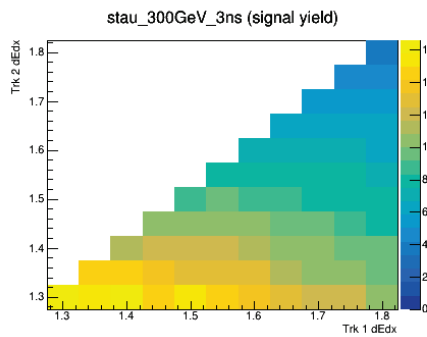
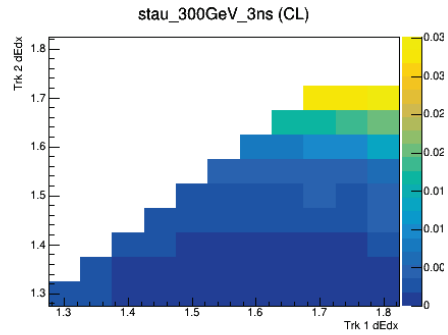
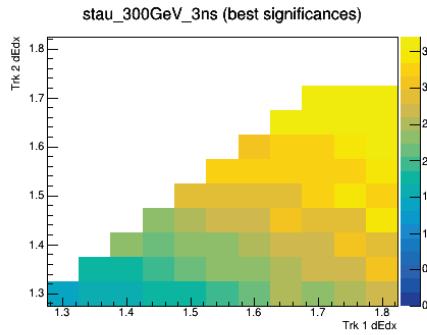
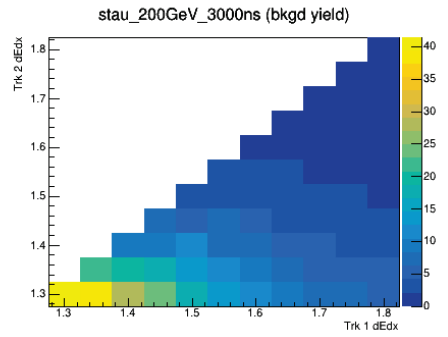
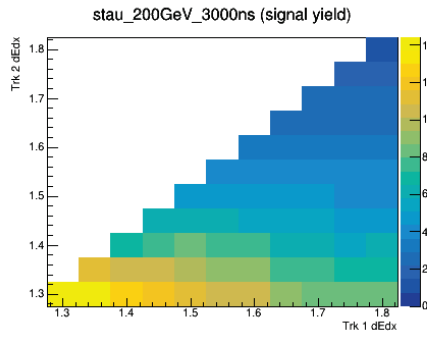
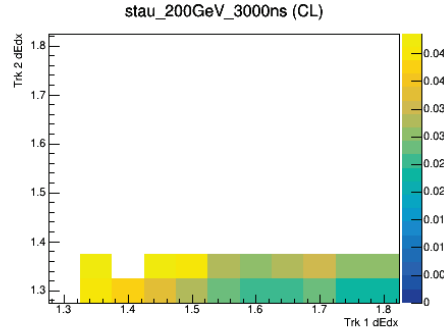
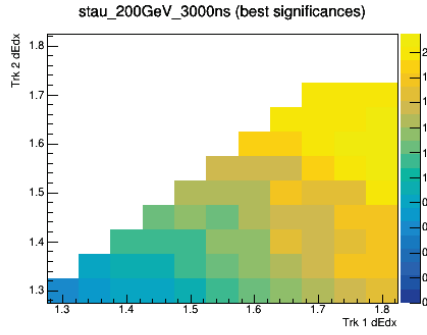
This appendix contains the plots from the  $dE/dx$  optimization study for the Exclusion and the Discovery signal regions. There are four plots per stau sample, containing the optimal CLs value, signal significance, signal yield, and background yield for a range of ditrack  $dE/dx$  cuts. A description of the optimization procedure is in Section ??.

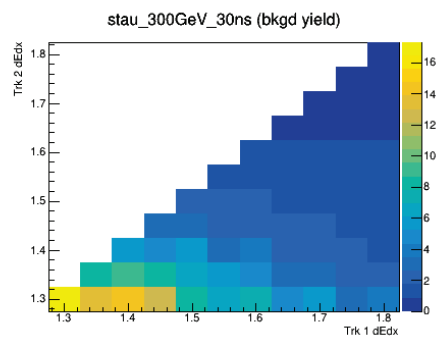
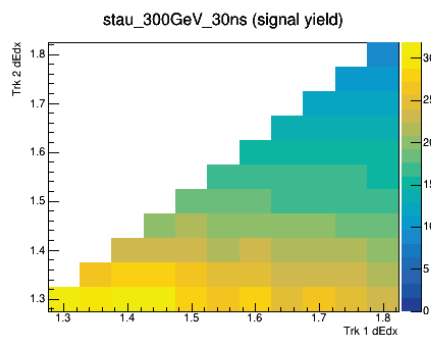
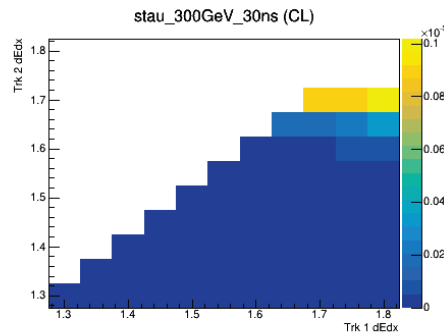
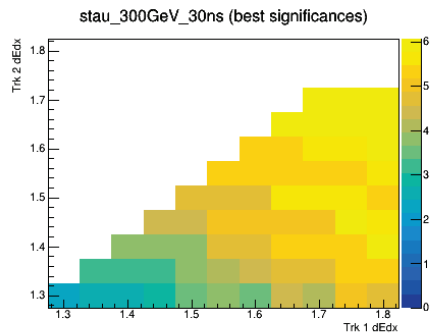
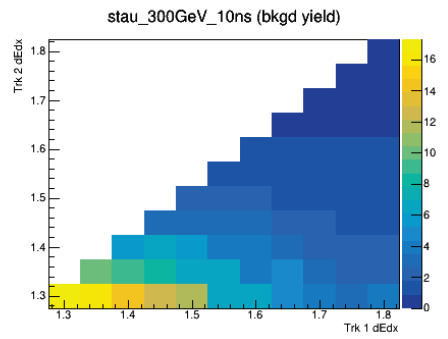
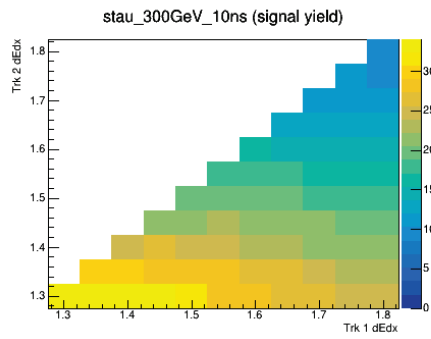
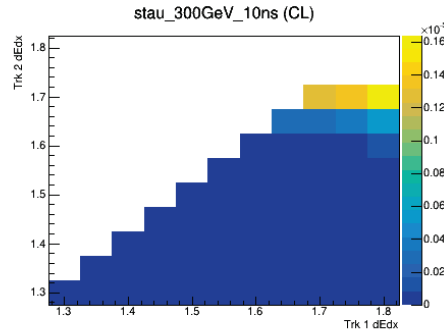
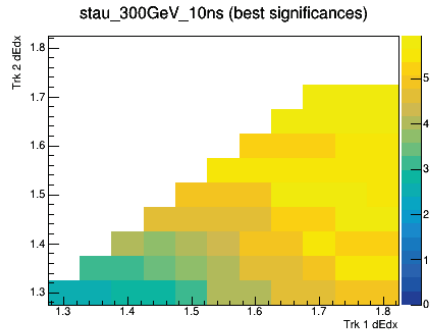
#### A.1 EXCLUSION SIGNAL REGION

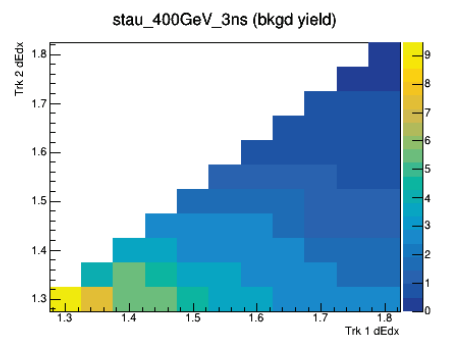
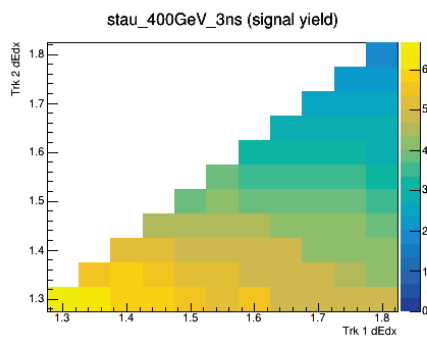
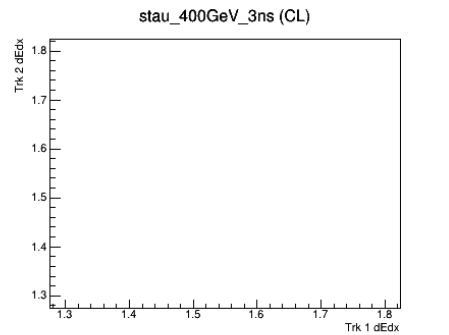
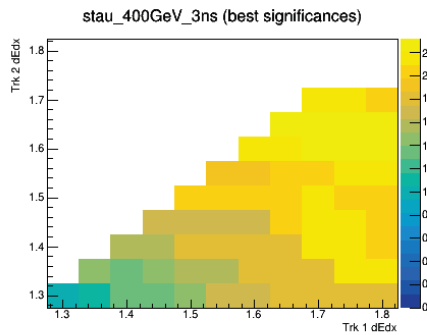
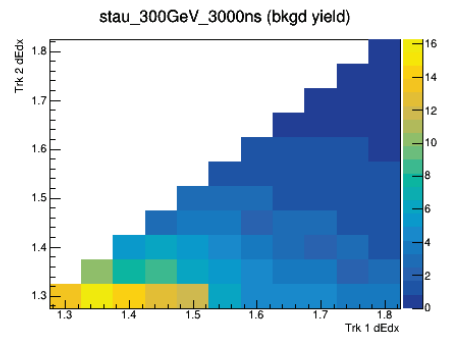
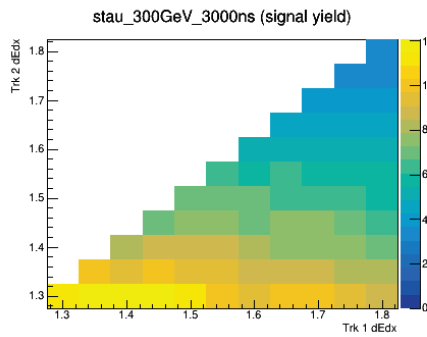
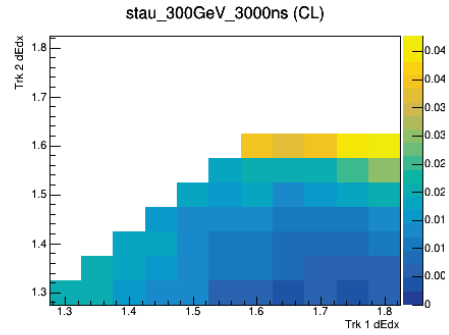
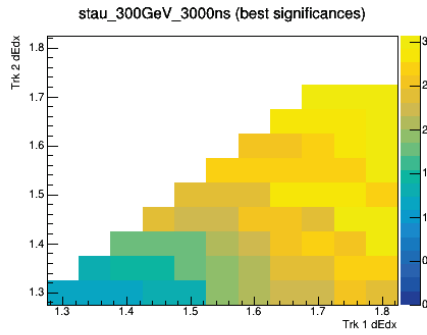


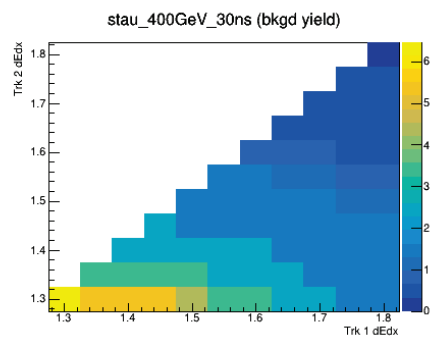
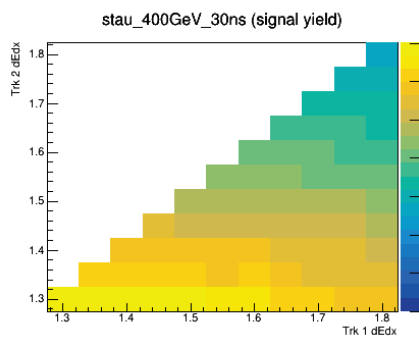
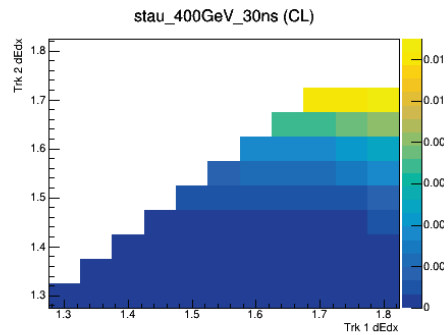
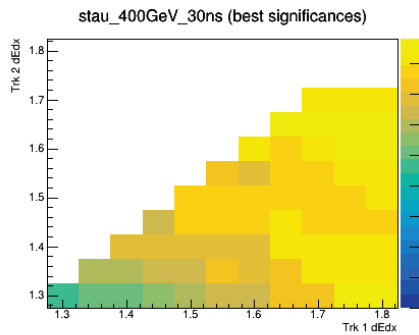
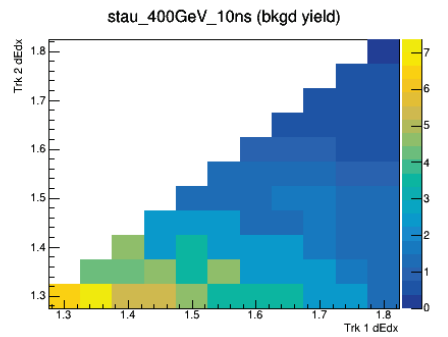
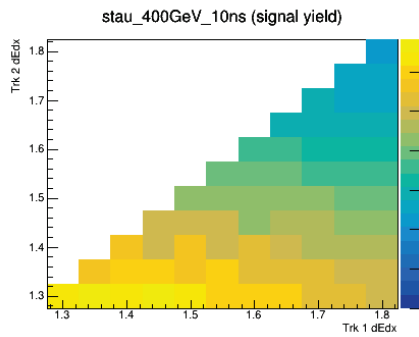
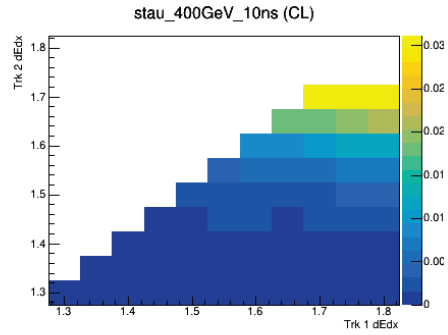
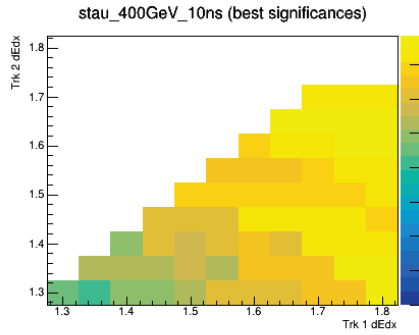
#### A.2 DISCOVERY SIGNAL REGION

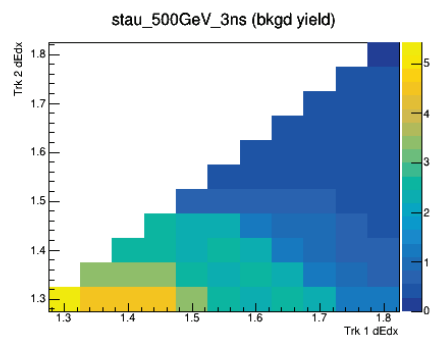
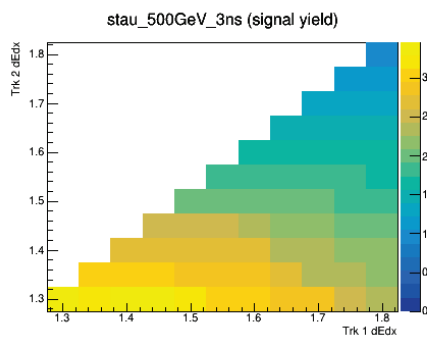
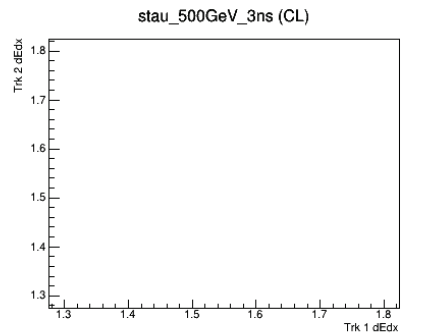
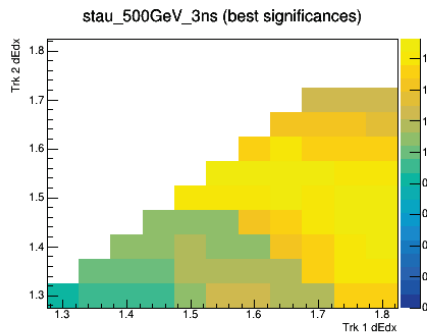
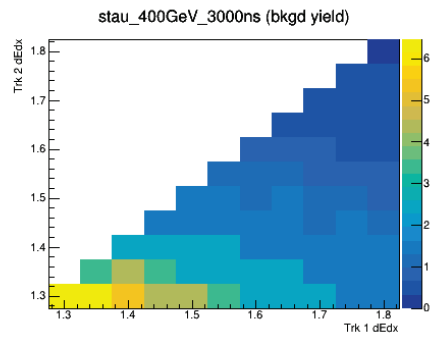
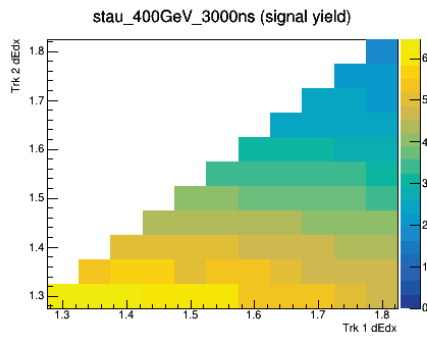
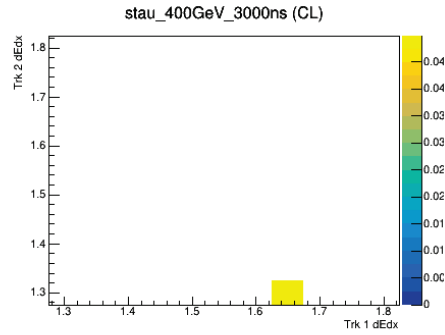
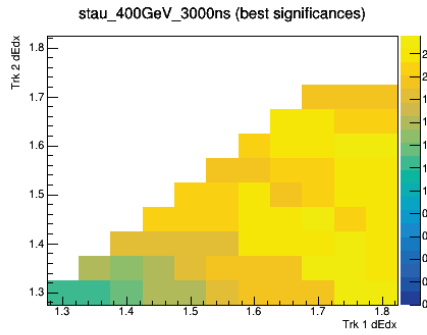


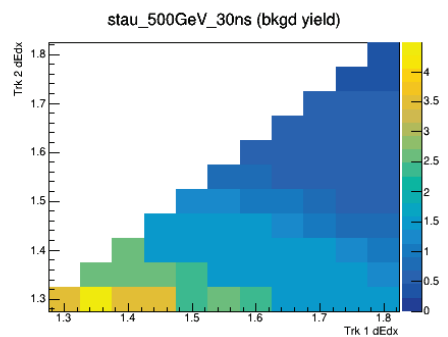
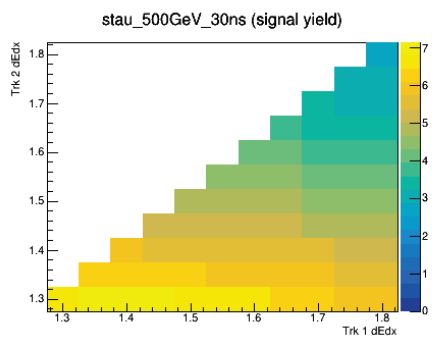
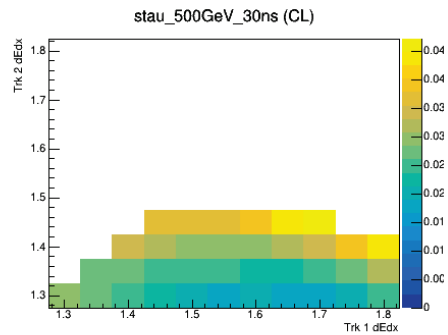
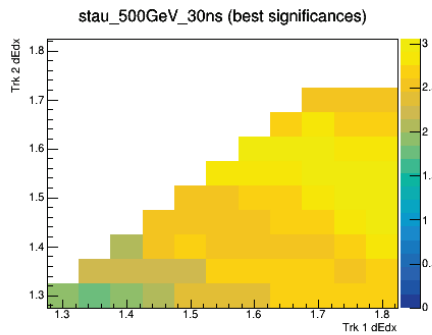
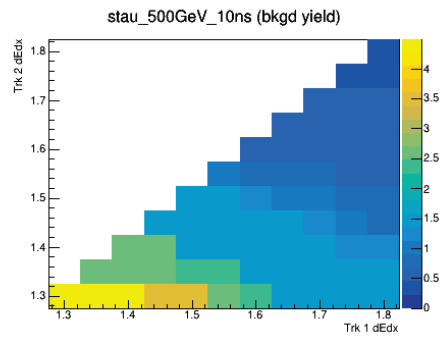
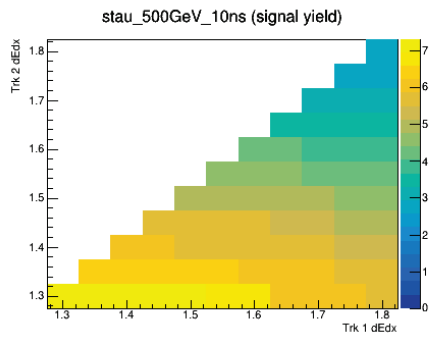
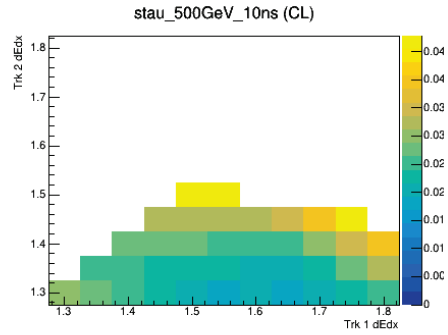
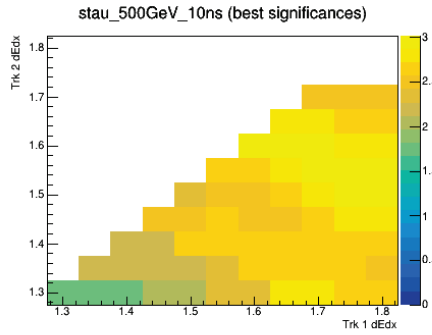


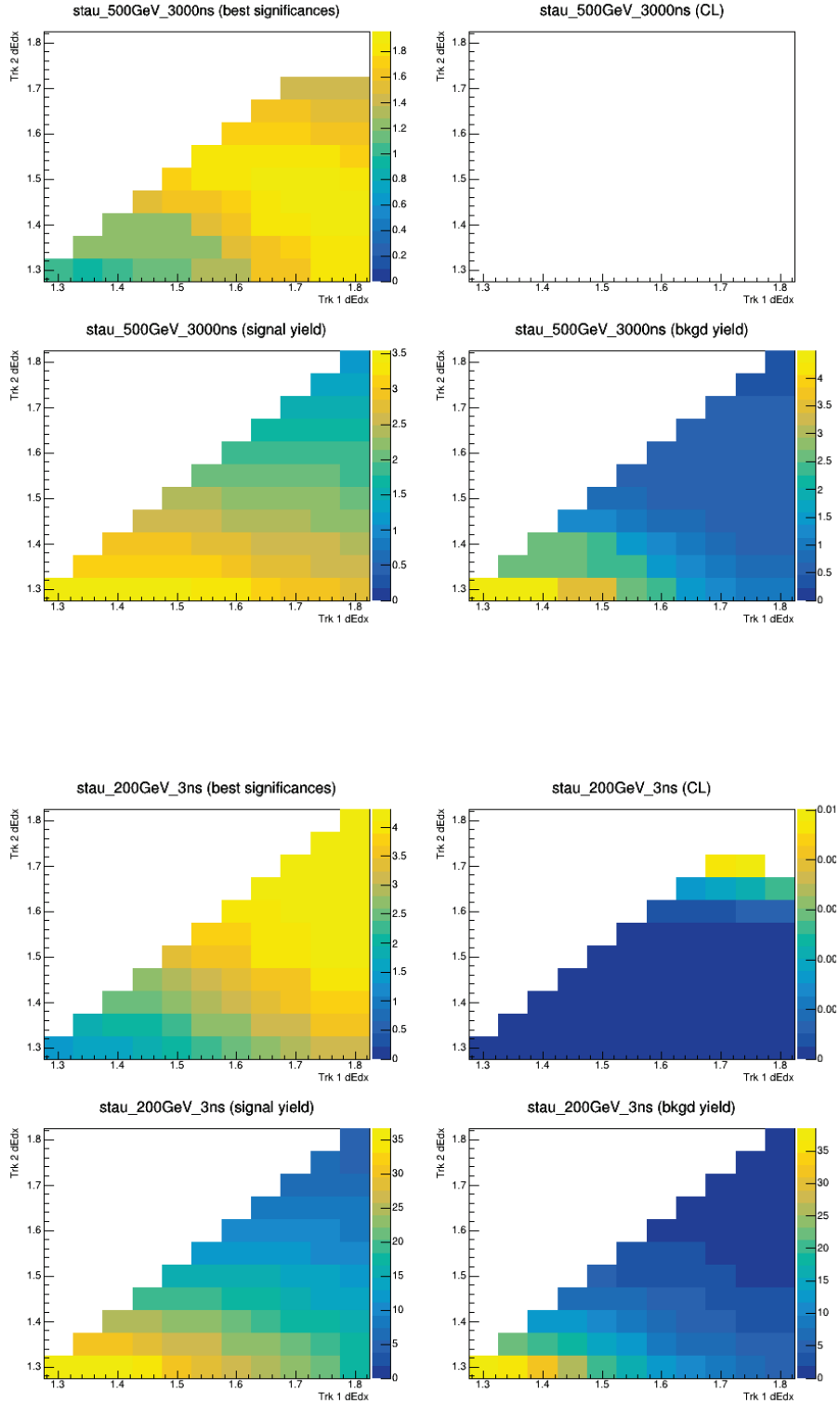


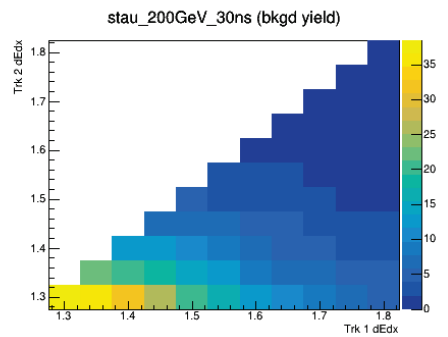
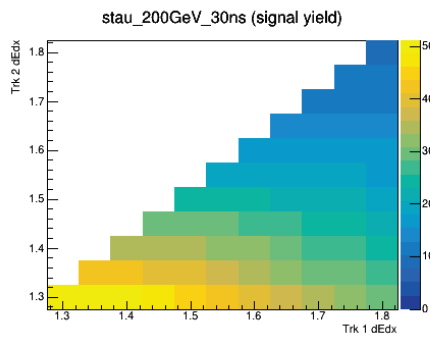
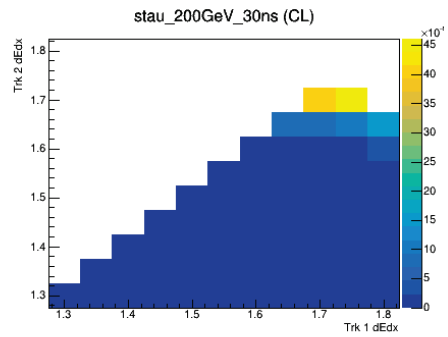
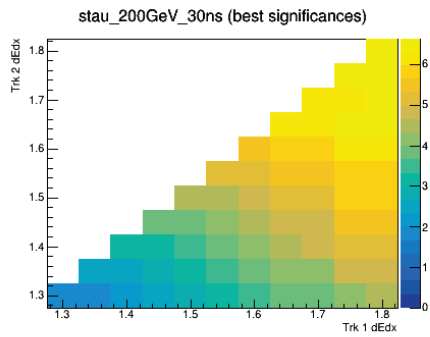
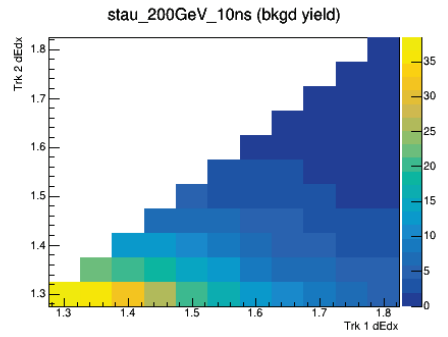
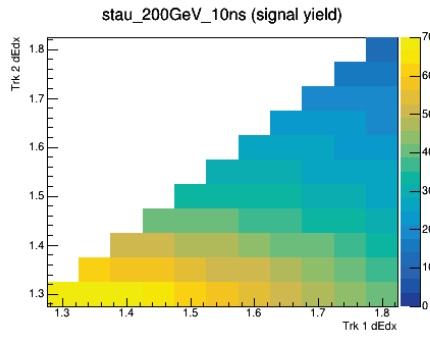
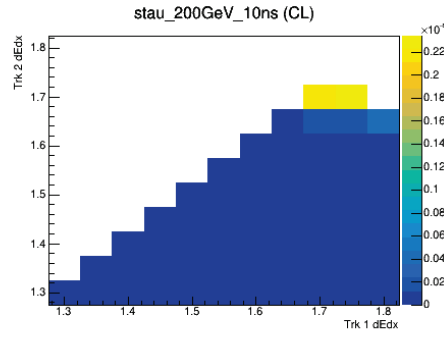
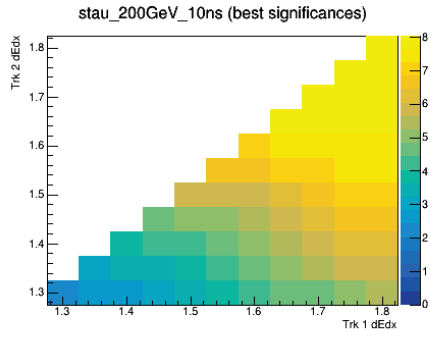


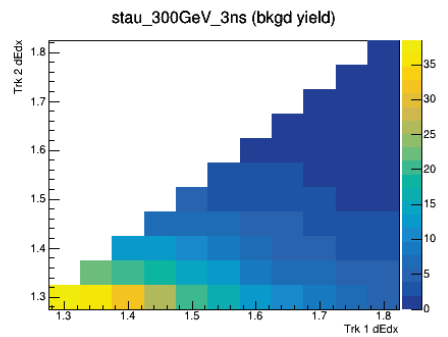
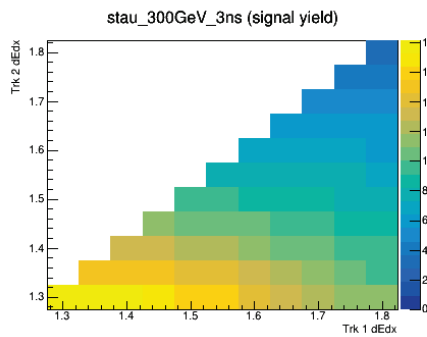
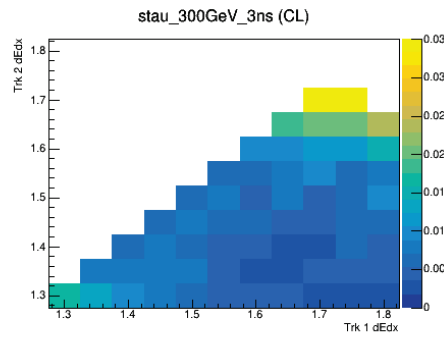
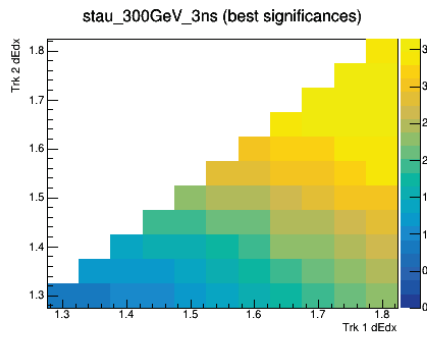
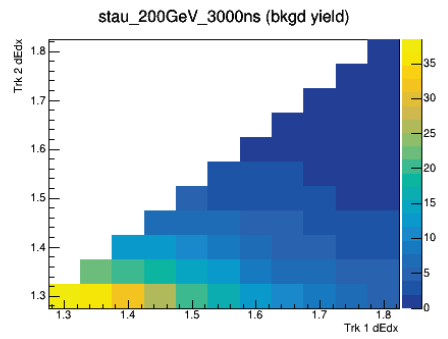
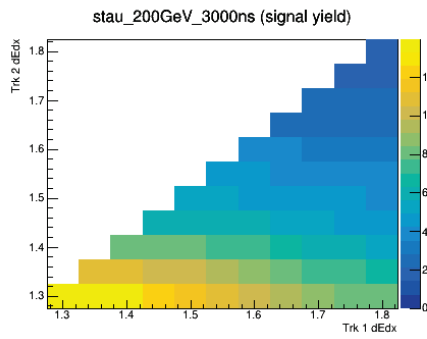
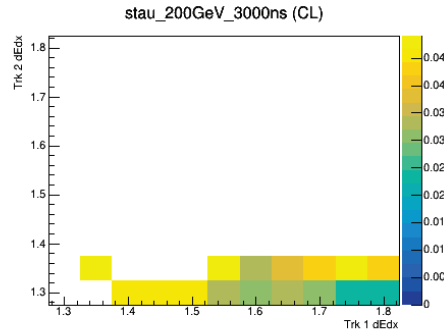
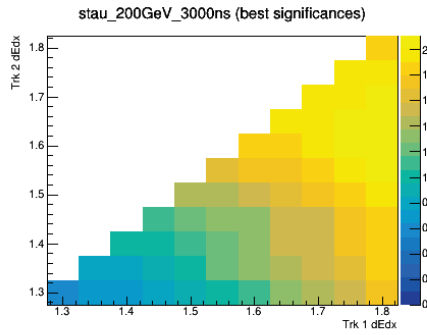


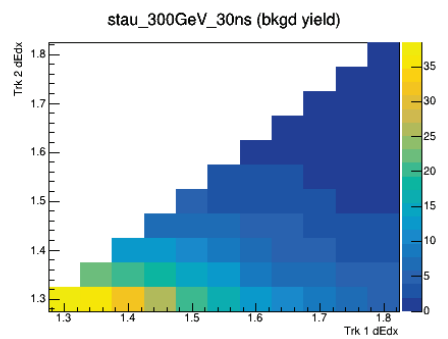
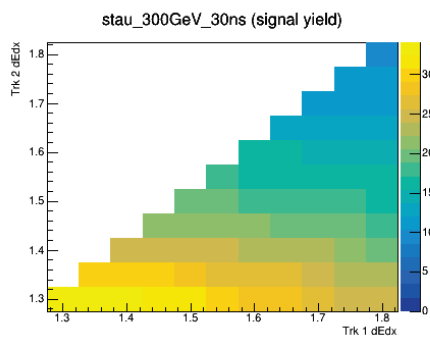
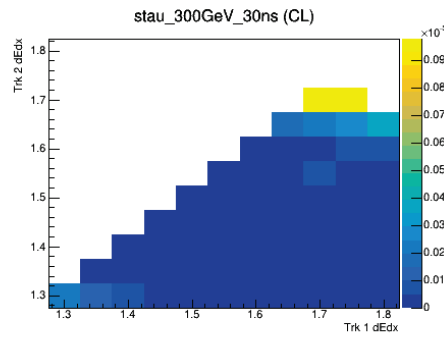
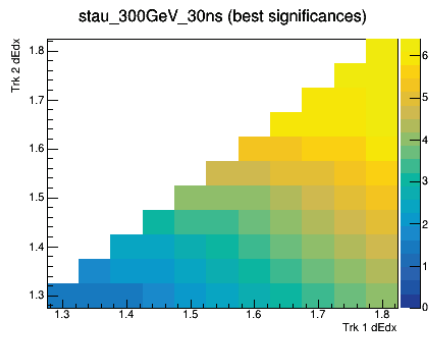
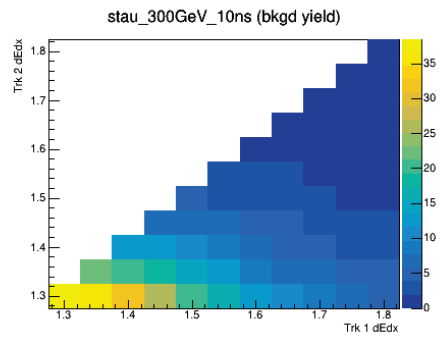
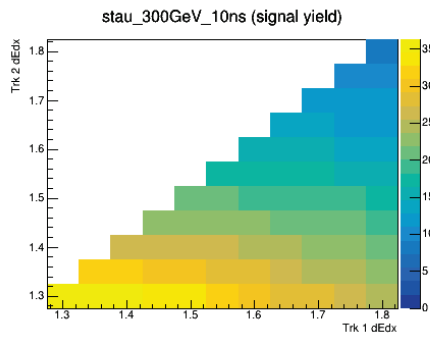
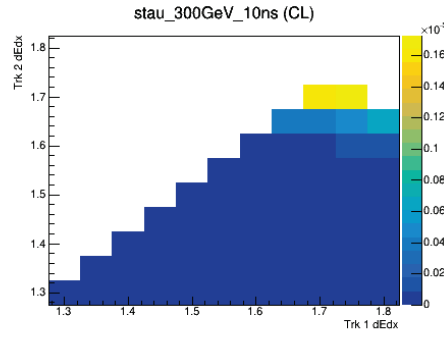
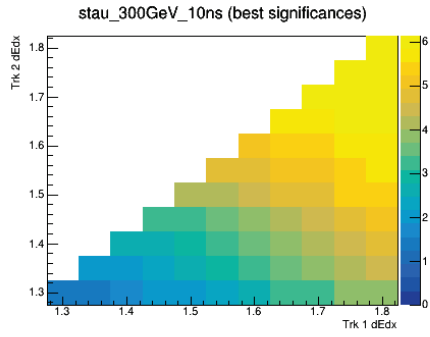


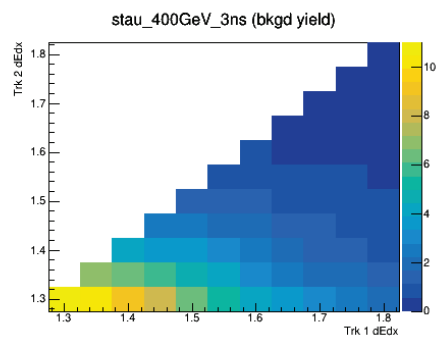
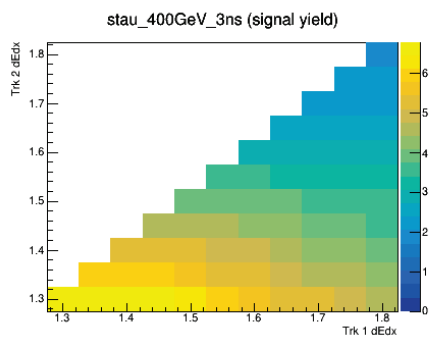
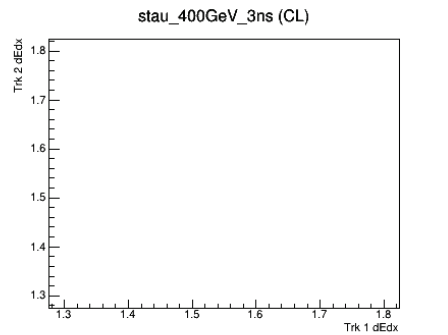
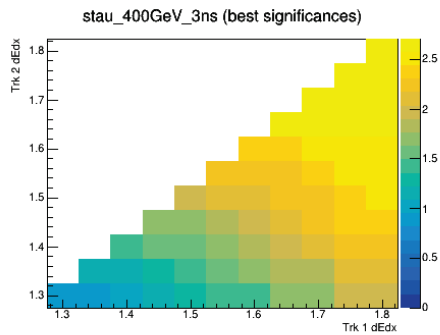
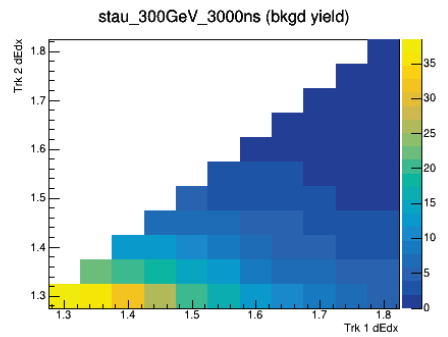
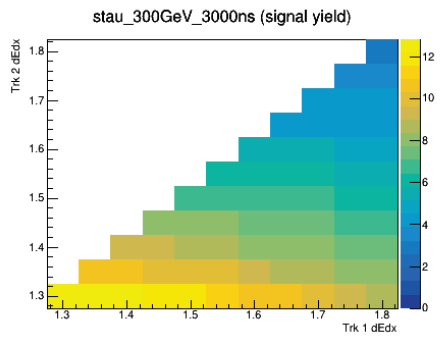
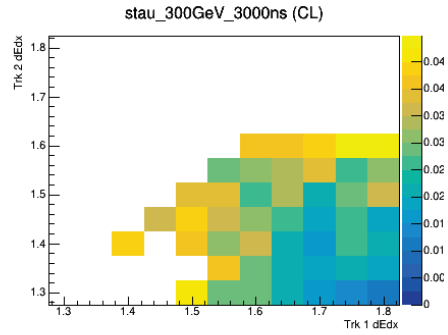
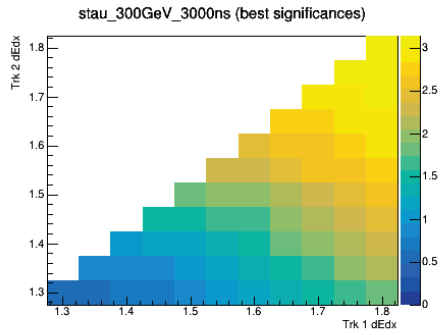




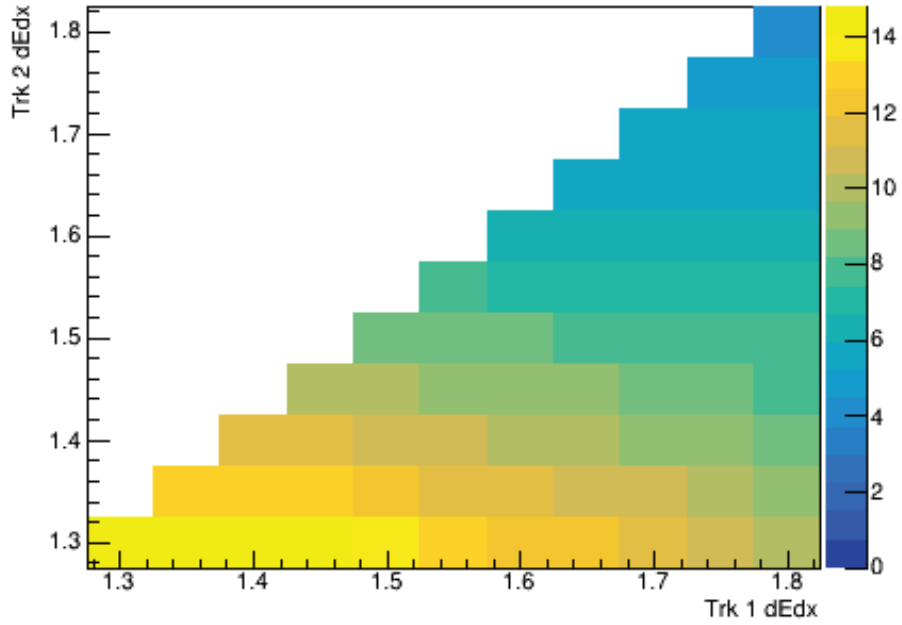




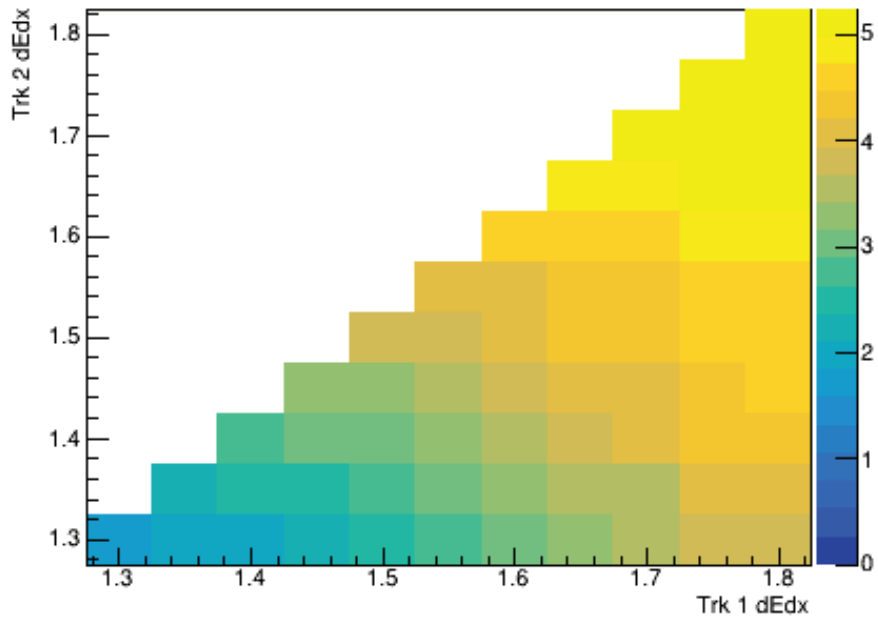


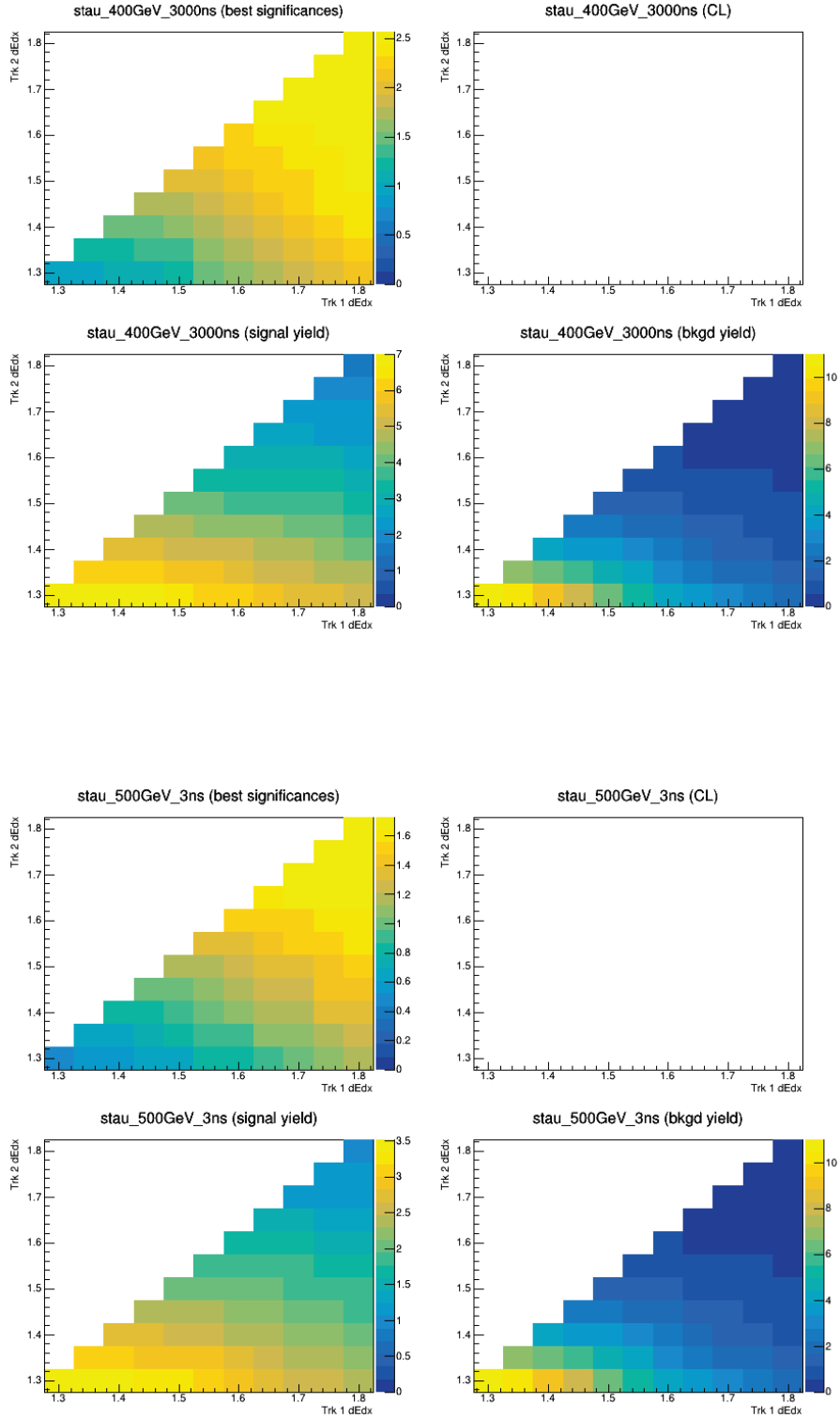


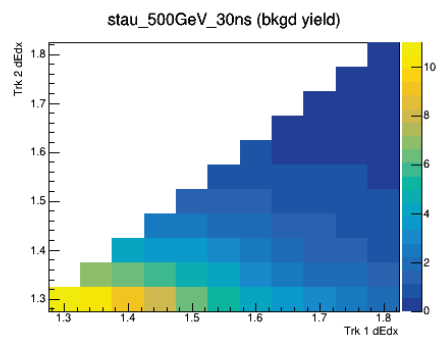
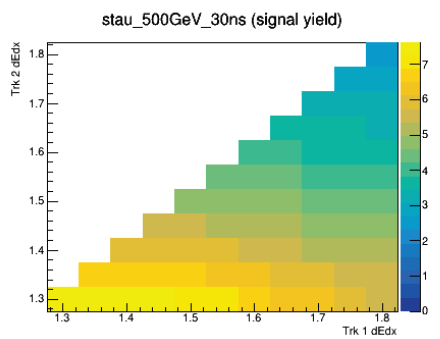
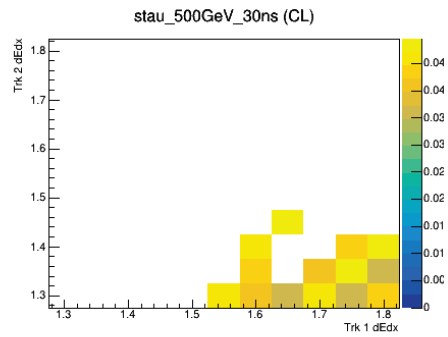
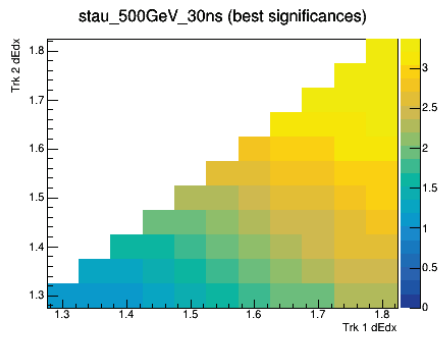
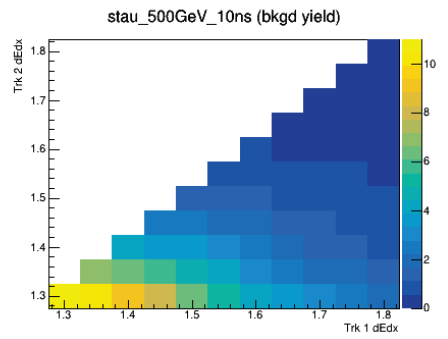
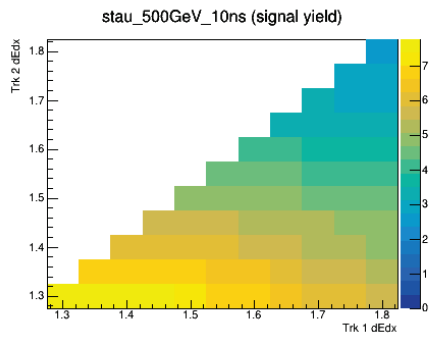
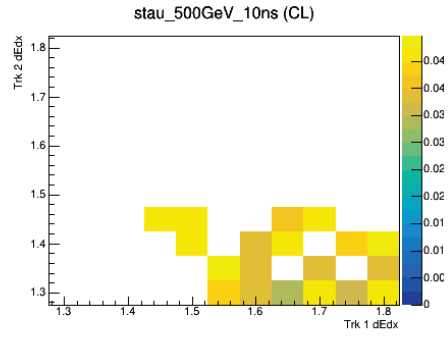
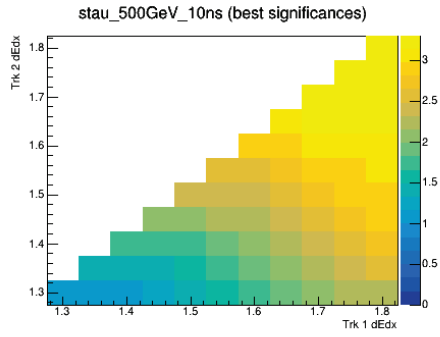
stau\_400GeV\_10ns (signal yield)



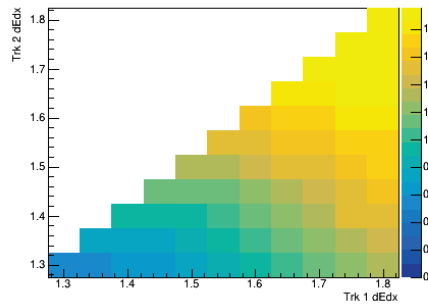
stau\_400GeV\_30ns (best significances)



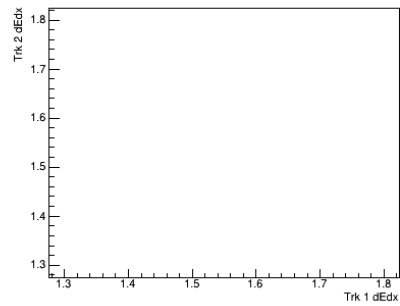




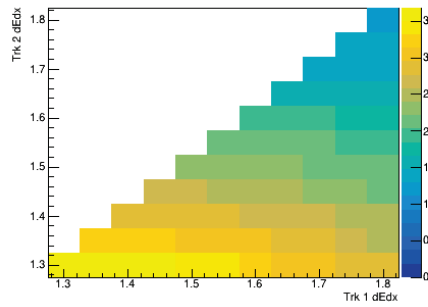
stau\_500GeV\_3000ns (best significances)



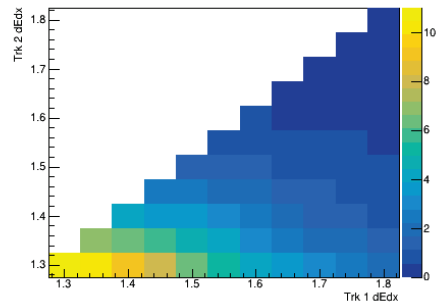
stau\_500GeV\_3000ns (CL)



stau\_500GeV\_3000ns (signal yield)



stau\_500GeV\_3000ns (bkgd yield)



## REFERENCES CITED

- [1] Wikipedia contributors. Standard model of elementary particles — Wikipedia, the free encyclopedia, 2024. URL [https://en.wikipedia.org/wiki/File:Standard\\_Model\\_of\\_Elementary\\_Particles.svg](https://en.wikipedia.org/wiki/File:Standard_Model_of_Elementary_Particles.svg). [Online; accessed 29-August-2024].
- [2] Lawrence Lee, Christian Ohm, Abner Soffer, and Tien-Tien Yu. Collider searches for long-lived particles beyond the standard model. *Progress in Particle and Nuclear Physics*, 106:210–255, May 2019. ISSN 0146-6410. doi: 10.1016/j.pnpnp.2019.02.006. URL <http://dx.doi.org/10.1016/j.pnpnp.2019.02.006>.
- [3] Standard Model Summary Plots June 2024. Technical report, CERN, Geneva, 2024. URL <http://cds.cern.ch/record/2903866>. All figures including auxiliary figures are available at <https://atlas.web.cern.ch/Atlas/GROUPS/PHYSICS/PUBNOTES/ATL-PHYS-PUB-2024-011>.
- [4] ATLAS Collaboration. Observation of a new particle in the search for the Standard Model Higgs boson with the ATLAS detector at the LHC. *Phys. Lett. B*, 716:1, 2012. doi: 10.1016/j.physletb.2012.08.020.
- [5] Yihan Shen. Dark matter: Evidence and candidates. 01 2022. doi: 10.2991/assehr.k.220504.530.
- [6] Vera C. Rubin and Jr. Ford, W. Kent. Rotation of the Andromeda Nebula from a Spectroscopic Survey of Emission Regions. , 159:379, February 1970. doi: 10.1086/150317.
- [7] Douglas Clowe, Maruša Bradač, Anthony H. Gonzalez, Maxim Markevitch, Scott W. Randall, Christine Jones, and Dennis Zaritsky. A Direct Empirical Proof of the Existence of Dark Matter. *The Astrophysical Journal*, 648(2), 08 2006. doi: 10.1086/508162. URL <https://iopscience.iop.org/article/10.1086/508162>.
- [8] Review of Particle Physics. *Progress of Theoretical and Experimental Physics*, 2022(8):083C01, 08 2022. ISSN 2050-3911. doi: 10.1093/ptep/ptac097. URL <https://doi.org/10.1093/ptep/ptac097>.
- [9] S. Navas et al. *Phys. Rev. D*, 110:030001, Aug 2024. doi: 10.1103/PhysRevD.110.030001. URL <https://link.aps.org/doi/10.1103/PhysRevD.110.030001>.

- [10] Stephen P. Martin. A Supersymmetry Primer. *Adv. Ser. Direct. High Energy Phys.*, 18:1, 1998. doi: 10.1142/9789812839657\_0001.
- [11] Dan Green, editor. *At the leading edge: the ATLAS and CMS LHC experiments*. World Scientific, Singapore, 2010. ISBN 978-981-4304-67-2. doi: 10.1142/7349.
- [12] ATLAS Collaboration. ATLAS Insertable B-Layer: Technical Design Report, 2010. URL <https://cds.cern.ch/record/1291633>.
- [13] T. Flick, P. Gerlach, K. Reeves, and P. Maettig. ATLAS pixel detector timing optimisation with the back of crate card of the optical pixel readout system. *JINST*, 2:P04003, 2007. doi: 10.1088/1748-0221/2/04/P04003.
- [14] ATLAS Collaboration. ATLAS Inner Detector: Technical Design Report, Volume 1, 1997. URL <https://cds.cern.ch/record/331063>.
- [15] ATLAS Collaboration. ATLAS Inner Detector: Technical Design Report, Volume 2, 1997. URL <https://cds.cern.ch/record/331064>.
- [16] ATLAS Collaboration. ATLAS Liquid Argon Calorimeter: Technical Design Report, 1996. URL <https://cds.cern.ch/record/331061>.
- [17] ATLAS Collaboration. ATLAS Tile Calorimeter: Technical Design Report, 1996. URL <https://cds.cern.ch/record/331062>.
- [18] ATLAS Collaboration. ATLAS Muon Spectrometer: Technical Design Report, 1997. URL <https://cds.cern.ch/record/331068>.
- [19] ATLAS Collaboration. ATLAS TDAQ System Phase-I Upgrade: Technical Design Report, 2013. URL <https://cds.cern.ch/record/1602235>.
- [20] Joao Pequeno. Event Cross Section in a computer generated image of the ATLAS detector. 2008. URL <https://cds.cern.ch/record/1096081>.
- [21] ATLAS Collaboration. Jet reconstruction and performance using particle flow with the ATLAS Detector. *Eur. Phys. J. C*, 77:466, 2017. doi: 10.1140/epjc/s10052-017-5031-2.
- [22] Matteo Cacciari, Gavin P. Salam, and Gregory Soyez. The anti-kt jet clustering algorithm. *Journal of High Energy Physics*, 2008(04):063, apr 2008. doi: 10.1088/1126-6708/2008/04/063. URL <https://dx.doi.org/10.1088/1126-6708/2008/04/063>.
- [23] ATLAS Collaboration. Performance of missing transverse momentum reconstruction with the ATLAS detector using proton–proton collisions at  $\sqrt{s} = 13$  TeV. *Eur. Phys. J. C*, 78:903, 2018. doi: 10.1140/epjc/s10052-018-6288-9.

- [24] ATLAS Collaboration. Muon reconstruction and identification efficiency in ATLAS using the full Run 2  $pp$  collision data set at  $\sqrt{s} = 13$  TeV. *Eur. Phys. J. C*, 81:578, 2021. doi: 10.1140/epjc/s10052-021-09233-2.
- [25] dE/dx measurement in the ATLAS Pixel Detector and its use for particle identification. Technical report, CERN, Geneva, 2011. URL <https://cds.cern.ch/record/1336519>. All figures including auxiliary figures are available at <https://atlas.web.cern.ch/Atlas/GROUPS/PHYSICS/CONFNOTES/ATLAS-CONF-2011-016>.
- [26] ATLAS Collaboration. Search for heavy, long-lived, charged particles with large ionisation energy loss in  $pp$  collisions at  $\sqrt{s} = 13$  TeV using the atlas experiment and the full run 2 dataset. *Journal of High Energy Physics*, 2023(6), jun 2023. ISSN 1029-8479. doi: 10.1007/jhep06(2023)158. URL [http://dx.doi.org/10.1007/JHEP06\(2023\)158](http://dx.doi.org/10.1007/JHEP06(2023)158).
- [27] ATLAS Collaboration. Search for metastable heavy charged particles with large ionization energy loss in  $pp$  collisions at  $\sqrt{s} = 13$  TeV using the atlas experiment. *Phys. Rev. D*, 93:112015, Jun 2016. doi: 10.1103/PhysRevD.93.112015. URL <https://link.aps.org/doi/10.1103/PhysRevD.93.112015>.